Order Number 9029931

Radial and axial density fluctuations in a high-velocity fluidized bed

Feindt, Hans-Jacob, Ph.D.

City University of New York, 1990

U·M·I
300 N. Zeeb Rd.
Ann Arbor, MI 48106

A

RADIAL AND AXIAL DENSITY FLUCTUATIONS IN A HIGH VELOCITY FLUIDIZED BED

BY

HANS - JACOB FEINDT

A dissertation submitted to the Graduate Faculty in Engineering in partial fulfillment of the requirements for the degree of Doctor of Philosophy, The City University of New York.

1990

This manuscript has been read and accepted for the Graduate Faculty in Engineering in satisfaction of the dissertation requirement for the degree of Doctor of Philosophy.

April 3, 1990 — Chairman of Examining Committee
Date

4/3/90 — Executive Officer
Date

Dr. J.M. Matsen

Prof. R.A. Graff

Prof. G. Tardos

Prof. D. Rumschitzki

Supervisory Committee

The City University of New York

Abstract

RADIAL AND AXIAL DENSITY FLUCTUATIONS

IN A HIGH VELOCITY FLUIDIZED BED

by

Hans - Jacob Feindt

Advisor: Professor H. Weinstein

The use of gas-solid high velocity fluidized beds as catalytic chemical reactors in industrial practice is well known. A typical fast fluidized bed is operated with two distinct flow regions, a dense phase in the bottom and a dilute phase on top giving an s-shaped axial profile of the solid fraction. Recent publications show also the existence of a radial solid distribution profile with a dense wall region and a dilute core in both of the regions. Also, the occurrence of pressure waves in the lower dense region have been reported. These pressure waves, with frequencies of the order of one Hz, were interpreted as resulting from density waves. At this point in time only the first steps in describing the flow pattern for a fluidized bed operating in the high velocity fluidization regimes have been discussed.

In this work a technique is developed to directly measure instantaneous solid fractions and its radial distribution in a riser flow of air and fluid cracking catalyst. The method is based on an x-ray chordal absorptometry technique using phototransistor sensors hardwired to a computerized data acquisition system. Complementary to the x-ray measurements density fluctuations were studied

using instantaneous pressure signals. Measurements were made in a high velocity fluidization unit with an inner diameter of 0.152 m and 8.4 m high. The solid used in this investigation was a Zeolite FCC catalyst, HFZ-33 (dp = 59 μm).

The data confirmed that the pressure readings are dependent on the spacing of the pressure probes. Decreasing the spacing of the probes leads to an increase in fluctuation amplitude and mean time average of the pressure readings, while the power spectrum shows no dependence on the spacing. To obtain reproducible data, a time average of three minutes for the pressure readings and one minute for the x-ray measurements are necessary.

Radial density profiles detected with an x-ray system in the dilute and dense phase show the existence of a core-annulus flow with a dilute core surrounded by a denser wall region. The density profiles indicate clearly that a fully developed flow pattern exists only in the dense phase.

Pressure fluctuation readings converted directly to solid fraction are larger in amplitude than the solid fraction fluctuation detected with the x-ray system. Pressure fluctuation readings are a sum of the pressure drop caused by the solid fraction in a height segment of the riser and acceleration and deceleration of the solid.The power spectra for both the pressure readings and x-ray measurements show a superimposed low frequency.

ACKNOWLEDGMENTS

I am grateful to my mentor, Professor Herbert Weinstein, for his support, encouragement and guidance throughout the research project and also for his personal interest in me.

I wish to acknowledge the members of my thesis committee, Professor R.A. Graff, Professor G. Tardos, Professor D. Rumschitzki and Dr. J.M. Matsen for their interest in this work and helpful suggestions.

Valuable contributions to this work were made by E. Bandlamudi who carried out the calibration of the measurement systems, Lily Li who modified and developed software for this project and Libin Chen who helped perform the experiments.

I like to thank my colleagues and the technical and administrative staff of the Chemical Engineering Department of the City College for their support and assistance, especially Ivan Ortiz who actually designed and build the optical part of the x-ray data acquisition system.

Financial support for this project was given by the National Science Foundation under Grants # CTS-8508336 and INT-8310079. Exxon Research and Engineering Company was the collaborating Industrial organization for the first grant.

Für meine Eltern

Contents

List of Tables

List of Figures

Nomenclature

a_0, a_1,..	constants of polynomial
D	distance centerline bed to x-ray source
d_p	solid particle diameter, μm
f	frequency, Hz
G_s	solid flow rate, kg/m^{2}s
g	gravitational acceleration, m/s^2
H	bed height
r	radial coordinate of the bed, cm
R	radius of bed, cm
r/R	dimensionless radial distance
s	chord length, cm
I	detected intensity of x-ray beam
I_0	detected intensity of the reference x-ray beam
I_s	solid inventory, m
k	x-ray absorption coefficient of absorbing medium
U_g	superficial gas velocity, m/s
U_w	wave speed, m/s
Z	bed height, m

Greek Symbols

θ	chord angle
ϵ	average void fraction of cross section
ϵ_{app}	void fraction calculated from pressure readings
$\epsilon(r)$	local void fraction in radial direction
λ	wave length, m
ρ_s	density of particles, kg/m^3
$\rho(r)$	local density in radial direction, kg/m^3
μ	x-ray attenuation coefficient of medium
Λ	scattering coefficient
σ	variance of probability distribution
τ	x-ray absorption coefficient, Fig. 3.8

1. Introduction

High velocity (circulating) fluidized beds have become more and more attractive in modern industrial application, due to better design of gas-solid separation systems (i.e. cyclones), solid flow control devices (i.e. facette valves) and catalysts (short residence times). High velocity fluidization units may be used especially for very fast gas-solid reactions, where the following notable advantages occur:

- a close approach to plug-like flow of gas and solids
- high temperature uniformity within the bed
- small particle size, intimitate gas-solid contact
- ability to use cohesive particles.

Although the phenomenon of high velocity fluidization has been known for almost half a century, rigorous research work on high velocity and circulating fluidized systems has been published only in the last decade or so. Compared with the low velocity bubbling and slugging fluidization regimes for which there are several models which describe the two phase flow well, only the first steps in describing the flow patterns for the high velocity fluidization regimes have been reported. Major points of discussion still include the definition of the high velocity fluidization regimes and their corresponding significant characteristics. Over the last few years

it has been shown (Li and Kwauk, 1980) that the cross-sectional mean void fraction in the high velocity fluidization regime usually exhibits a strong dependence on its height in the column. A typical fast fluidized bed is operated with two distinct flow regions, a dense phase in the bottom and a dilute phase on top which gives an axial s-shaped profile of the solid fraction. The existence of not only an axial solid distribution profile but also a radial solid distribution profile was shown in recent publications (Weinstein et al, 1986; Werther, 1986). The radial solid distribution profiles show the existence of a dilute core surrounded by a denser wall region.

By analyzing the instantaneous differential pressure readings, Schnitzlein (1987) found a coherent low speed density wave travelling upward only in the dense phase of the riser. Gas tracer experiments by Weinstein et al (1989) at different superficial gas velocities and solid flow rates show for the dilute and dense phase very different characteristics in terms of gas-solid contact and backmixing. Even though the two distinct flow regions, a dilute phase on top of a dense phase, coexist in the riser the two phases exhibit very different physical flow characteristics.

A method to describe the two-dimensional two-phase flow of a high velocity fluidized flow for design purposes is still lacking. In fact, the nature and number of parameters needed to design and operate a circulating fluidized system has yet

to be determined. At this point in time a clear understanding of the physical characteristics of the flow has not been presented. The aim of this experimental program is to provide more basic information to help understanding the nature of the high velocity two phase-flow. For this purpose a new measurement system was developed. The method is based on an x-ray chordal absorptometry technique using phototransistor sensors hardwired to a computerized data acquisition system. With this system instantaneous radial and axial solid fraction profiles are detected and compared with instantaneous axial solid fraction profiles derived from pressure gradient measurements. Fluctuations in pressure gradient and x-ray absorption are collected simultaneously and analyzed in order to draw some conclusions about the structure of the two phase flow. Typical flow structures in both the dense phase and dilute phase are studied and discussed. Implications as to the nature of the stochastic (turbulent) and the quasi periodic structures can be made.

2. Literature Review

2.1 History

The phenomenon of fluidization was first introduced by Fritz Winkler in December 1921. In 1926 I.G. Farben Leunawerke, near Leipzig, Germany, built a large scale fluidized bed using coarse solid particles. The so-called "Winkler Generator" was used for gasifying lignite to produce fuel gas for Otto gas engines that compressed ammonia synthesis gas. In the early 1940s the first commercial fluidized bed catalytic cracker was under construction. On May 25,1942 this unit began to produce components for 100 octane aviation gasoline at Standard Oil of New Jersey's Baton Rouge refinery (now Exxon). A brief history of the application of heterogeneous catalysis in fluidized beds is shown in Table 2.1.

Today the use of fluidization is wide spread in industrial application. The Lurgi Company, West Germany designed the first circulating fluidized bed for the calcination of aluminum hydroxide to alumina (Figure 2.1). Newer applications are Fischer-Tropsch Synthesis to gasoline and dry gas cleaning units for absorption of HF and HCl with aluminum hydroxide in the production of aluminum fluoride (Reh, 1971).

Table 2.1 Major Application of Heterogeneous Catalysis in Fluid Beds (Squires et al.,1985).

Process	Licensor	Status
Fluid catalytic cracking (1942)	Exxon, UOP, Kellogg, Shell, Texaco, others	10×10^6 barrels per day, >350 units
Phthalic anhydride (1945)	Sherwin-Williams, Badger, others	0.3×10^9 pounds per year (United States)
Fischer-Tropsch synthesis (1955)	Kellogg, Badger	3 units (Sasol I), 16 units (Sasol II and III)
Chlorinated hydrocarbons and chlorine (early 1950's)	Badger, Shell, Uhde, PPG, others	Large number of units
Acrylonitrile (1960)	Sohio-Badger	$>6 \times 10^9$ pounds per year, >50 units
Polyethylene (high density, 1968) (low density, 1977)	Union Carbide	>15 units

One of the major applications using Geldart (1973) class B powders is in the generation of steam in atmospheric pressure fluid bed combustion (AFBC) of coal, operating in the low velocity regime only or in the high velocity regime only or as a combination of both (Furusawa and Shimizu, 1988). Compared with a conventional boiler, AFBC-boilers may be used for combustion of low-grade brown coal, coal with high sulfur content, wood, waste and even sewage sludge (Beisswanger, 1980). To reduce sulfur in the waste gas limestone may be added to the bed material, consisting mainly of ash and plain sand, which reacts during the combustion with the sulfur to make gypsum. This advantage makes AFBC-boilers very attractive due to tight exhaust regulations in several European countries and Canada. Also the availability of cheap low-grade coal and increasing problems in the disposal of garbage and waste are making the use of AFBC even more attractive. Large AFBC units (Heyde and Klocke, 1979) cost less to build than traditional pulverized coal boilers.

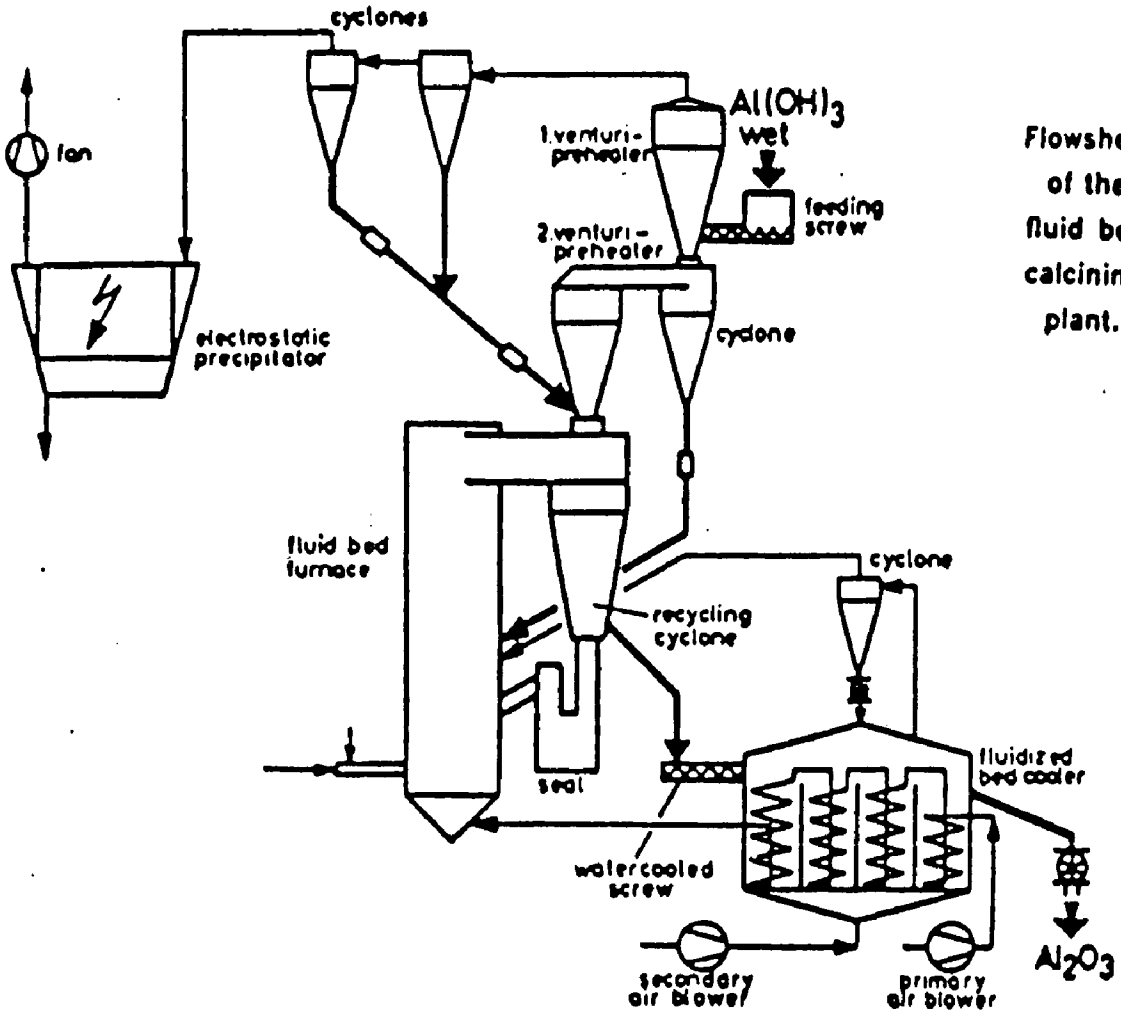

Flowsheet of the fluid bed calcining plant.

Fig. 2.1 Process Schematic for a Circulating Fluidized Bed Calciner.

For combustion in fluidized beds numerous publications and research works are available for calculating heat transfer coefficients in low velocity fluidization regimes (Pope, 1978; Baskakov et al, 1973; Feindt, 1986 etc.), and for high velocity fluidization regimes and for cleanup of waste gases (Basu and Large, 1988; Kaminsky, 1983; Köhling,1978, etc.)

2.2 High Velocity Fluidization Regime

Apparently, the phenomenon of high velocity fluidization was first recognized by Lewis, Gilliland and Bauer (1941) based on observations while fluidizing a pulverized clay catalyst at a gas velocity of 2.4 m/s. This fluidization regime has a significant flow through of solids, which makes a recirculation leg necessary or makes for a limited time of operation starting with a reservoir of stored solid. The first steps in describing the high velocity fluidization regime were taken by Reh, 1971. In his regime diagram the mean void fraction is given as a function of the particle Reynolds number and the Archimedes number. Squires, Yerushalmi and coworkers (1974-1979) used as an additional parameter, the solid flow-rate, to calculate the mean void fraction. Both correlations do not consider a solid profile in the axial direction and it is not clear whether their results apply to the dense region only or a bed average.

Lanneau (1960) presented a measure for transition from low to high velocity fluidization by defining a 'heterogeneity' parameter which is the mean deviation of the instantaneous point density from the time-averaged bed density (Figure 2.2). Yerushalmi et al (1978) also observed at higher gas velocities (using particles with a density of approximately 1000 kg/m^3 and a mean size in the range of 50 to 250 μm) a smoother operation resulting from a decrease in the magnitude of the pressure fluctuations, similar to Lanneau's heterogeneity parameter. This significant reduction in the magnitude of the pressure fluctuation is due to breaking up and disappearance of bubbles.

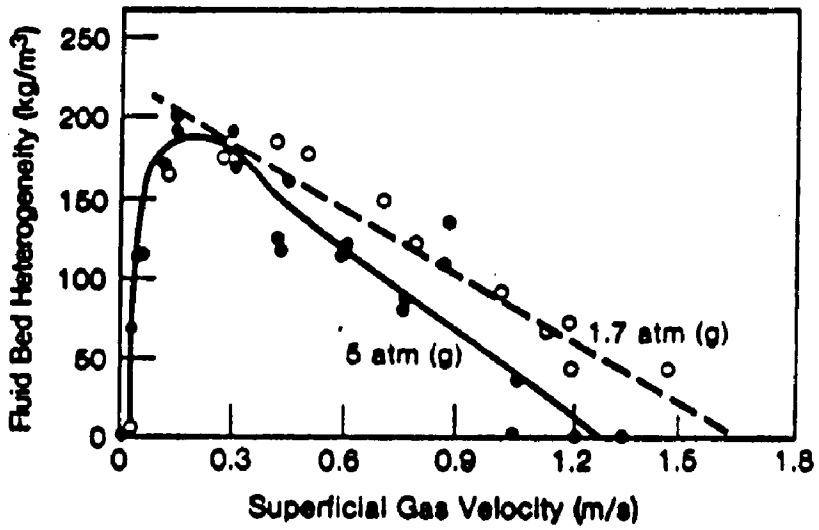

Fig. 2.2 Lanneau's Heterogeneity - the Mean Deviation of the Instantaneous Point Density from the Time Average Bed Density (Lanneau, 1960).

Initially following the decrease, the solid carryover is not great and the bed may be classified in the regime of turbulent fluidization. Schnitzlein (1987) included in his measurements using FCC cracking catalyst the entire regime of high velocity

fluidization (Figure 2.3). The scatter of the data however made it hard to define a transition between turbulent flow and fast fluidization.

Matsen (1988) describes the fast fluidization regime as being when,"at higher voidages and slip velocities the continuous phase of turbulent fluidization disappears and the solids are only present as discrete particles or as ephemeral assemblages or clusters of a statistical-hydrodynamic nature". Dilute phase fluidization is characterized by having a slip velocity which decreases as voidage increases. However the boundary between the turbulent and high velocity fluidized bed is veiled. A more general criterion for fast fluidized beds is that the fast bed contains both a dense phase and a dilute entrained phase above it (Figure 2.4), while a turbulent fluidized bed holds a dense phase only.

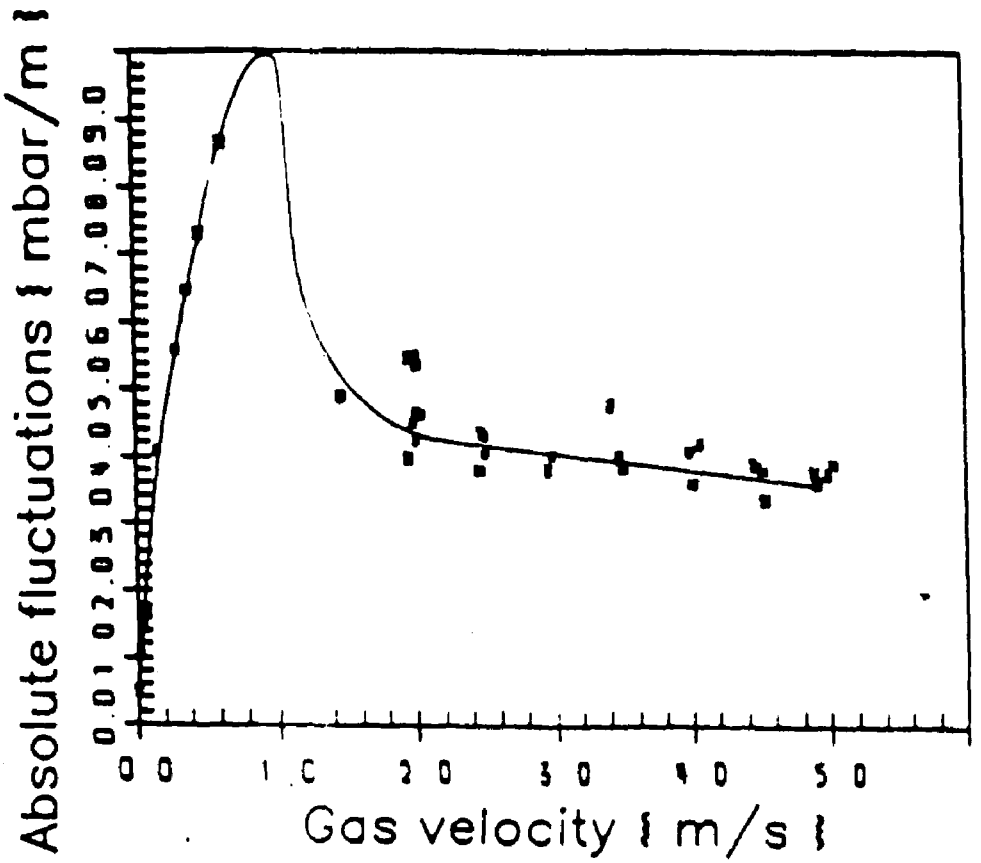

Fig. 2.3 Standard Deviation of Differential Pressure Signals within the Dense Fluidized Region Normalized by the Mean Pressure Difference (Schnitzlein and Weinstein, 1988)

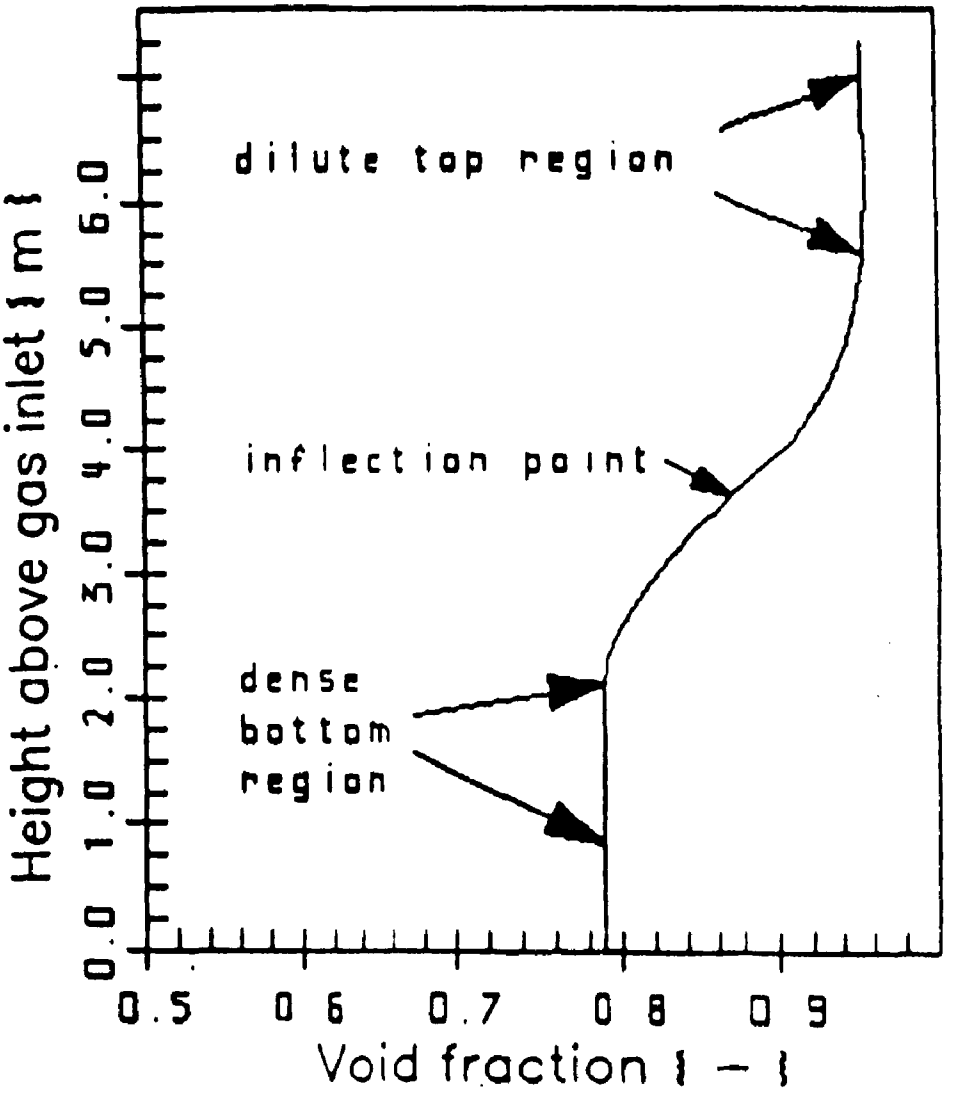

Fig. 2.4 Typical Solid Distribution Profile in Vertical Direction.

2.3 Axial Voidage Profiles

Pressure profiles were reported as early as 1976 by Yerushalmi (1976) using the City College facility. A better description of the high velocity fluidized bed behavior by detailed analysis of the pressure gradients along the bed was done by Li et al in 1981. Pressure profiles with various kind of solids are shown in Figure 2.5.

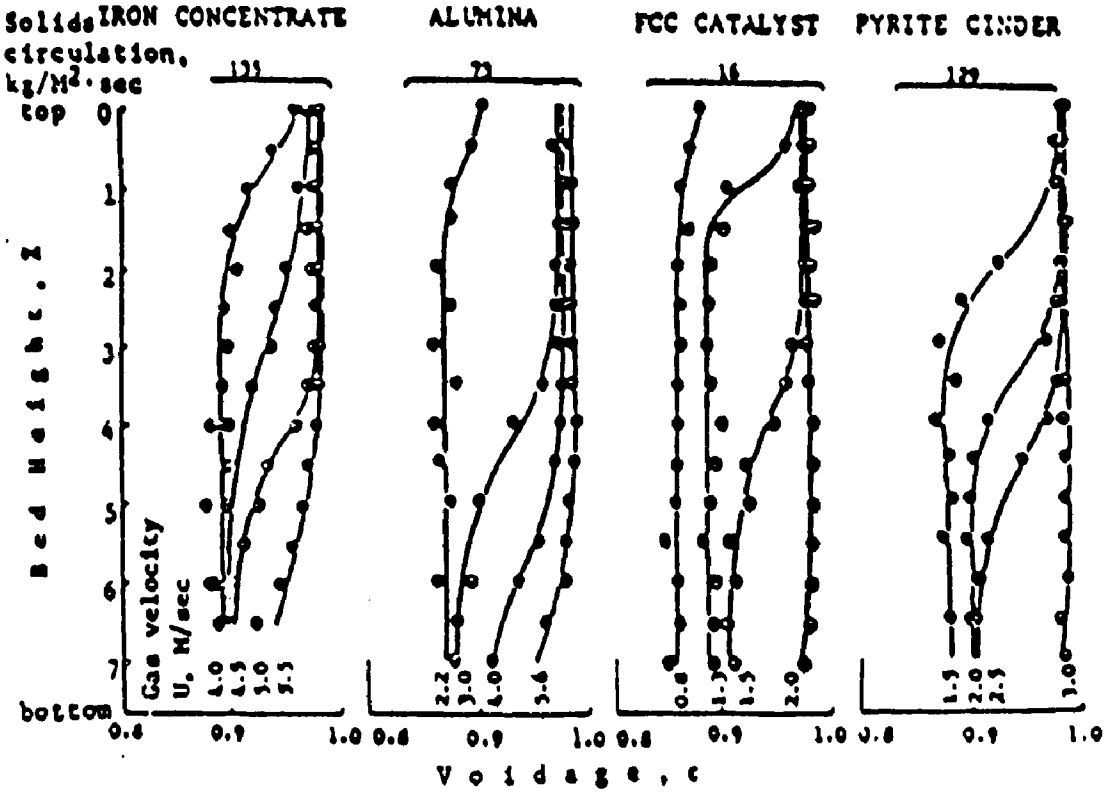

Fig. 2.5 Voidage Distribution Profile Along Bed Height Z (Li, 1980)

A correlation for the vertical solid distribution profile using an equation based on empirically defined parameters was first introduced by Kwauk and coworkers (1980-1981), which describes the s-shape of the density profile well. Similar to bubble correlations in slow velocity fluidized beds a particle cluster concept is used to preserve a one-dimensional picture of the flow (Avidan, 1980, Kwauk and coworkers, 1980-1988). The slip velocity in the dense and dilute phase regions for the two-phase flow of interest is much larger than anticipated in these slip velocity correlations based on the cluster concept. Since the high velocity fluidization regime actually consists of a two-dimensional flow pattern, this one-dimensional cluster picture is thus not one that can result in a consistent analytical relationship of the flow parameters.

With the significant flow through of solids, the high velocity fluidized system must operate with a recirculating leg. Thus the fast bed must be treated as an element of a circulating loop, and the pressure profile in the riser is a function of the gas velocity and also of the operating conditions in the recirculating leg. Figure 2.6 shows a schematic of a typical circulating fluidized bed and a pressure profile. In his paper Matsen (1988) demonstrates the directional changes in various elements of the pressure balance as a result of changes to the independent control

Table 2.2 Response of Dependent Variables to Change in Independent Variables (Matsen, 1988).

	Case	1	2	3	4	5	6
Independent	Gas Velocity	.	0	0	0	.	.
	Valve Opening	0	.	0	.	0	+
	System Inventory	0	0	.	+	+	0
Dependent	Solids Rate	.	.	.	0	0	0
	Cyclone Pressure Drop	.	0	0	0	.	.
	Valve Pressure Drop	.	+	.	+	0	.
	Inflection Point	?	.	.	0	+	+
	Dilute Density	.	.	.	0	+	+
	Dense Density	+	.	.	0	+	+
	Fast Bed Inventory	+	.	.	0	+	+
	Companion Bed Inventory	.	+	.	+	+	.

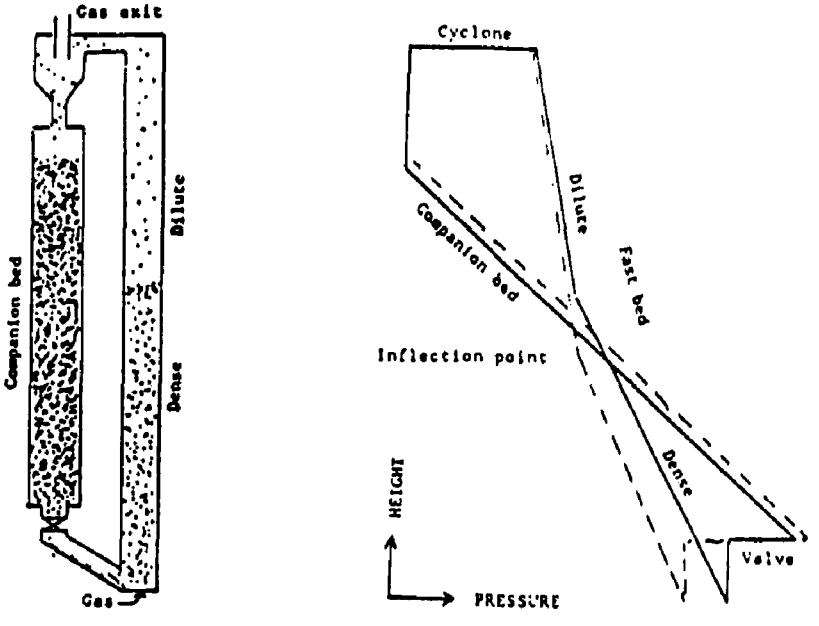

Fig. 2.6 Schematic of Circulation System with Pressure Balance. Dashed Line Shows Effect of Reducing Solid Rate by Decreasing Slide Valve Open Area (Schnitzlein, 1987).

variables of fast bed gas velocity, valve opening, and system inventory (Table 2.2). For case 1, 2, 3 the solid flow rate is reduced by reducing gas velocity, valve opening and inventory (case 2 is shown in Figure 2.6). In cases 4, 5, and 6 one independent variable is held constant, and the two others are manipulated to maintain a constant solid flow rate.

2.4 Pressure Fluctuations

The measurement of pressure fluctuations in a high velocity fluidized bed can give considerable information. Earlier publications in this field like Lanneau (1960, Fig. 2.2) and the City College Investigators (Yerushalmi et al, 1974-1979, Fig. 2.7) used pressure fluctuation relative to the mean pressure drop across a fluid bed to classify the different fluidization regimes. Since then, only a few papers (Fan et al, 1986, three phase flow; Abed, 1984; Schnitzlein and Weinstein, 1988; etc.) can be found analyzing pressure fluctuation in more detail.

Abed (1984) showed in his work that because of low frequency fluctuations Δp readings must be averaged for about 3 min to get a true steady state reading in a turbulent fluid bed. A more detailed study of the pressure fluctuation including Fast Fourier Transform (FFT's) analysis was done by Schnitzlein and Weinstein (1988). They chose the instantaneous differential pressure reading to detect the

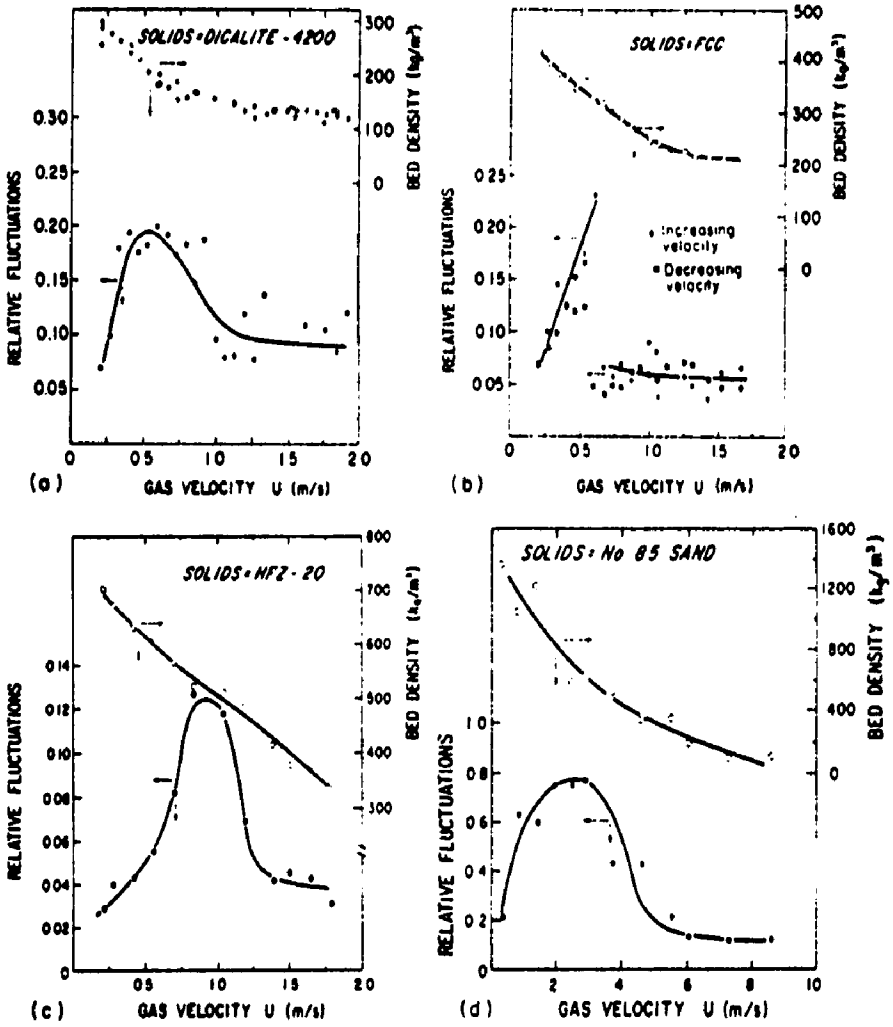

Fig. 2.7 Pressure Fluctuation Relative to the Mean Pressure Drop Across a Fluid Bed of (a) Dicalite, (b) Fluid Cracking Catalyst (FCC), (c) HFZ-20, and (d) Sand. The Upper Curve Gives the Corresponding Mean Pressure Drop Across the Bed.

fluctuations which occur within a differential height, in contrast to those of gauge pressure signals. Probability density functions (PDF's) for the differential pressures in the top and bottom regions of the bed are given in Fig. 2.8 for U_g = 2 m/s and G_s = 88 kg/m^{2}s. It can be seen that the PDF's are asymmetric in the region of high solid fraction at the bottom of the bed and reach a more or less symmetric shape at the top of the column within the dilute region. The fluctuations show a dominant low frequency which is consistent with Abed's data. Upward travelling instabilities within the lower dense region are interpreted as density waves with a wave speed of approximately 1.6 m/s for a wide range of superficial gas velocities (1.5 - 5.0 m/s; Fig. 2.9).

At this point in time there exists no real understanding of the turbulent two phase flow in a high velocity fluidized bed. Thus the two phase flow of interest in these devices are typically complex with a two dimensional field that may exhibit strong stochastic and periodic, or at least quasiperiodic, components. The object of this work is to demonstrate the complexity of these highly turbulent two phase flows. Pressure fluctuation readings are treated statistically and as time averages. An attempt is made to evaluate typical length scales of this two phase turbulent flow similar to the concepts of homogeneous fluid turbulence (Hinze, 1959). The appropriate averaging time to obtain reproducible data is evaluated. An equivalent integral or length scale is derived from pressure fluctuation readings using probes with different tap spacing.

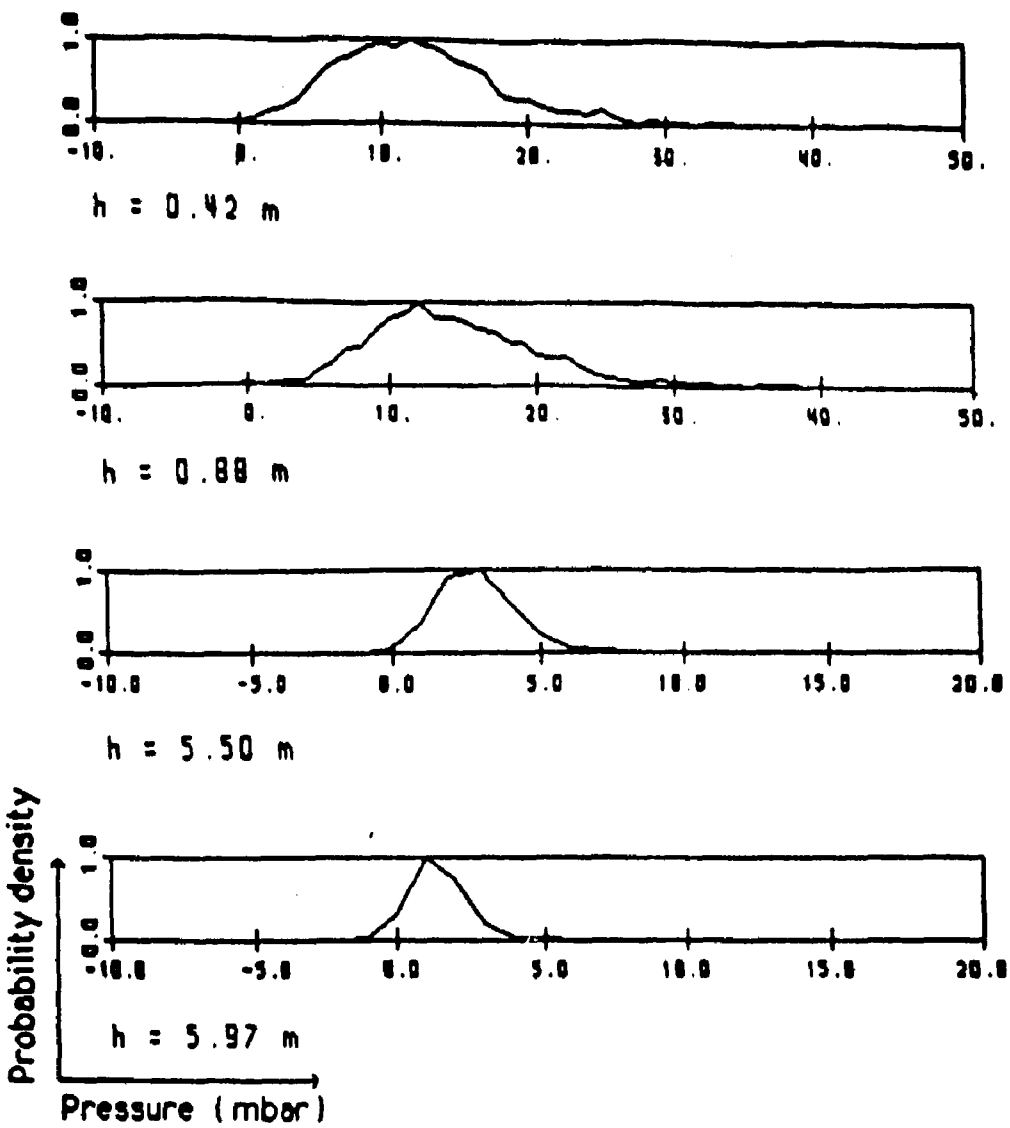

Fig. 2.8 Probability Density Function of Differential Pressures in a Fast Fluidized Bed, U_g = 2 m/s, G_s = 88 kg/m^{2}s (Schnitzlein and Weinstein, 1988).

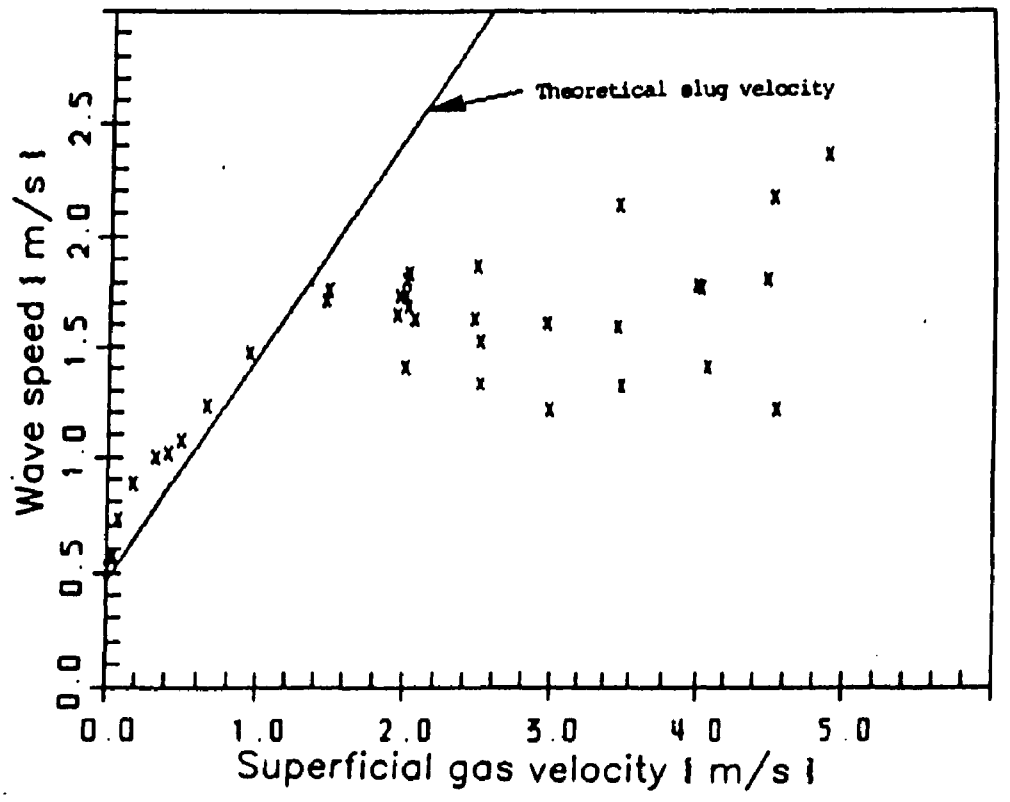

Fig. 2.9 Wave Speed in the Dense Fluidized Region in Various Fluidized Beds as a Function of Gas Velocity (Schnitzlein, 1987).

2.5 Radial Density Profiles

Radial density profiles in a high velocity fluidized bed are discussed only in a few papers. Saxton and Worley (1970) showed that in a large diameter riser cracking unit dense downflow regions can exist in the central core as well as near the wall surrounding less dense high velocity upflow regions. Gajdos and Bierl (1978) used crude x-ray photographs and a suspension sampling technique in a column of 7.5 cm diameter to describe the solid concentration profile. Capacitance probes (Herb et al,1989; Brereton and Grace, 1989) are of limited applicability due to electrostatic charges (Hartge, 1985). More practicable are Fiber optic probes (Quin and Liu, 1982; Werther, 1986) calibrated with an in-situ calibration procedure. Both systems take only readings at one "point" in the bed, the probe has to be moved across the radius to obtain a radial density profile and so do not give instantaneous profiles. Gamma ray scans (Saxton, 1970; Berker and Tulig, 1986) are usually done by rotating a low level source and sensor around the column. Weinstein et al (1985) added an x-ray system to the City College fluidized bed. In contrast to the above described measurement techniques they were able to quantify the radial distribution of solid density over a time period of 5 sec (Shao, 1986). The shortcoming of this work was that due to characteristics of the photographic paper used, only 5 second averages could be obtained.

The radial density profiles obtained with a Laser doppler or Fiber optic system and with the City College x-ray system are presented in Fig. 2.10 and 2.11. The solid distribution profiles are similar in both cases. The dense phase shows a high concentration in the wall region and a dilute region in the middle, like a core-annulus structure. This parabolic solid concentration profile may be interpreted as the result of an internal solid circulation with dense down flow close to the wall. Moving into the dilute region the profile flattens out to a more uniform solid distribution.

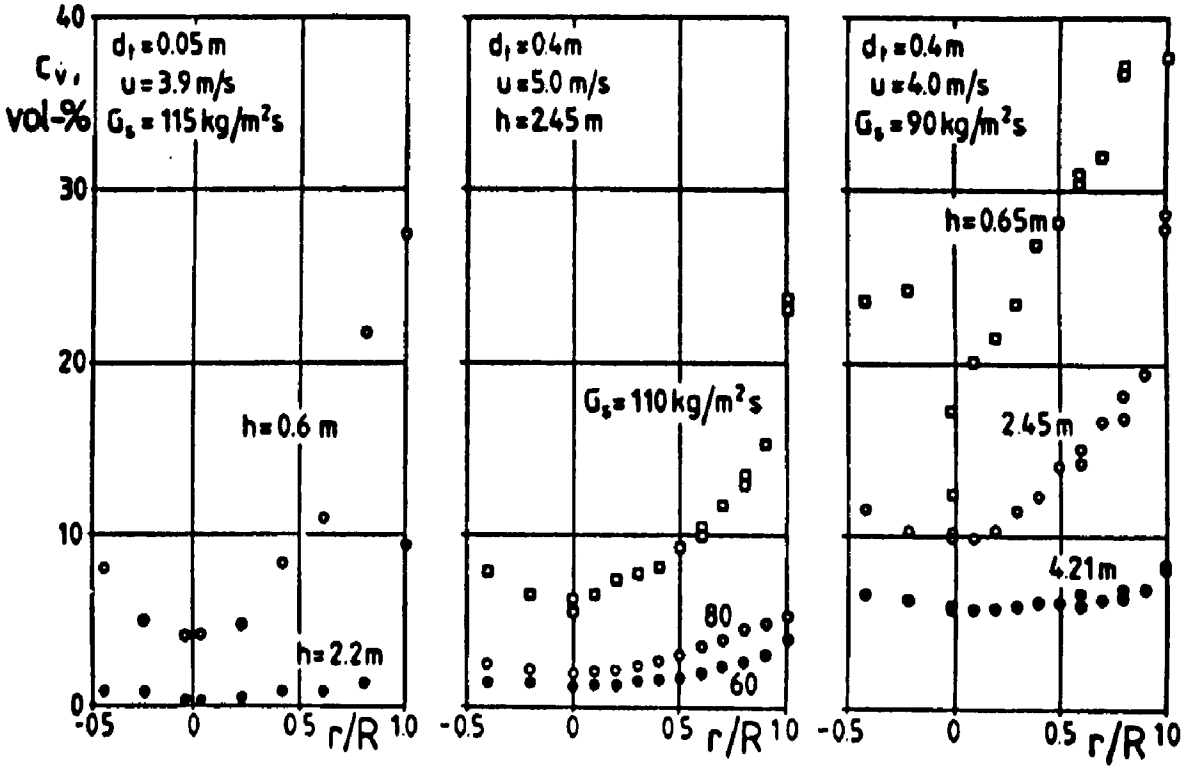

Fig. 2.10 Radial Solid Concentration Profile (Werther, 1986)

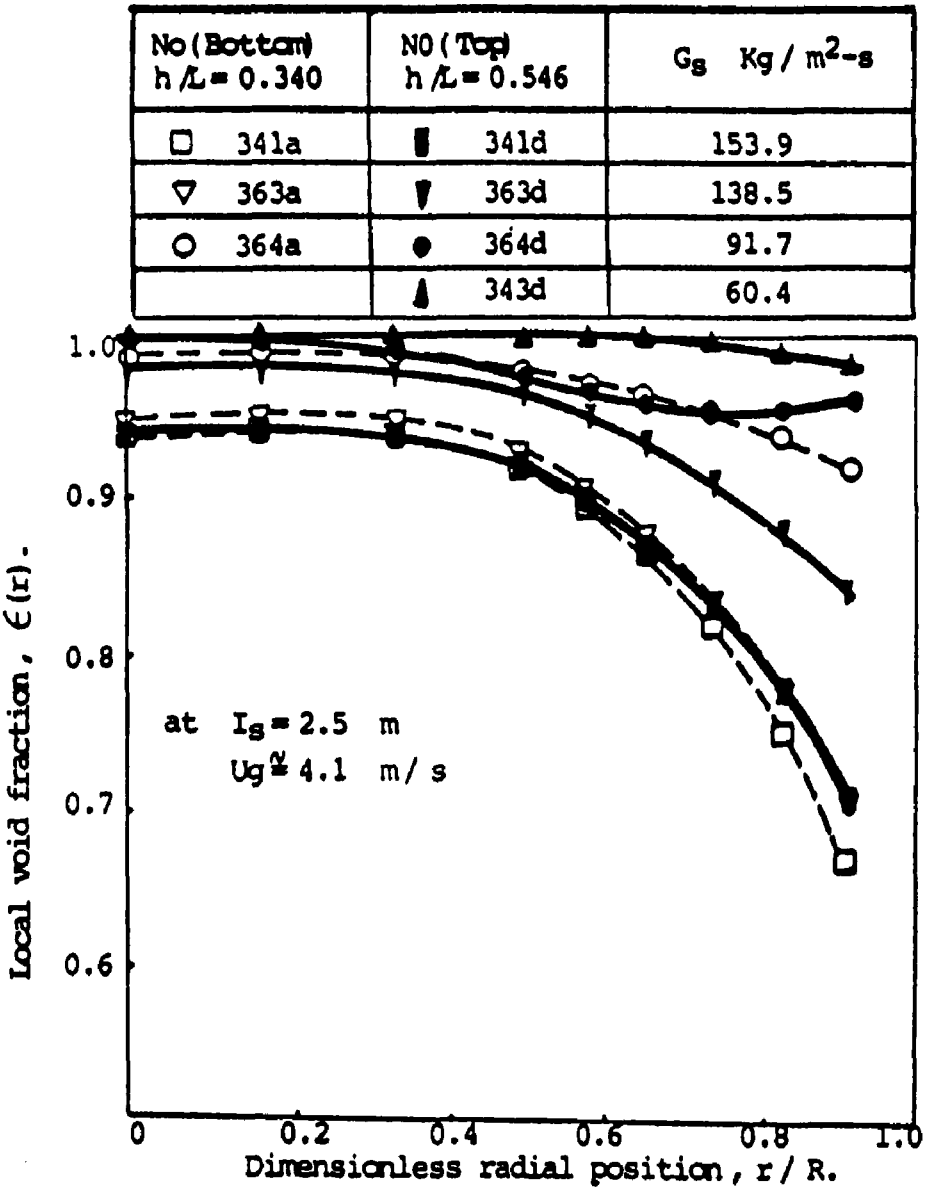

Fig. 2.11 Radial Variation of Void Fraction for Different Solid Rates, I_s = 2.5 m and U_g = 4.1 m/s. Run 364d and 343d in Dilute Phase; Run 341d, 363a and 341a in Dense Phase (Shao, 1986).

Integrating the profile function along the radius results in the cross sectional solid concentration. Measurements of Shao (1986) at the City College facility taken at 5 min time intervals indicate fluctuation in the radial solid profile as well as cross sectional average with time, even though the data are averaged over a time period of 5 sec (Figure 2.12). This indicates that like the pressure readings a minimum data collecting time (Abed (1984) claims 3 minutes) is necessary to get statistical average data.

For the complex flow in the high velocity fluidization regime the question occurs as to whether or not the pressure fluctuations are due primarily to solid fraction fluctuations or to solid fraction fluctuations plus an additional pressure drop resulting from the local accelerations and decelerations of the solid particles in the highly turbulent flow. In the course of this work pressure and density fluctuations, obtained with pressure transducers and the x-ray system, are measured simultaneously and characterized by amplitude and frequency as functions of the flow parameters. Thus, a comparison can be made to determine if terms of correlation of the fluctuating quantities, equivalent to Reynold's stresses, are important in describing the flow.

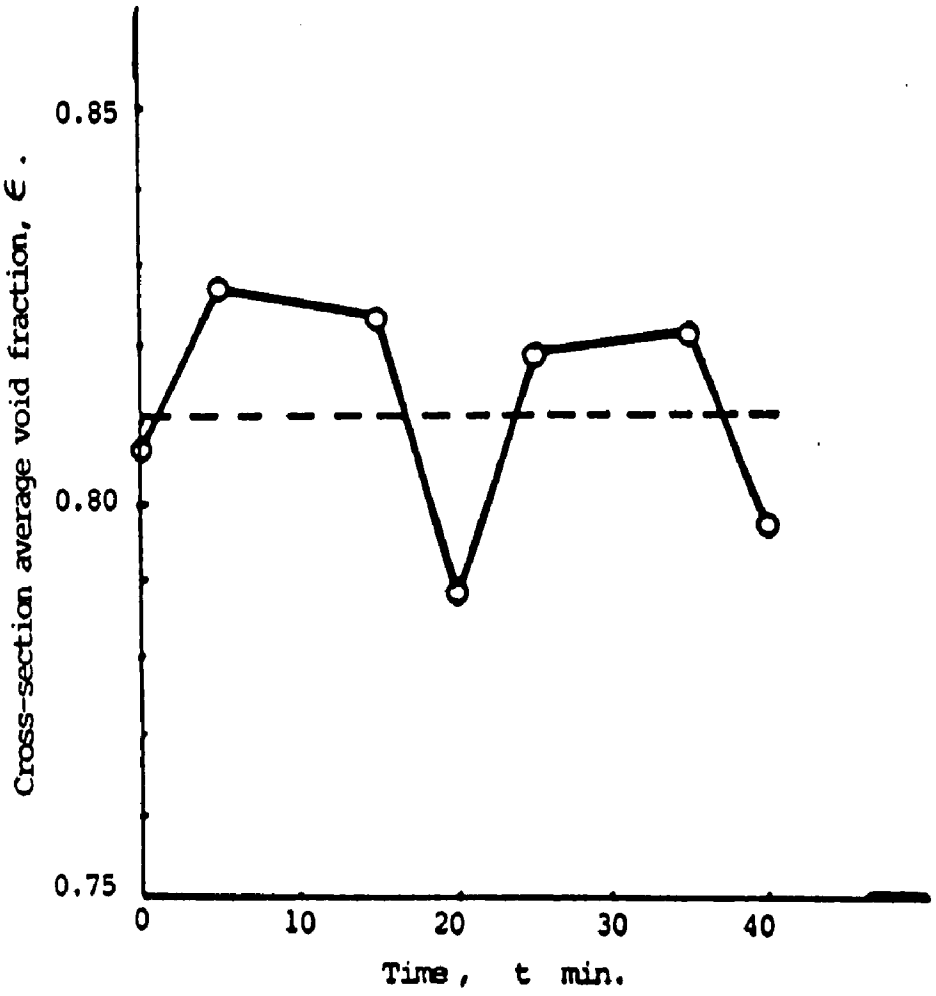

Fig. 2.12 Time Fluctuation of the Cross-Section Average Void Fraction in a Fast Fluid Bed at U_g = 3.0 m/s, G_s = 87 kg/m^{2}s, l_s = 2.5 m and 100 kV, 5 mA at 5 Seconds for HFZ-20.

3. Experimental Procedure

3.1 Fluidized Powder

The solid used in this investigation is Engelhardt HFZ-33 catalyst in unused condition. The catalyst is classified as a Geldart (1984) group A. The properties are shown in Figure 3.1 and Table 3.1.

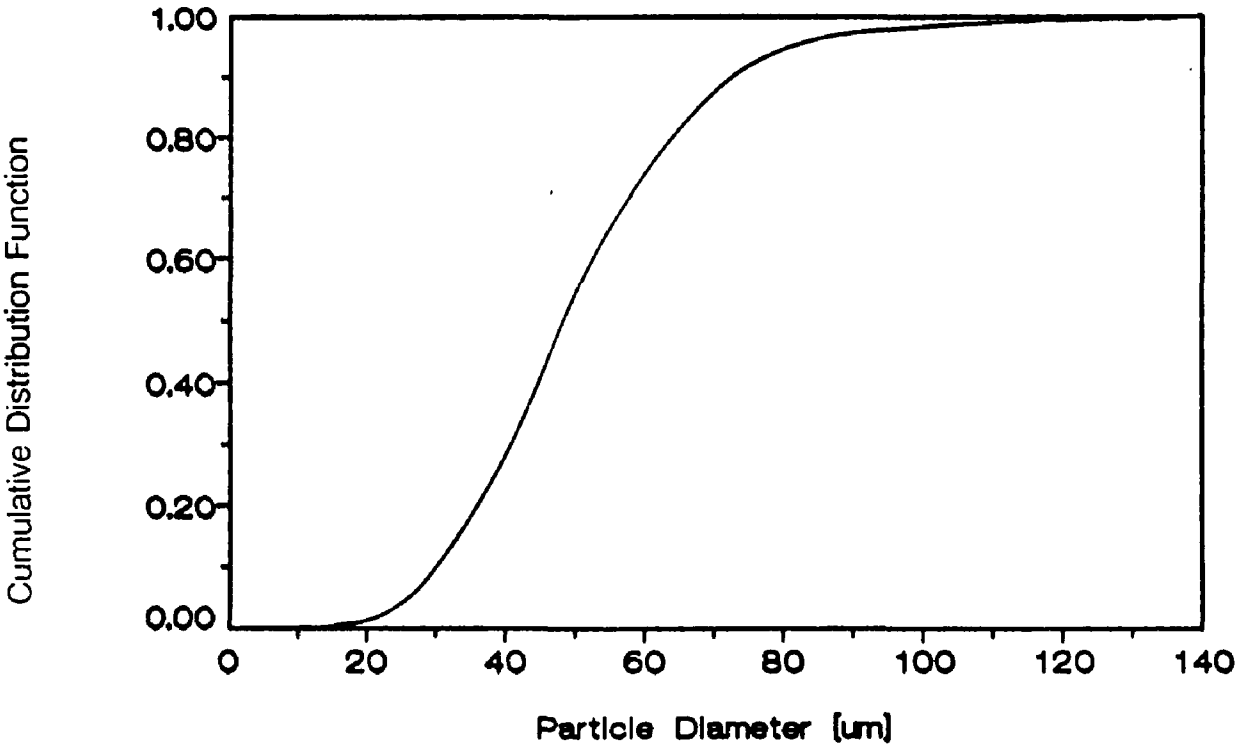

Fig. 3.1 Particle Size Distribution Engelhardt HFZ-33 Catalyst.

Table 3.1 Properties of Engelhardt HFZ-33 Catalyst

Size Range [μm]	d_p [μm]	Density [Kg/m^3]	Sphericity [-]	U_{mf} [cm/s]	ϵ_{mf} [-]
20 - 120	59	1450	1.0	0.09	0.48

3.2 The Circulating System

All of the experiments have been conducted at ambient conditions, i.e. ambient pressure and temperature. The equipment used in this investigation is the City College Fast Fluidized Bed Facility. A schematic of the system is shown in Figure 3.2. On the left side of this figure is the so-called "fast-bed" or riser which consists of a plexiglas tube with an inner diameter of 15.2 cm and a length of 8.5 m. On top of the riser is a 90° glass elbow which directs the upwardly carried solid into a two stage cyclone system. The plexiglas vessel (inner diameter of 0.343 m) on the right side is used as a downcomer and storage bed for the solid. After the secondary cyclone the air is released through a filter bag.

The solid in the storage bed is kept at bubbling "slow bed" conditions. At the bottom air is passed through a conical brass perforated distributor plate to fluidize this bed. It terminates at the bottom into an aerated standpipe of 0.152 m diameter. The standpipe is equipped with a butterfly valve to control the solid rate. The standpipe operates in an unrestrained, fully fluidized mode when the butterfly

valve is fully open. The standpipe operates in a bottom restrained mode when the valve is partially closed to act as an orifice and prevent the continued fluidization of down flowing solids. The height of the solids in the slow bed after slumping them is called the inventory I_s of the system.

Air, the fluidizing medium, is provided by a blower with a flow rate of up to 1400 cfm at 10 psig. The air can be regulated separately over three different air supply lines and enters the system in the U-bend section (N_1, N_2 and N_3, Figure 3.2).

The second butterfly valve in the middle of the slow bed is made out of a sintered plate. It is used to measure the solid flow rate. To determine the solid recirculation rate the change in differential pressure between tap 25 and 23 is recorded with the data acquisition system after closing the top butterfly valve. When this valve is closed, the solids fluidize above the sintered plate and the bed below is carried away. The decay of the pressure drop due to the disappearing lower bed can be determined by applying linear regression (Gaussian least square method). It is assumed that the bed is in a steady fluidized condition. The pressure drop is solely a function of the mass of the fluidized solid in the storage bed. The error range of the detected solid recirculation rate is less than 5% (Schnitzlein and Weinstein (1988)).

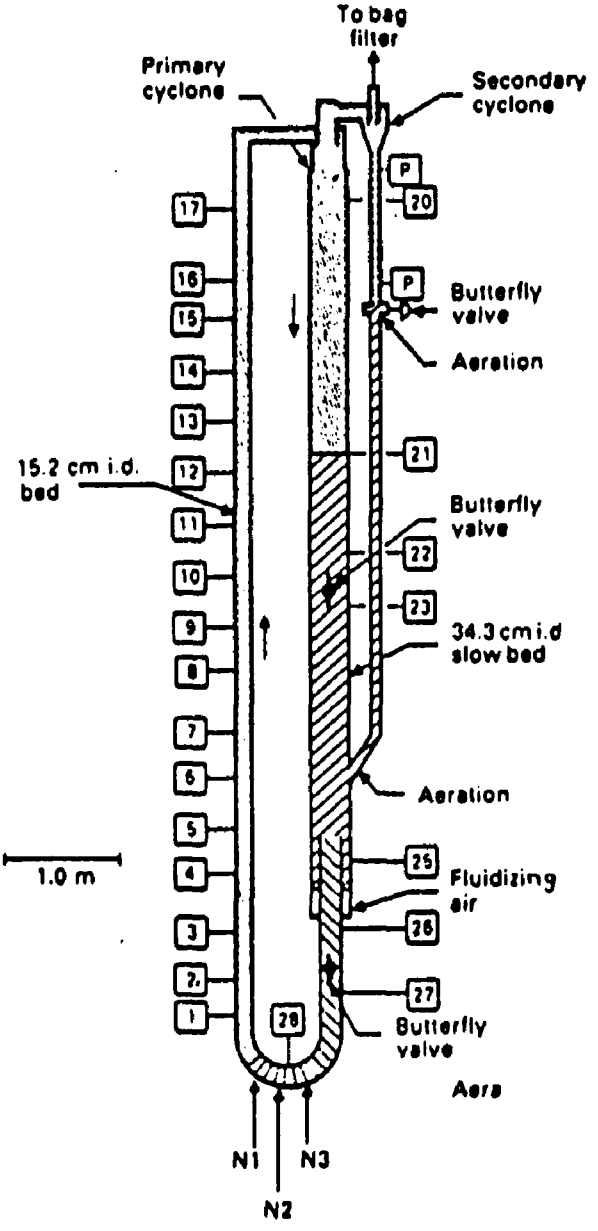

Fig. 3.2 Laboratory System for Fast Fluidization Experiments.

3.3 Pressure Measurements

The circulating system has 27 pressure taps which are flush with the inside column wall (Figure 3.2). The distance between two adjacent pressure taps in the riser averages 0.40 m.Pressure fluctuations are measured by means of piezo-electric pressure transducers (Schnitzlein, 1987). The output signal range of the transducers is 0 - 10 volts. The transducers are hardwired to two real time computer systems (Intel 86/310 with IRMX operating system and Dell System 310 with DOS operating system). It is possible to do online analysis including Fast Fourier Transform (FFT) of the collected data. Examples of probability density functions are shown in Figure 3.3 and 3.4 along with auto- and cross-correlation. Also power-spectra and time-series are presented in graphical form.

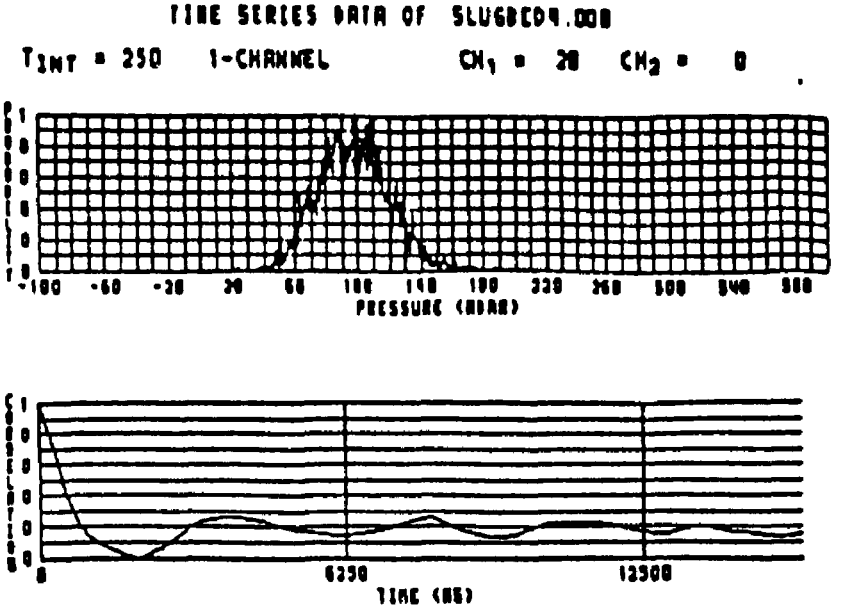

Fig. 3.3 Time Series Analysis of a Slugging Fluidized Bed, One-Channel Analysis.

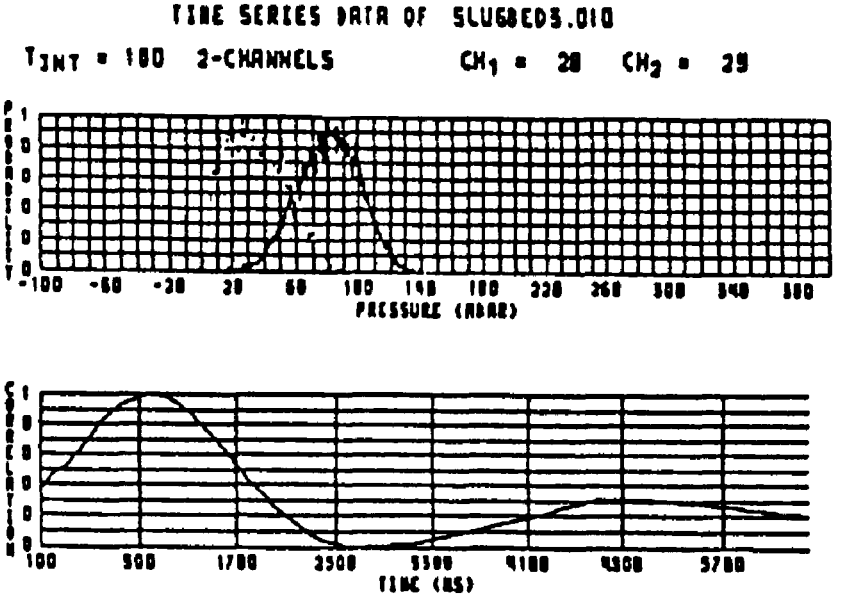

Fig. 3.4 Time Series Analysis of a Slugging Fluidized Bed, Two-Channel Analysis.

3.4 X-Ray System

3.4.1 Hardware

The x-ray source is a Norelco MG 150/300 generator designed for continuous output and high intensity operation. In this investigation a 150 kV x-ray head is used with a maximum level of 30 mA at 100 kV and 20 mA at 150 kV. The x-ray tube is a fixed anode type with two focal points of 15 and 40 mm. The focal spot is chosen to be 40 mm because it provides a wider angle of the x-rays. The operating conditions (voltage and current) can be adjusted at the control console.

The x-ray image of the bed is projected onto a 9" Phillips image intensifier screen. It converts the x-ray into visible light and projects it onto a 3" output screen. Behind the intensifier (Figure 3.5) a mirror box is mounted. The mirror has an angle of 45° to the 3" screen. 10% of the light passes the mirror and is monitored by a closed circuit T.V. camera which is connected to a monitor in the control room. 90% of the light is projected onto a curved 6" plexiglas screen by means of a focal lens. The plexiglas screen is equipped with 48 phototransistors all at equal distance from the image intensifier screen. These are arranged such that 3 rows of 16 transistors can be used to scan the projected image of the bed at 1 cm intervals. The optical setup is shown in Figure 3.6.

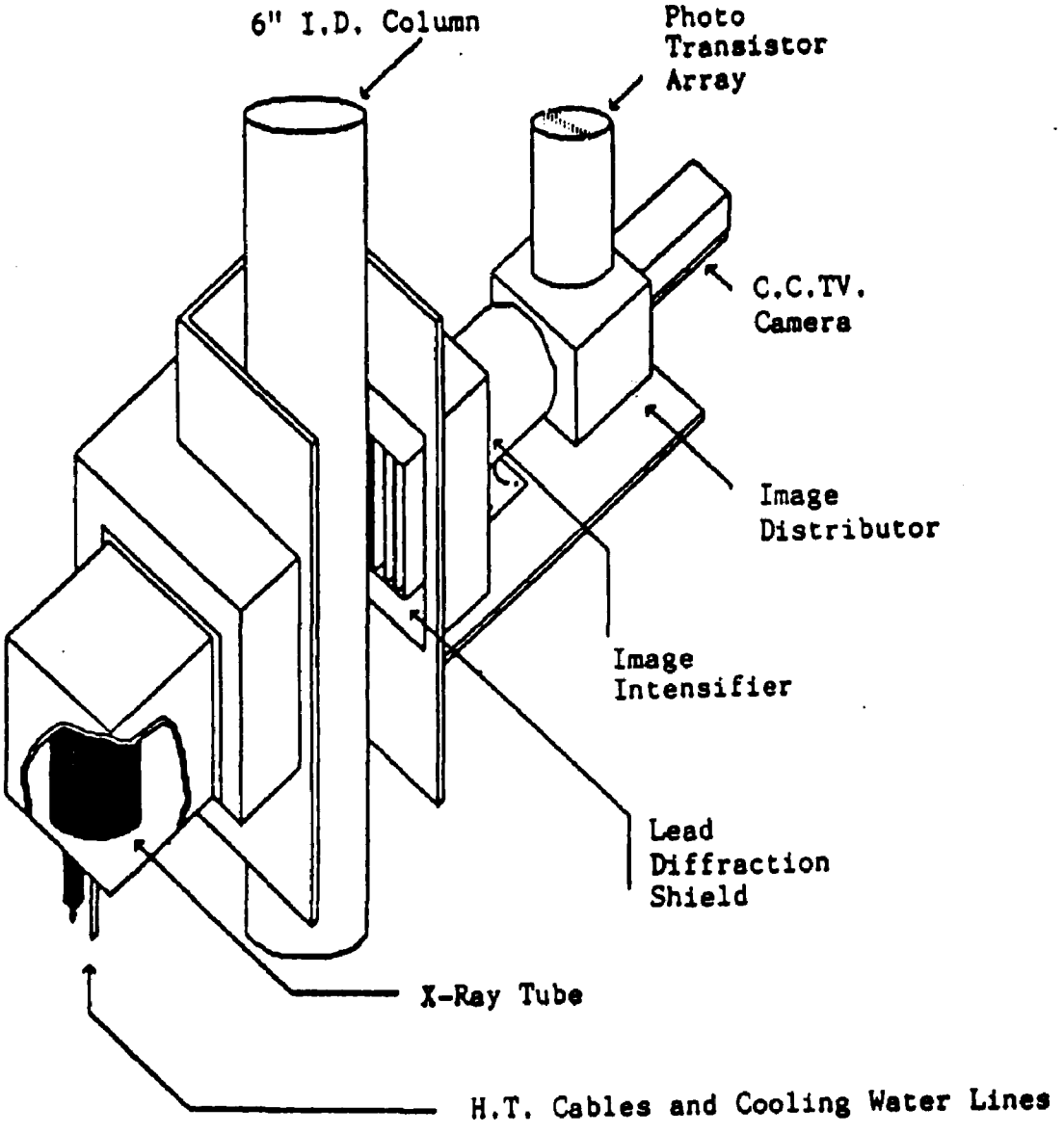

Fig. 3.5 Schematic Representation of the X-Ray Carriage Assembly.

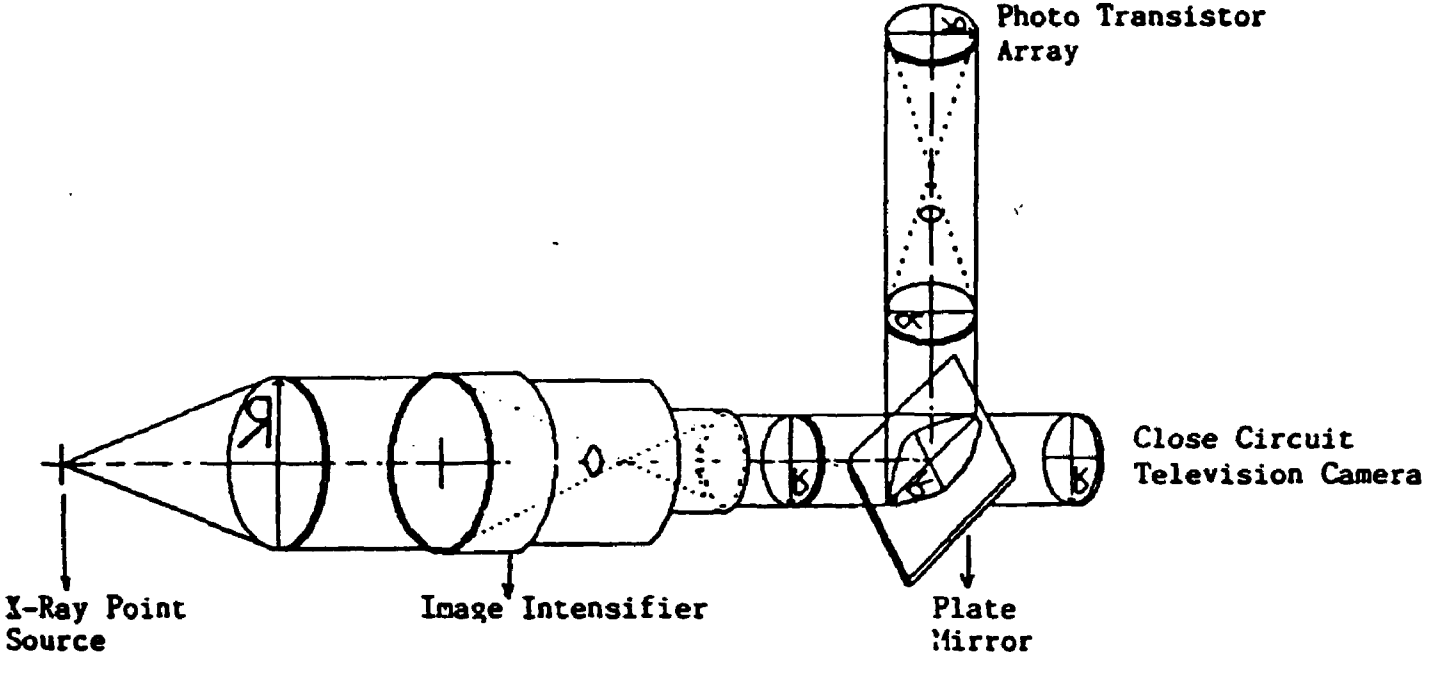

Fig. 3.6 Optical Setup of the X-Ray Imaging System.

The image intensifier with the transistor array and the x-ray head are mounted on a platform. The platform is guided by two vertical supports and can be moved up and down by means of a winch. The winch is controlled from the control room so that every desired height within the working range, beginning at pressure tap 2, can be reached. To minimize radiation leakage, the tray and the x-ray tube box are shielded with lead.

3.4.2 Data Acquisition System

Shao (1986) recorded the x-ray beam intensity with a film plate (Kodak Industrex type M) positioned in front of the intensifier. She only could expose the film over a time period of 5 sec in a discontinuous manner in order to achieve the desired density of the exposed film. Her optimal operating conditions for the x-ray source were 100 kV and 5 mA.

In this work the x-ray image is detected by means of 48 phototransistors (Figure 3.5 and 3.6) arranged in an array of three rows. All parts are made out of black plexiglas and shielded carefully with black cardboard to avoid light leakage. The sensors are SKN 042 NPN silicon photo- transistors. Transistor windows are made out of an optical epoxy lens to increase the sensitivity. The response time is given

as 1 μsec (1 MHz). To get a low noise/signal ratio the output of the transistors is connected to an dual JFET input operational amplifier. This is a low noise device of type TL 082. The circuit diagram is shown in Figure 3.7. It is possible to increase or decrease the amplification by changing the feedback resistor. The output level can be adjusted with the 100 kΩ trimpotentiometer. For this setup the amplification ratio is 1:600. The output range is between 0 - 10 Volts. The circuit in Figure 3.7 is duplicated for each one of the 48 phototransistors. The output of the amplifiers are hardwired to a Dell 386/20 MHz with an Metra-Byte DAS20 analog to digital converter board. This measurement technique allows the collection of short and long term time series depending on available storage capacity of the computer system.

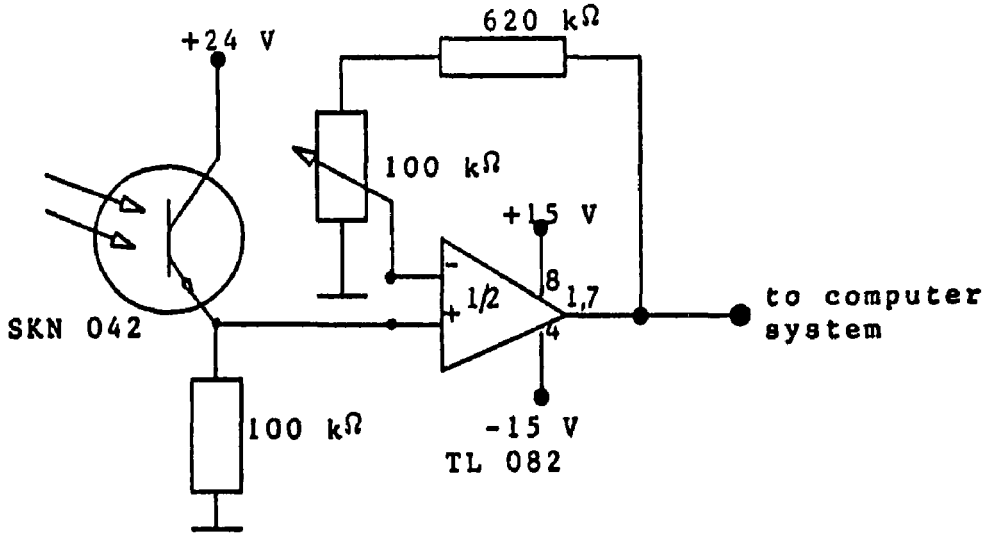

Fig. 3.7 Circuit Diagram of Sensor Elements.

In comparison to the approach taken by Shao (1986) the above mentioned technique does not require optimizing the operating conditions of the x-ray intensity. It is important to maintain a minimum x-ray intensity to insure detection of the beam after it passes through the absorbing medium. If the intensity is to high, low particle concentrations are not detected. This occurs when the intensifier is working in the saturated range. The settings at the control panel may be vary between 80 - 100 kV and 5 - 8 mA.

Tests with an ionization chamber did not give satisfactory results. The decay time after introducing a Dirac-pulse is very large (on the order of seconds). Thus due to the integrating effect of the ionization chamber instantaneous signal fluctuation reading are not possible.

3.4.3 Calibration Procedure

The x-ray system provides a polychromatic photon beam of high energy. Low frequencies are filtered out by means of an aluminum plate in front of the x-ray source. This gives a narrow frequency distribution which behaves similarly to a monochromatic beam. The decrease in intensity of a monochromatic beam is proportional to the thickness of the absorbing material

and can be expressed with the differential equation:

$$dI = -\mu \cdot I \cdot dx \tag{3.1}$$

where

dI = change of the intensity of the beam passing through the absorbing medium

x = length of beam passing through absorbing medium

μ = attenuation coefficient

With the boundary condition $I = I_0$ at $x = 0$ integration of the above differential equation yields the Beer-Lambert Law:

$$I = I_0 \cdot e^{-\mu x} \tag{3.2}$$

Introducing k for the mass attenuation coefficient and δ for the medium density. The amount of radiation absorbed by the material is governed by (for mono energetic beams), where L is the integrated length of the beam path:

with

$$\mu = k \cdot \rho$$

eq. (3.2) becomes:

$$I = I_0 \cdot e^{-k \cdot \rho \cdot L} \tag{3.3}$$

As the beam passes through the absorbing material, energy losses are due to absorption and scattering. Scattering is the effect where the beam changes its initial direction and does not reach a receiver placed along the original beam path (Figure 3.8). With the term Λ for the scattering coefficient and τ as the true absorption coefficient it follows:

$$k = \Lambda + \tau \tag{3.4}$$

The effect of scattered radiation reaching a receiver on another path is reduced by means of a lead diffraction shield (Figure 3.5). The shield is made out of 2.54 cm wide lead strips which are mounted parallel to the x-ray path to the image

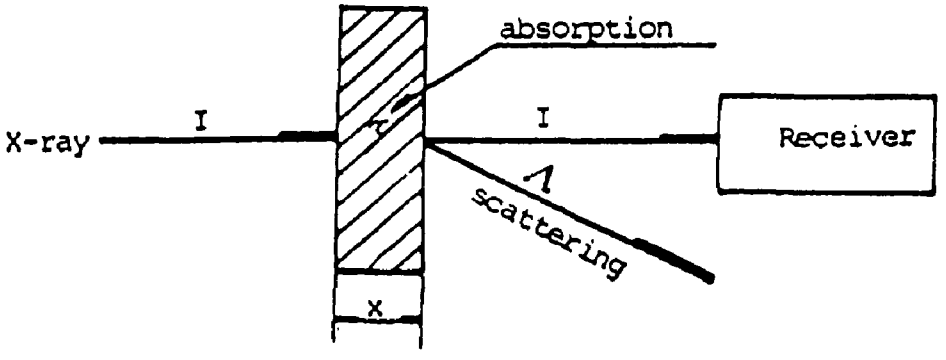

Fig. 3.8 X-ray Absorption and Scattering.

intensifier screen. The x-rays which pass straight through the absorbing medium are not influenced by the lead shield. Scattered beams which strike the intensifier screen at an angle are absorbed by the lead shield.

To demonstrate the validity of the exponential law (eq. 3.3) for this x-ray system seven boxes of varying widths (1.27 - 15.2 cm) were made out of plexiglas. The wall thickness is 0.63 cm which is similar to the thickness of the wall of the riser tube. The intensity of a beam passing through the box filled with solid can be described in the following way (Fig. 3.9):

$$\ln \frac{I_{(w+s)}}{I_0} = -(k \cdot \rho)_w \cdot (\overline{GA} + \overline{BH}) - (k \cdot \rho)_s \cdot (\overline{AB}) \qquad (3.5)$$

with the subscripts w = wall and s = solid. I_0 is the reference beam detecting the intensity of the x-ray source. The attenuation of the walls using the appropriate boxes is:

$$\frac{I_w}{I_0} = -(k \cdot \rho)_w \cdot (\overline{GA} + \overline{BH}) \qquad (3.6)$$

Combining eq. (3.5) and (3.6) leads to the detection of the absorption of the solids as a function of the distance traveled L:

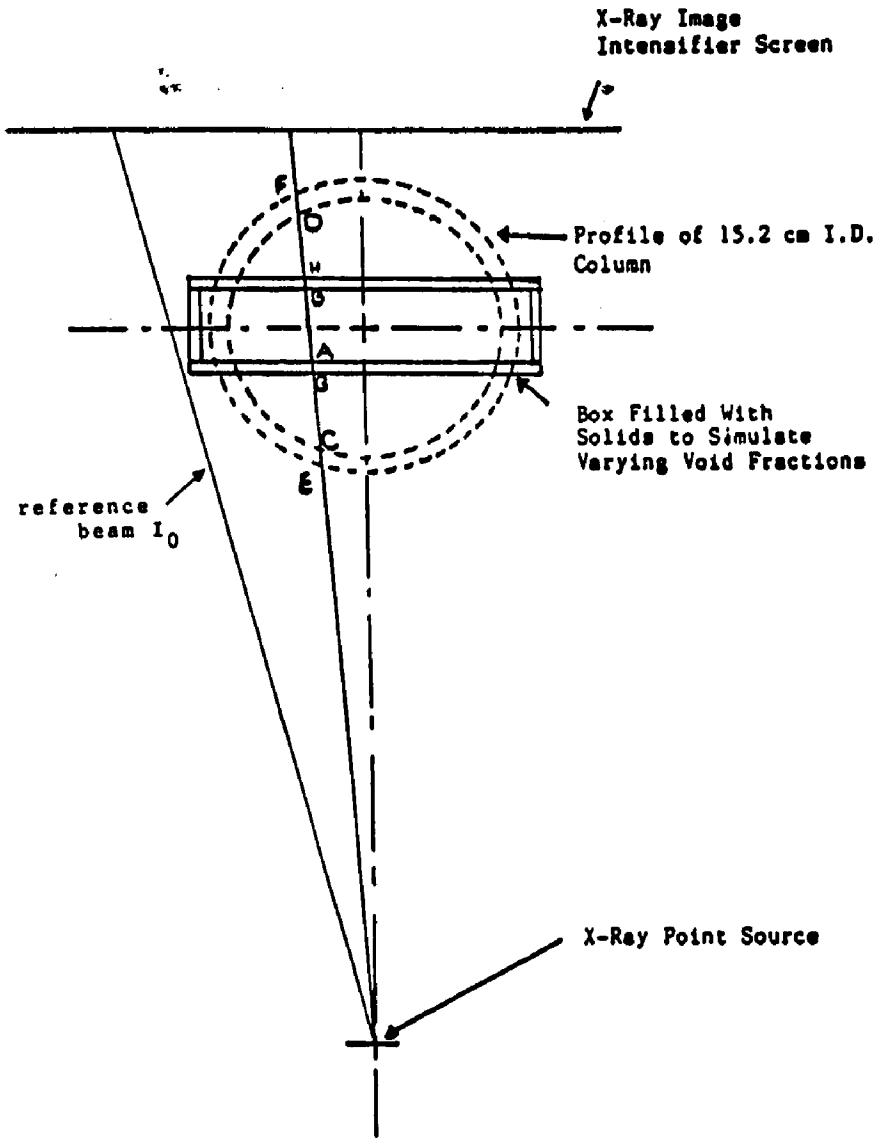

Fig. 3.9 Schematic Setup for Photo Transistor Calibration.

$$\ln\frac{I_{(w+s)}}{I_0} - \ln\frac{I_w}{I_0} = -(k \cdot \rho)_s \cdot (\overline{AB}) \qquad (3.7)$$

To avoid errors because of possible changes of the intensity in the x-ray source, the reference beam I_0 is monitored during all measurements and calculations. Figure 3.10 shows a typical calibration curve of a phototransistor located in the middle of the bed. The plot shows a straight line and demonstrates that the exponential law is valid for this experimental setup. The absorption coefficient k can be obtained from Figure 3.10 by dividing the slope of the curve by the solid density of the packed bed.

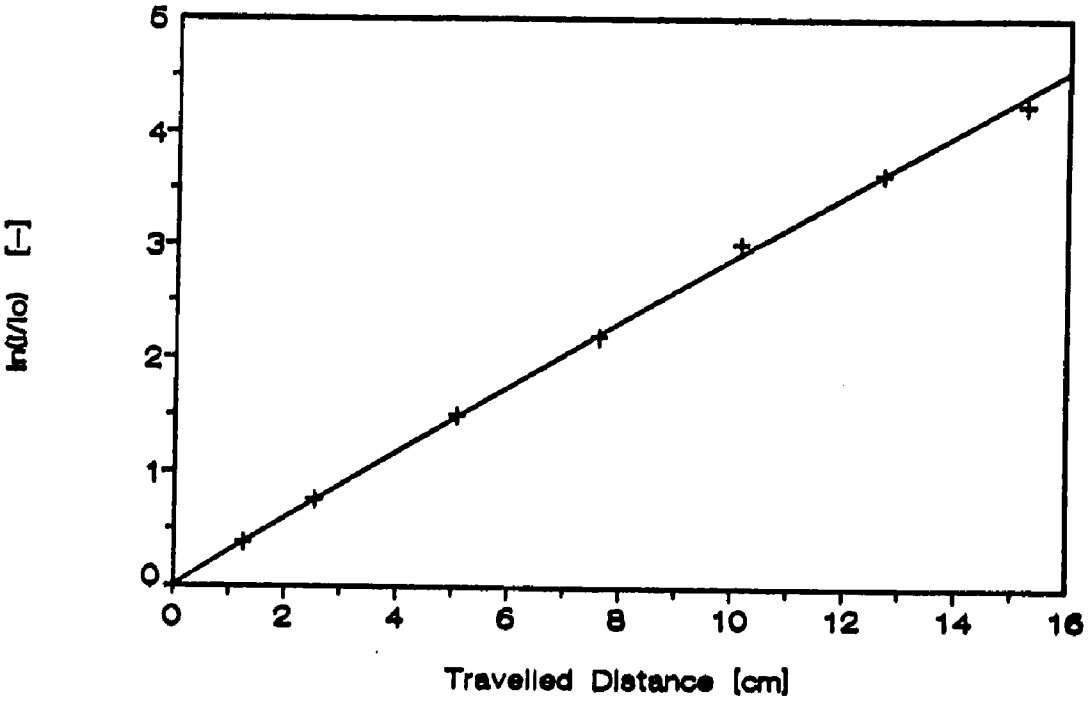

Fig. 3.10 Calibration Curve of a Phototransistor Located in the Middle of the Bed.

3.4.4 Method of Image Reconstruction

When the photon beam passes through a non-homogeneous suspension the detected attenuation is the integral of the local attenuation along the beam path. Suppose $\xi(x,y)$ is the local solid fraction, the detected intensity then is actually given by (Figure 3.11):

$$\ln\frac{I_{(w+s)}}{I_0} - \ln\frac{I_w}{I_0} = -\int_A^B k \cdot \xi(x,y) \cdot ds \qquad (3.8)$$

With the assumption of axial symmetry the local solid fraction distribution $1-\epsilon(r)$ is then reconstructed as a function of the radius. The movable coordinates x and y in Figure 3.9 are related to r by $r = \sqrt{x^2 + y^2}$. The solid density function can be expressed in a polynomial form such that:

$$\rho(r) = a_0 + a_1 \cdot r + a_2 \cdot r^2 + ... + a_n \cdot r^n \qquad (3.9)$$

with the boundary conditions

$$\frac{\partial \rho(r)}{\partial r} = 0 \qquad \text{at } r = 0 \qquad (3.10)$$

eq. (3.9) becomes:

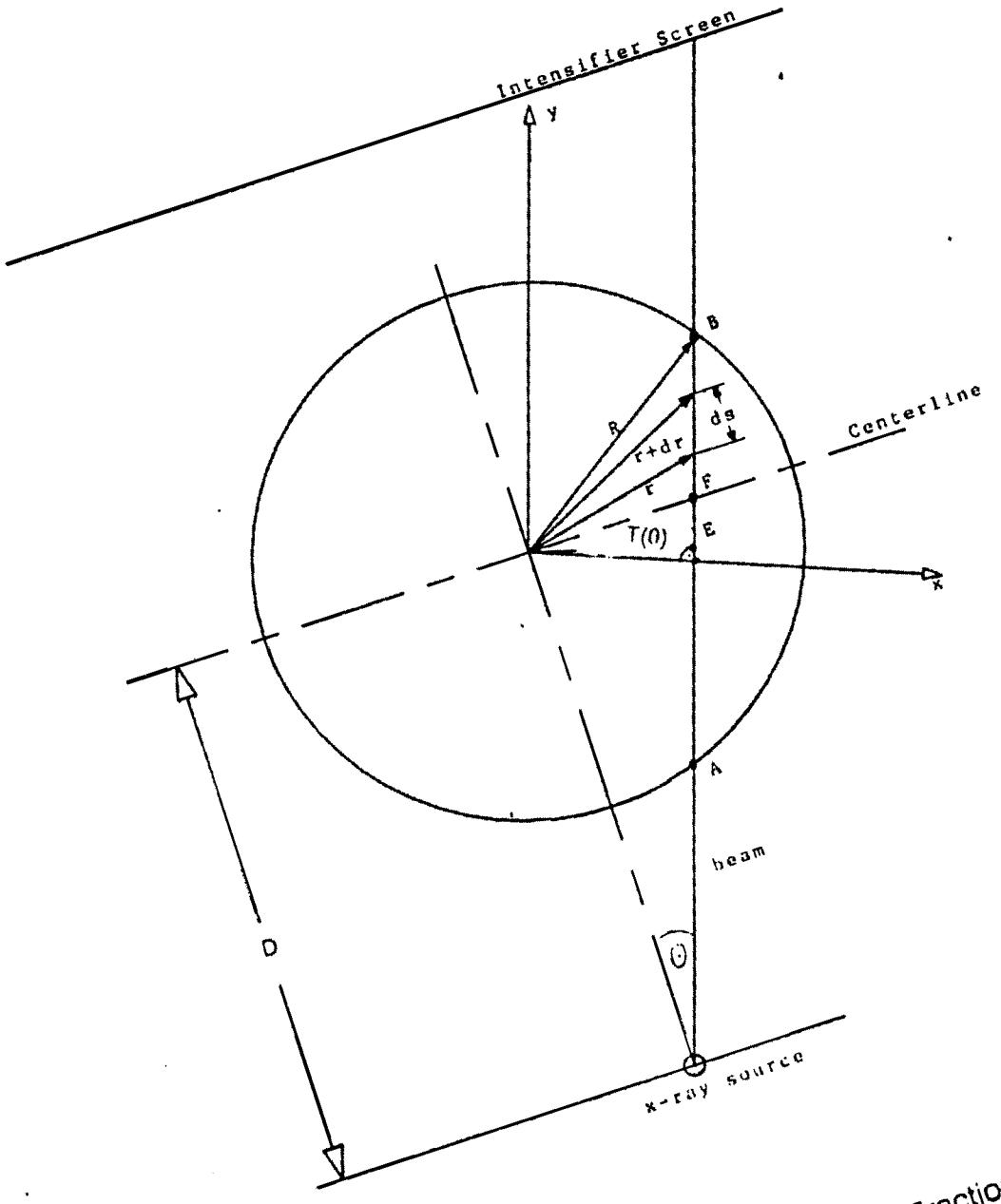

Fig. 3.11 Geometry for Reconstruction of Solid Fraction Distribution.

$$\rho(r) = a_0 + a_2 \cdot r^2 + ... + a_n \cdot r^n \tag{3.11}$$

Eq. (3.8) now can be written:

$$\ln\frac{I_{(w+s)}}{I_0} - \ln\frac{I_w}{I_0} = -\int_A^B k \cdot \rho(r) \cdot ds \tag{3.12}$$

The integration along the beam path from A to B is equal to twice the integration from either A to E or E to B. In eq. (3.13) the left hand value can be obtained from the detected intensity of the photon beam (see eq. 3.12). For a third order polynomial function P_0, P_2 and P_3 can be determined with the geometric relations:

$$x = T(\theta) = D \cdot \sin\theta$$

$$y = s, \quad dy = ds$$

$$\int_0^{s/2} \rho(r) \cdot ds = \int_0^{y_2} (a_0 + a_2 \cdot r^2 + a_3 \cdot r^3)\, dy$$

$$= a_0 \cdot P_0 + a_2 \cdot P_2 + a_3 \cdot P_3 \qquad (3.13)$$

$$r = \sqrt{x^2 + y^2} = \sqrt{y^2 + D^2 \cdot \sin\theta}$$

$$\frac{s}{2} = \frac{AB}{2} = y_2 = \sqrt{R^2 - D^2 \cdot \sin^2\theta}$$

$$P_0 = y_2$$

$$P_2 = \int_0^{Y_2} (T^2(\theta) + y^2)\, dy = T^2(\theta) \cdot y_2 + y_2^3$$

$$P_3 = \int_0^{y_2} (T^2(\theta) + y^2)^{\frac{3}{2}}\, dy$$

$$= \frac{y_2}{4} \cdot (y_2^2 + T^2(\theta))^{\frac{3}{2}} + \frac{3}{8} \cdot T^2(\theta) \cdot y_2 \cdot \sqrt{y_2^2 + T^3(\theta)}$$

$$+ \frac{3}{8} \cdot t^4(\theta) \cdot [\ln(y_2 + \sqrt{y_2^2 + T^2(\theta)}) - \ln T(\theta)] \qquad (3.14)$$

The result is a set of equations with three unknowns a_0, a_2 and a_3. Writing the set in matrix form leads to the problem Ax = y, which can be solved for x by means of the Gauss-Jordan elimination procedure. Integration of the solid density distribution $\rho(r)$ over the radius gives the average void fraction of the cross-sectional area.

The distance travelled by the photon beam to each appropriate photodetector are determined by the following procedure: The intensity of a beam passing through a packed bed with known solid fraction $(1-\epsilon)$ is scanned with one row of the phototransistors. In this case $\rho(r)$ is constant. Equation (3.12) gives the length of the travel distance of the photon beam through the absorbing medium with the absorption coefficient k obtained by the calibration procedure of section 3.6.

To reconstruct the density distribution by means of the third order polynomial in equation (3.14) the values for the length obtained by the above mentioned calibration procedure are applied. The profiles for a homogeneous void fraction in Fig. 3.12 represent an empty and slumped or packed bed very well. Due to changes in moisture content of the catalyst for all experiments the slumped bed was used to adapt the parameters like attenuation coefficient and travel distance of the x-ray beams.

An illustration of the dynamic response of the x-ray system in comparison with pressure measurements is done for the slugging fluidization regime. All data are converted into solid fraction (1-ϵ). The x-ray data are the cross sectional average obtained by integrating the third order polynomial function over the cross sectional area. Fig. 3.13 and 3.14 show the time series and the power spectrum of a slugging bed, both x-ray and pressure signal describe the slugs very well.

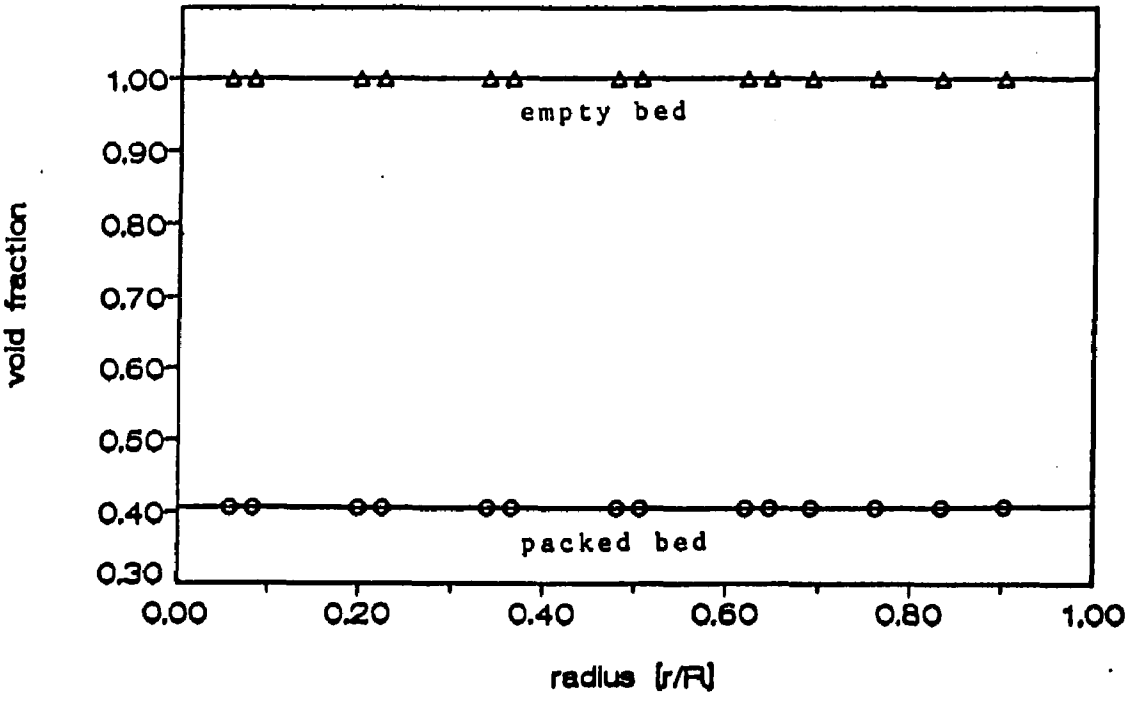

Fig. 3.12 Density Profile of Packed Bed and Empty Tube.

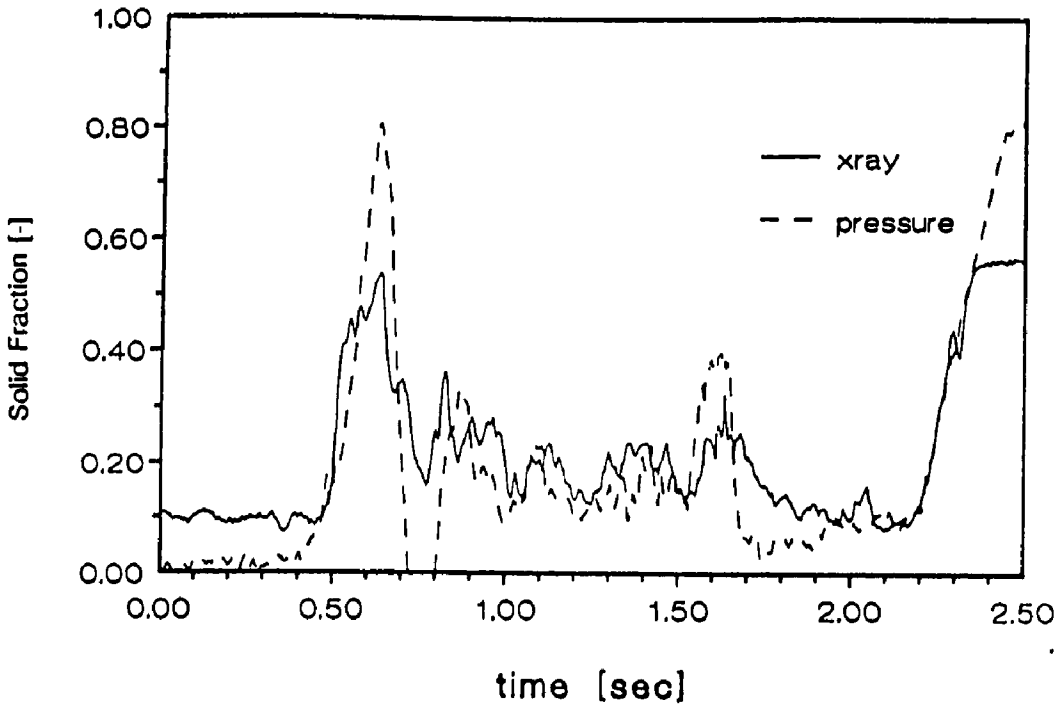

Fig. 3.13 Time Series of a Slugging Bed.

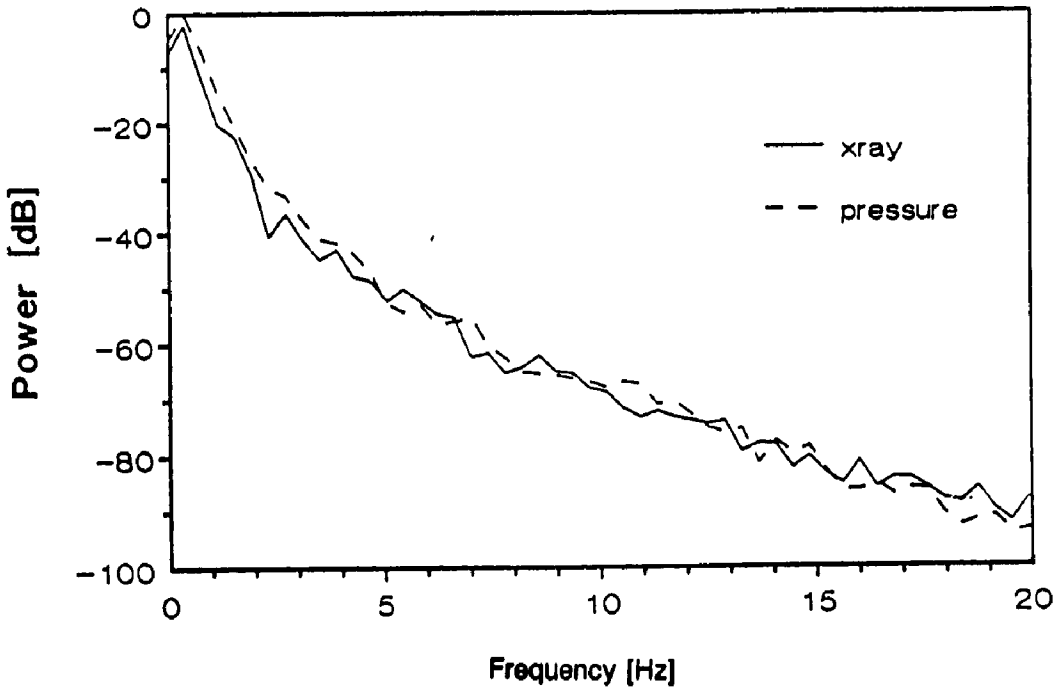

Fig. 3.14 Power Spectrum of a Slugging Bed.

3.4.5 Order of Polynomial

The x-ray image of each cross section at a given height is detected by means of fourteen photo detectors. Nine detectors are on the left half and five are on the right half of the column. To determine the appropriate profile of the solid fraction as a function of the radius and the average value of the solid fraction, the order of the polynomial used to fit the data has to be defined. The development of the polynomial function is shown in the previous section.

A preliminary experiment was conducted in the dense phase of a riser at a superficial gas velocity of 3 m/s and a solid flow rate of 140 kg/m^{2}s. The data were collected with a sampling rate of 5 msec over a time period of 3 minutes. Second, third,etc. up to ninth order polynomials were integrated fitting the root mean square averaged experimental data. To compare the fits with the measured data the polynomial results were integrated over the chords "seen" by the transducers. It is shown in table 3.2 that polynomials of lower order produce a lower value in the wall region ($r/R \approx .9$) which results in a slightly lower average solid fraction. Higher order polynomials give a better data fit but tend to have a more oscillating character (Fig. 3.15d to f). Polynomials up to fourth order show a smoother solid profile (Fig. 3.15a,b and c) which is similar to the density profiles obtained with different measurement techniques, for example the Laser doppler system in Fig. 2.10. Shao (1986) using the City College x-ray system with a film

plate concluded in her work that lower order polynomials are appropriate for reconstructing the image. Higher order polynomials in her work showed an anomalous behavior.

The average solid fraction of the cross section is given in Table 3.2 at two different heights above the air inlet. No significant dependence on the order of the polynomial exists. It can be concluded then, that the third order polynomial is sufficient to fit the experimental data. The local voidage of the fast fluidized bed as well as the cross sectional average are described well. For the course of this work a third order polynomial was used to treat the optical readings from the photo detectors.

Table 3.2 Solid Fraction of the Cross Sectional Area

		Order of Polynomial					
Height [m]	solid frac.	2	3	4	5	6	7
1.20		0.2165	0.2166	0.2163	0.2093	0.2178	0.2216
2.60		0.2108	0.2109	0.2107	0.2119	0.2108	0.2125

Table 3.3 Comparison between Experimental and Calculated Data at U_g = 3 m/s, G_s = 140 kg/m^{2}s.

r/R	Y(r)	PY(r	2.	3.	4.	5.	6.	7.	8.	9.
0.9016	0.8389	0.7223	0.6904	0.7046	0.7656	0.7656	0.7752	0.7793	0.7797
0.832	0.9741	0.971	0.9579	0.9778	1.0207	1.0204	1.0213	1.0221	1.0225
0.7612	0.7894	0.7219	0.7848	0.8204	0.7782	0.776	0.7823	0.7526	0.7506
0.6903	0.9285	0.9318	1.0133	1.0277	0.9845	0.9847	0.9817	0.9814	0.9817
0.6194	0.8765	0.7881	0.8915	0.8699	0.8216	0.8222	0.8299	0.8364	0.838
0.479	0.9875	0.9079	1.002	0.9469	0.9706	0.9708	0.981	0.9844	0.9844
0.3386	0.9277	0.8706	0.9197	0.9011	0.9662	0.9651	0.9528	0.9455	0.9441
0.1982	0.8665	0.7696	0.7583	0.8399	0.8479	0.8482	0.8554	0.8595	0.8605
0.0577	1.1768	1.4518	1.2544	1.2212	1.179	1.1791	1.1766	1.1756	1.1754

Y is experimental data; **PY** is calculated data

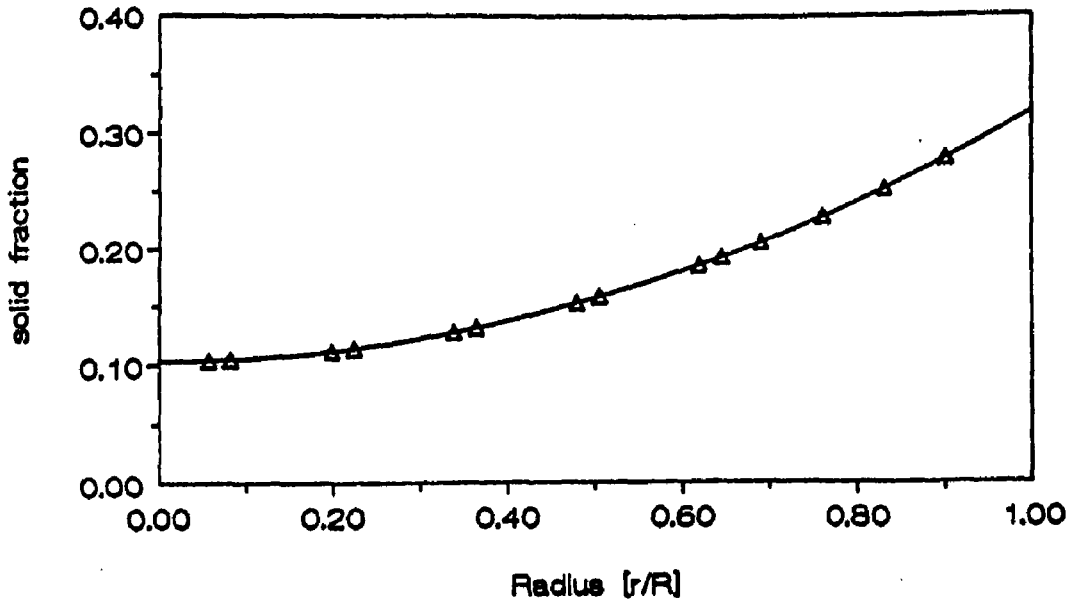

Fig. 3.15a Density Profile of a Second Order Polynomial.

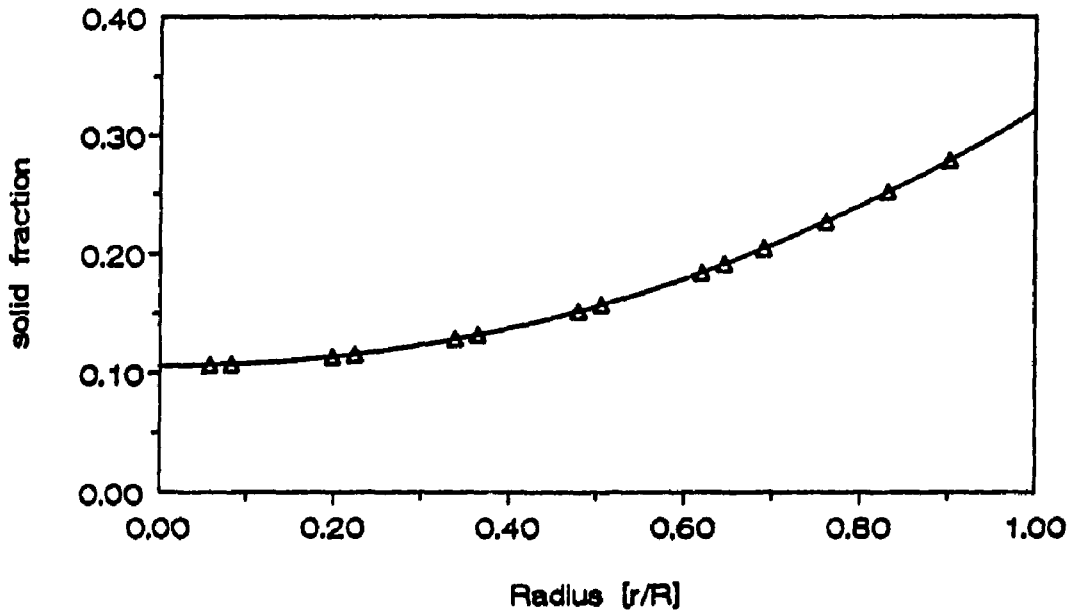

Fig. 3.15b Density Profile of a Third Order Polynomial.

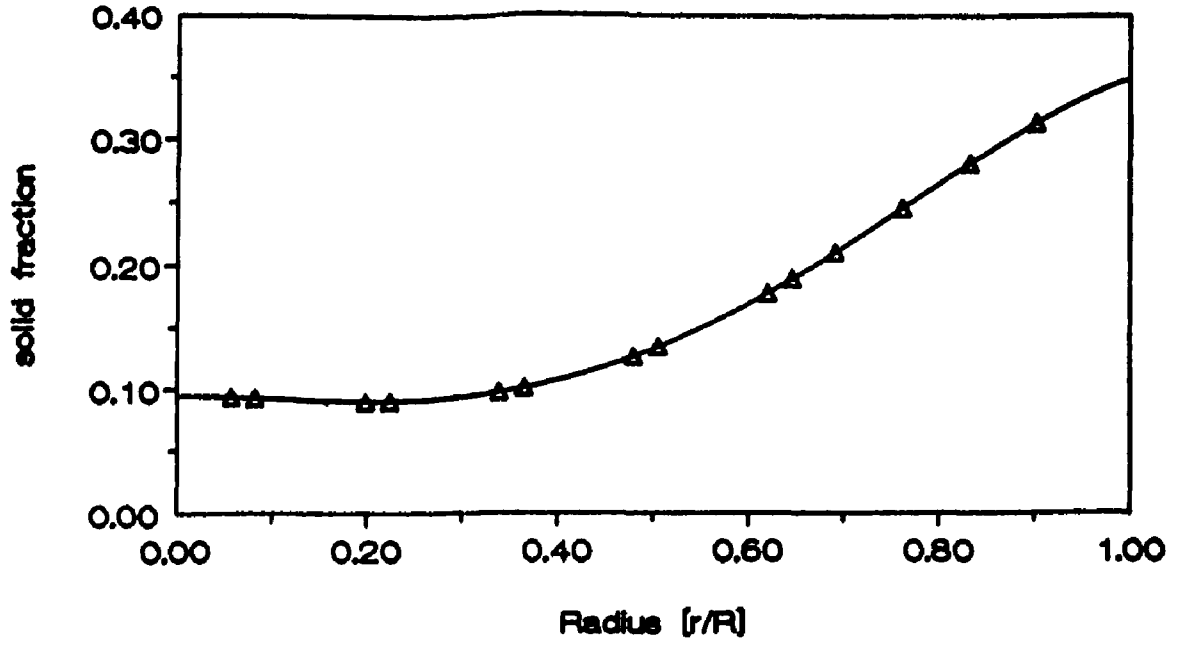

Fig. 3.15c Density Profile of a Fourth Order Polynomial.

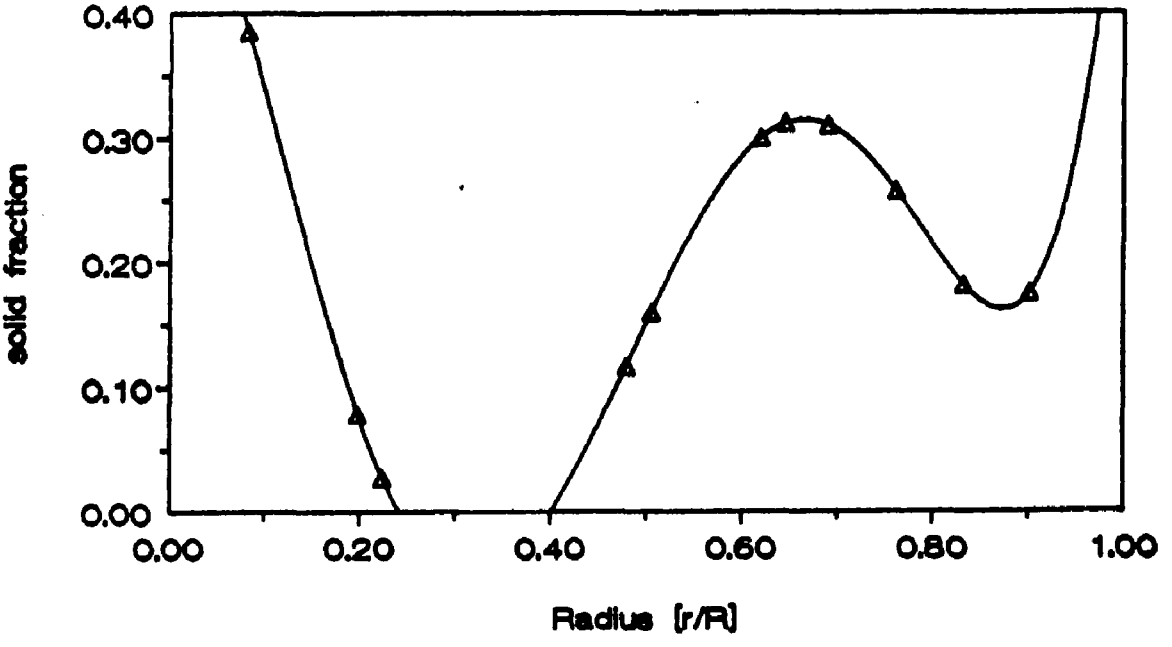

Fig. 3.15d Density Profile of a Fifth Order Polynomial.

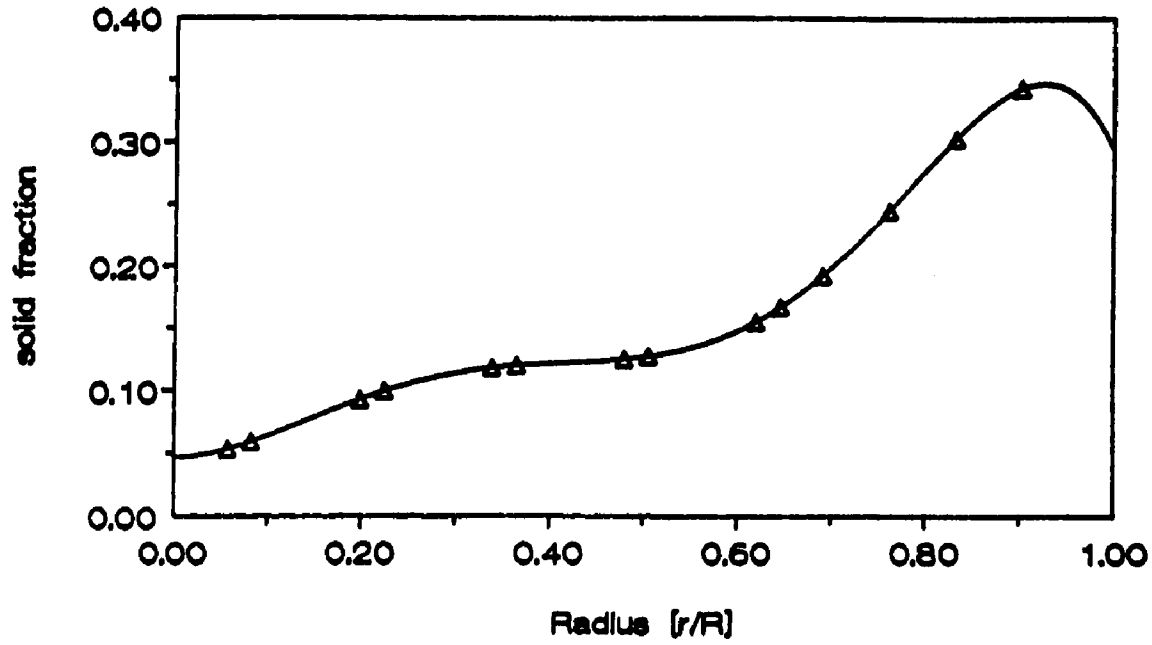

Fig. 3.15e Density Profile of a Sixth Order Polynomial.

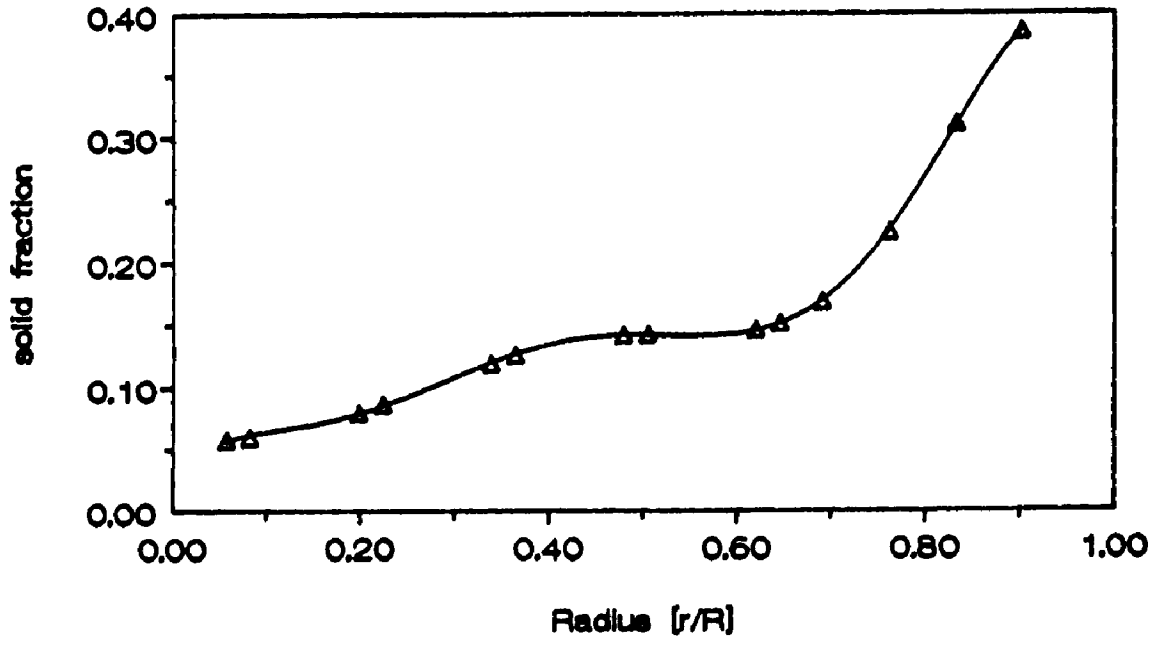

Fig. 3.15f Density Profile of a Seventh Order Polynomial.

4. Experimental Results

4.1 Pressure Fluctuation

The effect of the differential pressure tap spacing on the magnitude of the differential pressure fluctuation can give an indication of the axial scale of any large structures, i. e. turbulent eddies or waves, in the two-phase gas-solid flow.

Two cases, one in the dilute and one in the dense phase both with a moderate superficial gas velocity of U_g = 3 m/s were studied. Data from runs with a spacing of the differential pressure taps of 5 cm, 80 cm and 160 cm were collected simultaneously in one set of experiments and data from runs with a spacing of 12.8 cm and 40 cm were also collected simultaneously in another set of runs. The differential pressure taps with a smaller spacing are located approximately in the middle of the pair of taps with the wider spacing. To ensure no measurements were taken in the entrance or exit region of the riser the lowest pressure probe was mounted 3 m above the air inlet. All pressure readings were converted to apparent solid fraction to allow a comparison with x-ray measurements (eq. 4.1). A negative apparent solid fraction results when a negative pressure difference is detected.

$$(1 - \varepsilon)_{app} = \left(\frac{1}{\rho_s \cdot g}\right) \cdot \left(-\frac{dp}{dx}\right) \qquad (4.1)$$

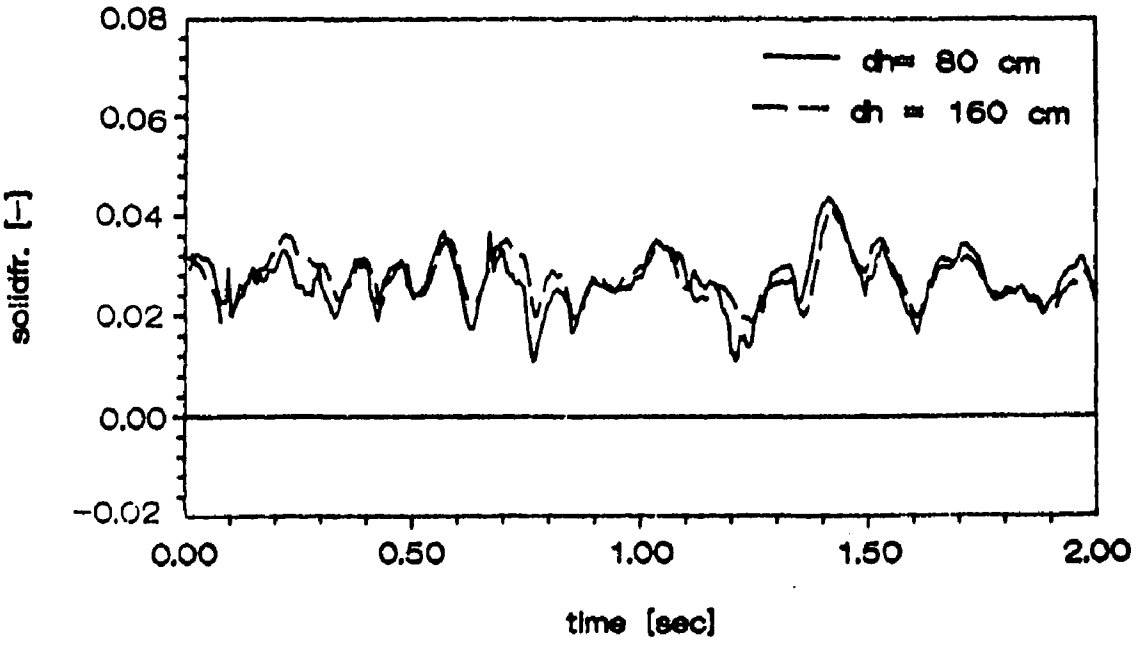

Fig. 4.1a Solid Fraction Fluctuation Derived from Pressure Measurements in Dilute Phase, dH = 80 cm and dH = 160 cm, G_s = 54 kg/m^{2}s.

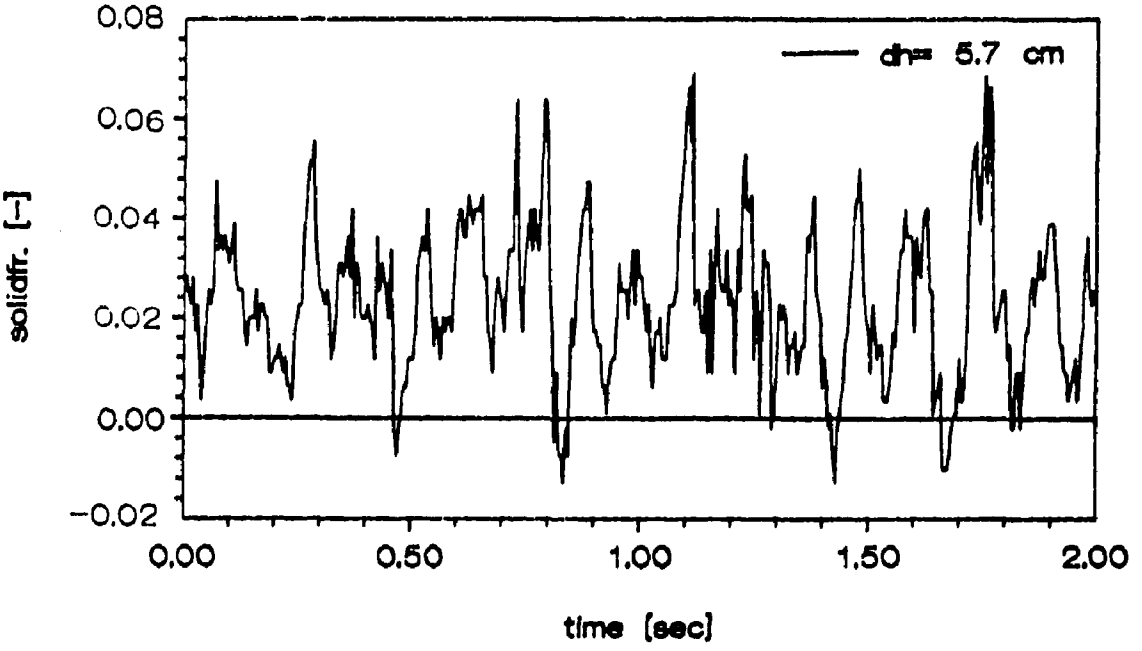

Fig. 4.1b Solid Fraction Fluctuation Derived from Pressure Measurements in Dilute Phase, dH = 5 cm, U_g = 3 m/s, G_s = 54 kg/m^{2}s.

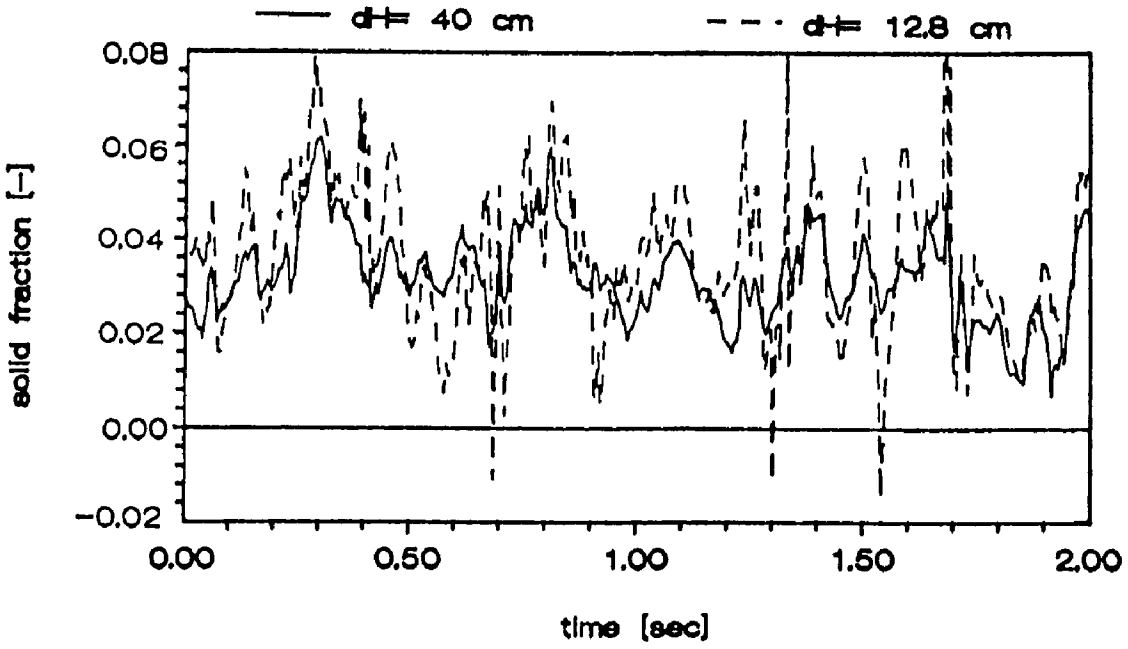

Fig. 4.2 Solid Fraction Fluctuation Derived from Pressure Measurements in Dilute Phase, dH = 12.8 cm and dH = 40 cm, U_g = 3 m/s, G_s = 54 kg/m^{2}s.

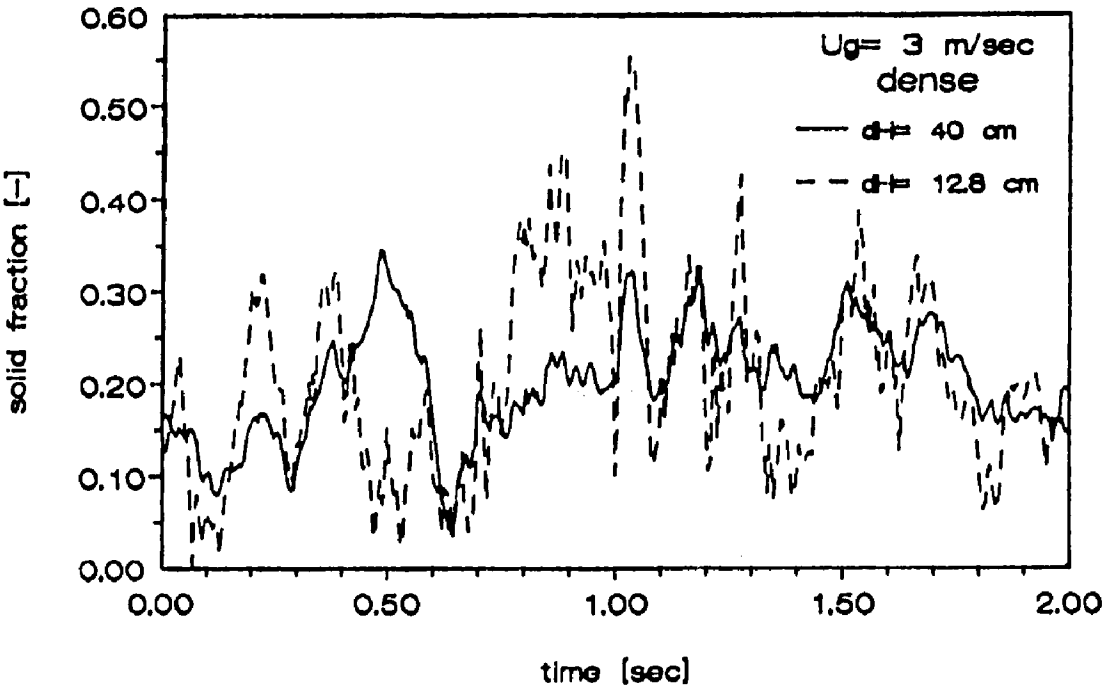

Fig. 4.3 Solid Fraction Fluctuation Derived from Pressure Measurements in Dense Phase, dH = 12.8 cm and dH = 40 cm, U_g = 3 m/s, G_s = 140 kg/m^{2}s.

Table 4.1 Dense and Dilute Phase with U_g = 3 m/s.

	Dense Phase					Dilute Phase				
dH [cm]	5	80	160	10	40	5	80	160	10	40
$1-\epsilon$	.2103	.2104	.2036	.2132	.2050	.0327	.0300	.0298	.0334	.0293
σ	.2196	.0514	.0319	.0752	.1369	.0294	.0084	.0068	.0170	.0091
$\sigma/(1-\epsilon)$	1.044	.2444	.1565	.3670	.6419	.8995	.2789	.2277	.5085	.3117

The time series of the measurements in the dilute phase are shown in Fig. 4.1a, 4.1b and 4.2 for different spacing. The pressure readings with a spacing of 80 cm or more show a very damped response. Both the frequency spectra and the amplitudes of the fluctuations are similar when the tap spacing is large. Decreasing the distance between the probes (Fig. 4.1b and 4.2) gave readings with higher frequencies and higher amplitudes. A sample of the time series in the dense phase is presented in Fig. 4.3 for a spacing of 12.8 cm and 40 cm. Decreasing the spacing of the taps in the dense phase increases, as in the dilute phase, amplitude and frequency of the fluctuations. The difference between the two phases is that the amplitude of the fluctuations and the mean pressure gradient in the dense phase is approximately ten times larger then in the dilute phase (Fig. 4.2 and Fig. 4.3). Also it is important to note that the mean apparent solid fraction calculated from the Δp increases with decreasing spacing (Table 4.1).

Visual and x-ray observations during the course of the experiments showed an oscillating up and down flow in the wall region both from outside through the plexiglass wall and with the video monitor of the x-ray system. With these observations in mind the Probability Density Functions (PDF's) of the pressure readings with different spacing are informative. PDF's with a spacing of more then 40 cm give a more or less symmetric shape (Fig. 4.4 and Fig. 4.5) resulting from a more damped response compared with the highly skewed PDF's obtained with the smaller spacings. This also can be seen in the time series (Fig. 4.1). These

changes in the PDF's with spacing imply that the length scale of the oscillations is small enough to be averaged out in the 80 cm spacing but large enough to be visible with a 40 cm spacing.

Decreasing the spacing to less then 40 cm gives a more asymmetric shape of the PDF's (Fig. 4.4 and Fig. 4.5). These pressure fluctuation readings are mainly the result of local disturbances in the wall region. For a riser of 15 cm diameter for example a 1.5 cm fluid wall region covers one third of the cross sectional area. Also the solid fraction in the wall region is higher due to the core annulus structure of the flow. The huge fluctuations of the readings using a smaller spacing may be explained as the result of the accelerations and decelerations added to the solid fraction changes in this oscillating wall region.

For further understanding it is necessary to look at the dense and dilute phase separately. The power spectra in Fig. 4.6a and 4.6b for the dense phase are particularly interesting since all the spectra exhibit a significant peak at a frequency of approximately one Hz. The cause of this superimposed low frequency may be explained by the up and down movement of the inflection point observed with the on-line pressure profile readings. Furthermore the curves of the power spectra fall off very rapidly for the readings with a spacing larger then 5 cm. The power spectrum in Fig. 4.6a for the spacing of 5 cm falls sluggishly reaching a frequency of approximately 14 Hz. This indicates the existence of higher than one Hz

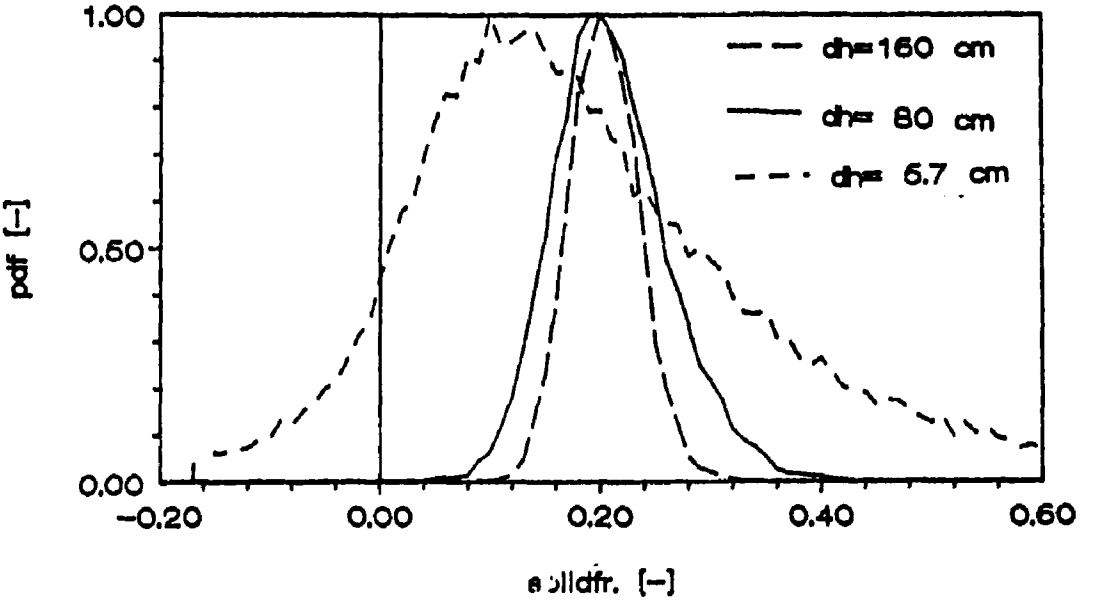

Fig. 4.4a PDF of Pressure Fluctuation in a Dense Phase, U_g = 3 m/s; dH = 5 cm, 80 cm and 160 cm, G_s = 140 kg/m^{2}s.

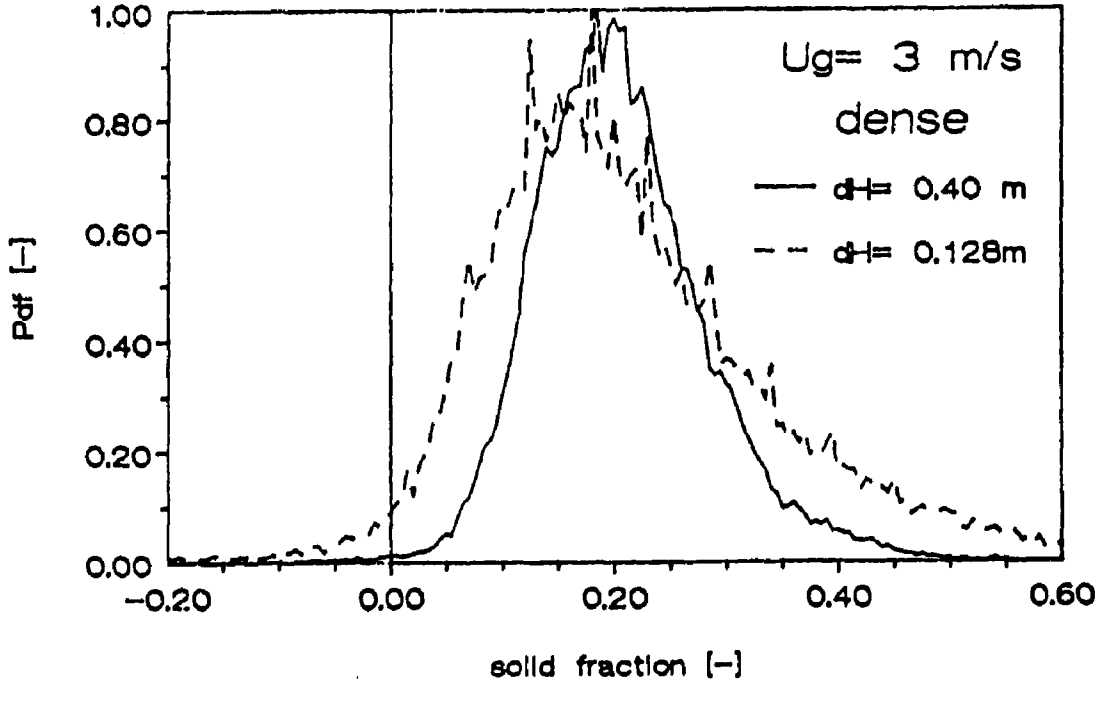

Fig. 4.4b PDF of Pressure Fluctuation in a Dense Phase, U_g = 3 m/s; dH = 12.8 m and 40 cm, G_s = 140 kg/m^{2}s.

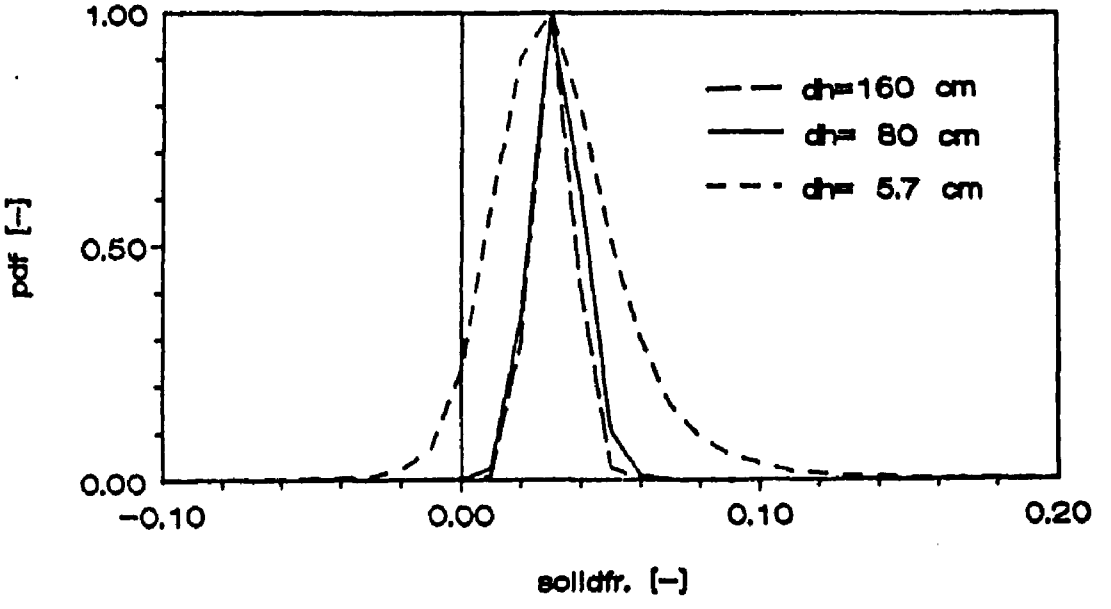

Fig. 4.5a PDF of Pressure Fluctuation in a Dilute Phase U_g = 3 m/s; dH = 5 cm, 80 cm and 160 cm, G_s = 54 kg/m^{2}s.

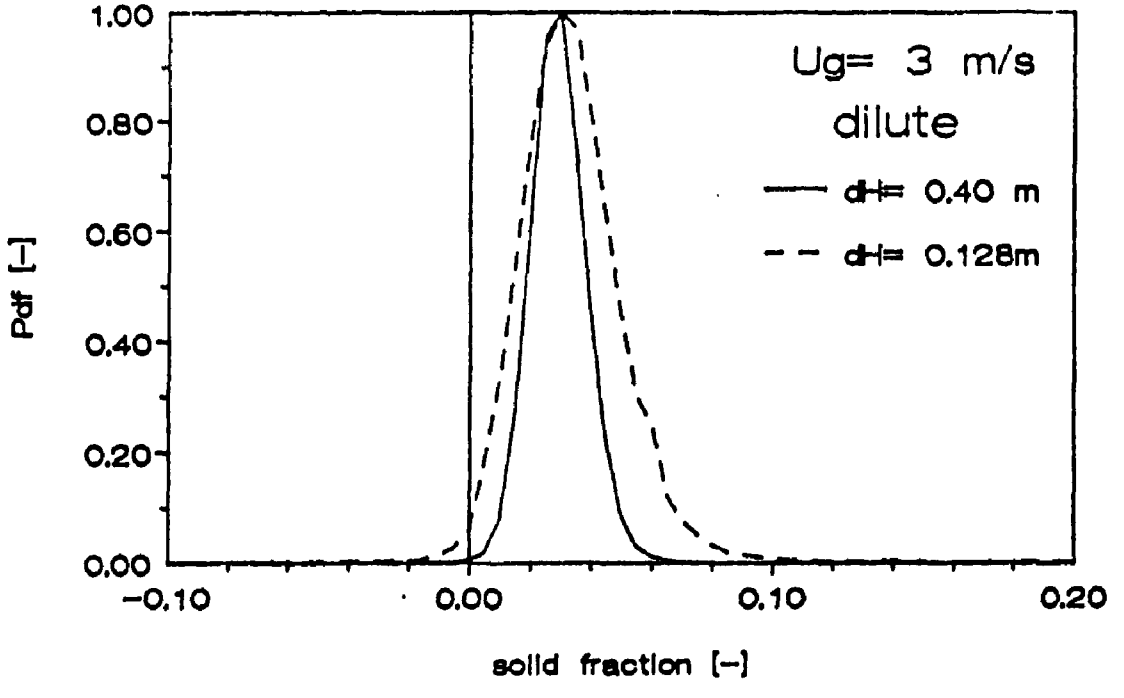

Fig. 4.5b PDF of Pressure Fluctuation in Dilute Phase, U_g = 3 m/s; dH = 12.8 cm and 40 cm, G_s = 54 kg/m^{2}s.

fluctuations which are local turbulence or density waves in addition to the low frequency oscillations. Schnitzlein (1987), using the City College facility, detected a density wave speed of 1.6 m/s in the dense phase for superficial gas velocities from 1.0 m/s to 5.0 m/s. The relationship between wave speed U_w, the frequency f and the wave length λ may be expressed as:

$$\lambda = \frac{U_w}{f} \qquad (4.2)$$

To calculate the frequency f a wave length or another characteristic length has to be defined. Similar to the methods of homogeneous turbulence a characteristic scale can be obtained by plotting the variance, σ, of the PDF's of pressure readings divided by the solid fraction against the dimensionless spacing (Fig.4.8.). The tangents of the horizontal and vertical legs of the curves intersects at a L/D ratio of approximately 1.1 which gives a magnitude for the length scale of ~ 17 cm. With eq. 4.2 a length scale of 17 cm and a wave speed of 1.6 m/s gives a frequency of ~ nine Hz which is in the range of fluctuations below ten Hz.

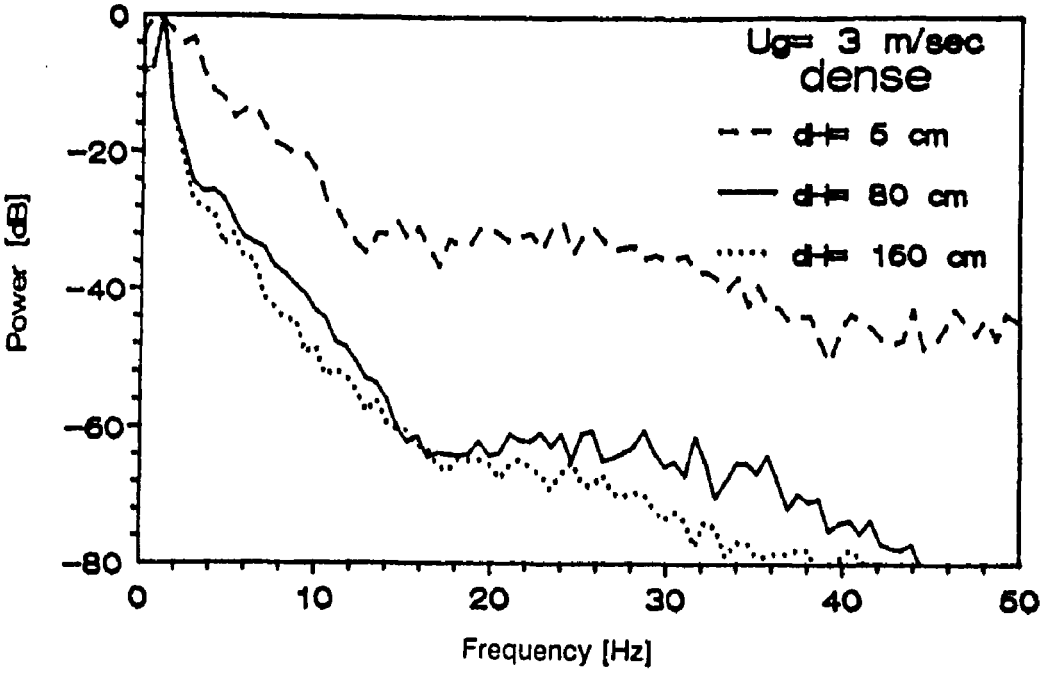

Fig. 4.6a Power Spectrum of Pressure Fluctuations in a Dense Phase, U_g = 3 m/s, dH = 5 cm, 80 cm and 160 cm, G_s = 140 kg/m^{2}s.

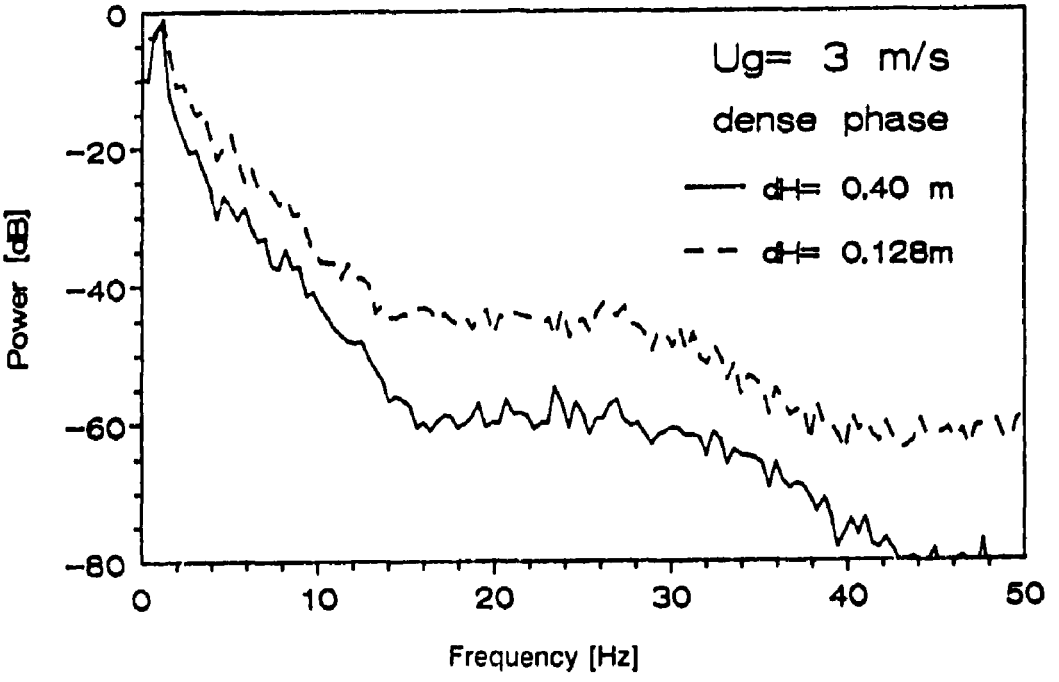

Fig. 4.6b Power Spectrum of Pressure Fluctuation in a Dense Phase, U_g = 3 m/s, dH = 12.8 cm and 40 cm, G_s = 140 kg/m^{2}s.

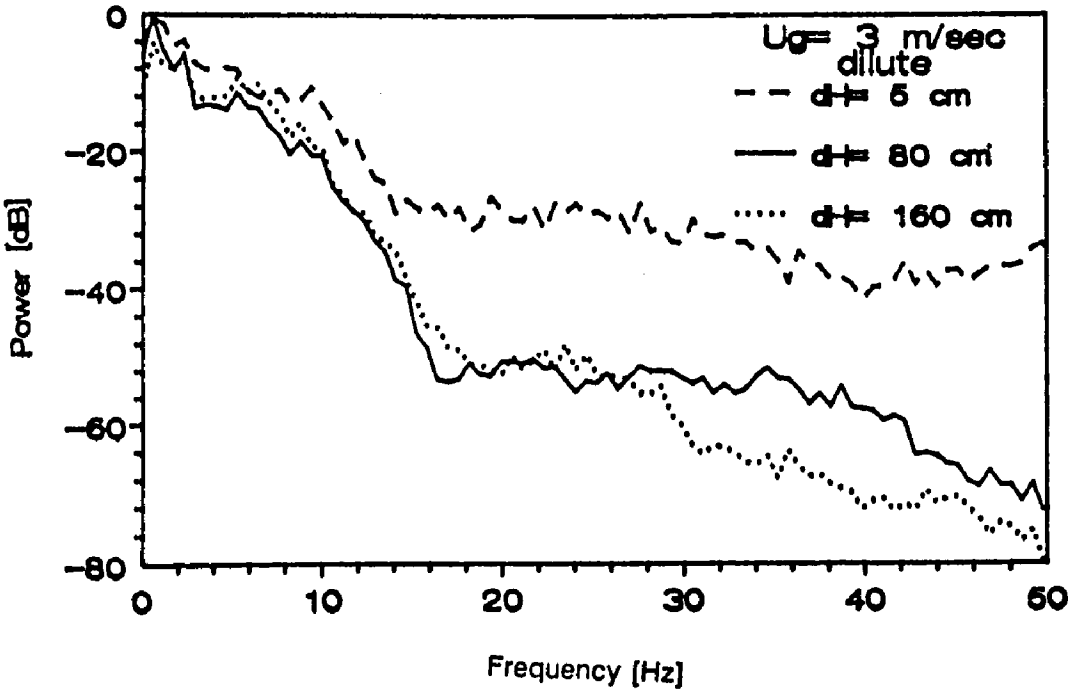

Fig. 4.7a Power Spectrum of Pressure Fluctuations in a Dilute Phase, U_g = 3 m/s, dH = 5 cm, 80 cm and 160 cm, G_s = 54 kg/m^{2}s.

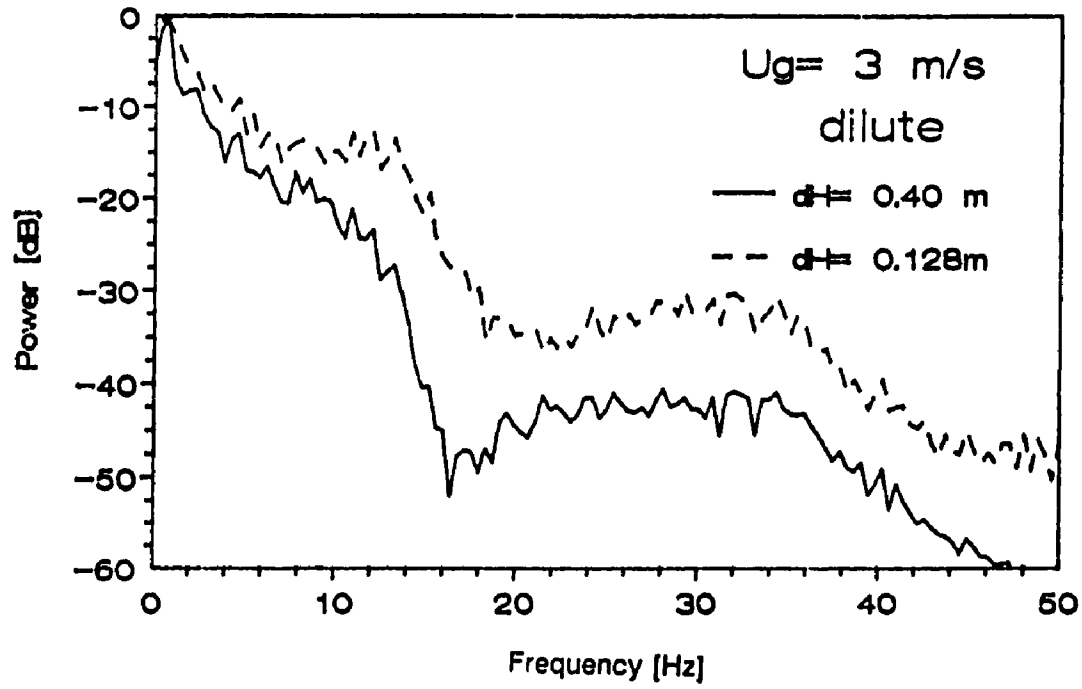

Fig. 4.7b Power Spectrum of Pressure Fluctuations in a Dilute Phase, U_g = 3 m/s, dH = 12.8 cm and 40 cm, G_s = 54 kg/m^{2}s.

The power spectra of the dilute phase in Fig. 4.7a and Fig. 4.7b also show a significant peak at a low frequency of one Hz and a more sluggish fall off for the taps with a smaller spacing. It is interesting that there is a second peak for the probes with a spacing of 5 cm and 12.8 cm in the range of 10 - 14 Hz. As in the dense phase, a characteristic length for the dilute phase is of the magnitude of 17 cm. Applying eq. 4.1 with, for example, a frequency of 14 Hz and a wave length of 17 cm gives a wave speed of ~ 2.4 m/s. Schnitzlein (1987) detected wave speeds in the dilute phase of various velocities but always higher than in the dense phase. His measurements show no clear indication of the existence of coherent density waves in the dilute phase as he found in the dense phase.

The low frequency peak may be explained as a natural or resonance frequency of the apparatus. Local fluctuations of the solid appear to exist in the wall region which have a higher frequency than the natural low frequency and a smaller scale than the diameter of the riser. Length scales of the order of 1.1 times the diameter of the riser may be interpreted as large quasi-periodic structures of the flow. It is unclear if the above scales are typical for two phase turbulent flow in general or only for a specific apparatus like the City College facility. Conducting similar experiments in a larger diameter bed (D > 15 cm), would help provide some of the answers.

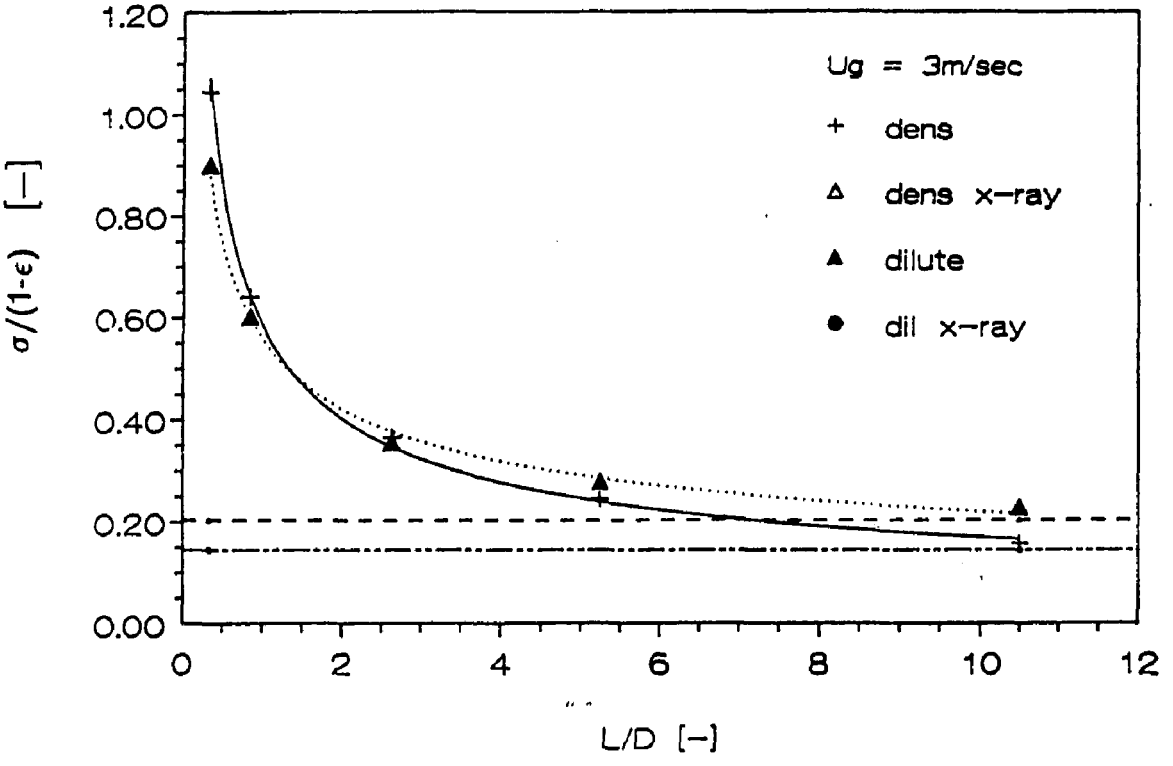

Fig. 4.8 Normalized Variance of Pressure Fluctuations as a Function of the Spacing L/D of the Probes.

4.2 Time Stability and Axial Symmetry

The time stability of data determines how long a record length must be for data to be reproducible. Depending on the frequency range of the fluctuations, the minimum sampling frequency and the number of data points which are necessary are determined. To analyze fluctuation frequencies of, for example the pressure readings, the sample frequency has to be ten times larger than the largest frequency to be analyzed (Paul, 1982). For the course of this work a sampling frequency of 200 Hz was chosen, so the low frequency fluctuations (<20 Hz) can be detected with a negligible error. To obtain reproducible data, the number of data points or the length of the time period for which measurements are analyzed, has to be determined from the lowest frequency possible. X-ray fluctuations, of the cross sectional average of the solid fraction averaged over a time period of five seconds, presented by Shao (1986, Fig. 2.12) indicate clearly that a longer averaging time is necessary. Abed (1984) observed in his paper that a probability density has to be computed from 3-minute time segments to be reproducible in a high velocity fluidized bed operating at steady state conditions.

To demonstrate the dependence of the average solid fraction on the averaging time, an experiment was conducted at a superficial gas velocity of 3 m/s with a solid flow rate of 140 kg/m^2s. The measurements were taken at the end of the entrance region, which explains the difference between the x-ray based values and

the pressure reading based values of the solid fraction in Fig. 4.9. The solid fractions are computed from time segments of 5 seconds, up to 15 minutes. It is seen in Fig. 4.9 that with increasing averaging time the time dependence of the solid fraction decreases. To fall within the $\pm$ 3% error band the pressure fluctuation readings have to be averaged over a time period of three minutes, while x-ray readings only require an averaging time of less than one minute.

To choose the data collecting time one has to balance between accuracy and available data storage capacity. X-ray and pressure fluctuation readings are collected simultaneously which generates a data file of the size of one mbyte for an averaging time of one minute . For the course of this work a data collection time of three minutes was chosen, which permits scanning the riser at ten different heights with the present data acquisition system.

The local solid fraction distribution as a function of the radius is reconstructed from the projected x-ray image with a chordal absorptometry technique (chapter 3.4.4) based on the assumption of axial symmetry. To prove if the assumption of axial symmetry is valid, measurements in the dense phase with a superficial gas velocity of 3 m/s were analyzed. Fig. 4.10 shows three profiles for three consecutive seconds. Each profile is averaged over a time period of one second, so each point of a profile represents an average of 200 readings. The solid fraction is calculated from the "true" reading of each phototransistor and the travel distance of the x-ray

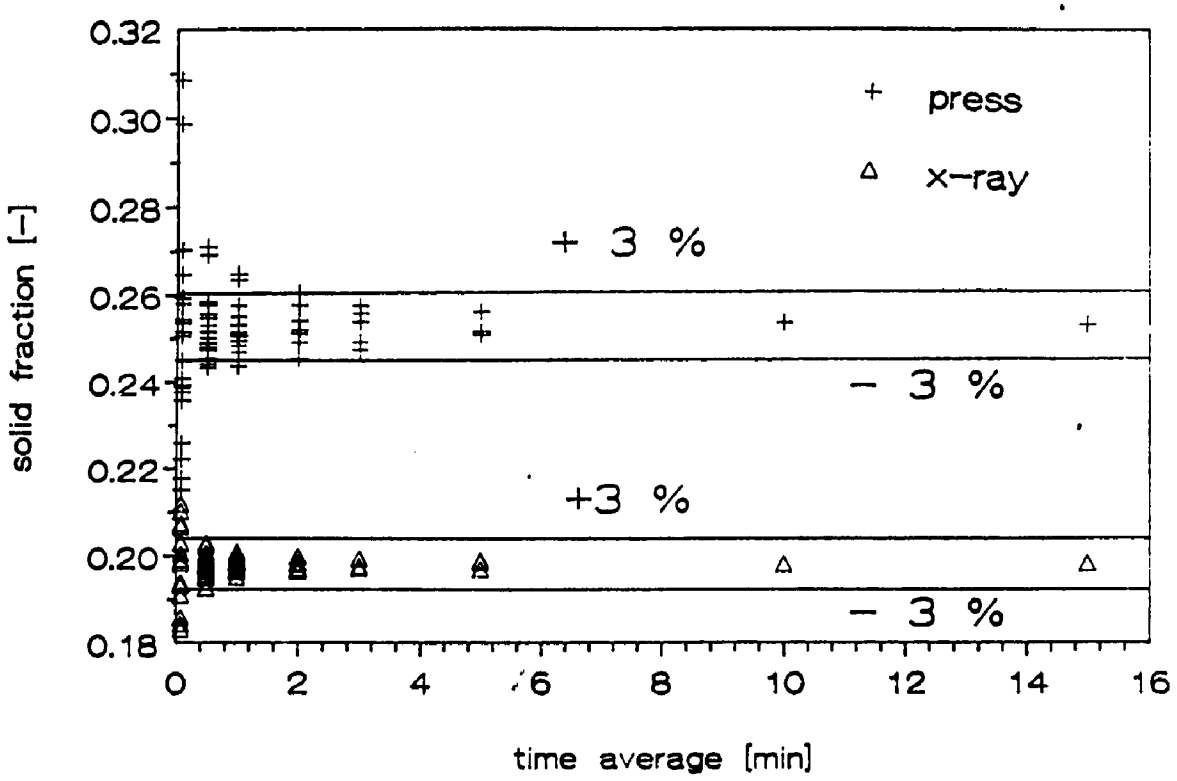

Fig. 4.9 Dependence of Time Average Solid Fraction Fluctuation on the Averaging Time at U_g = 3 m/s, G_s = 140 kg/m_s in the Entrance Region, dH = 40 cm

beam within the riser (eq. 3.7). While during the first second the profile is symmetric, local turbulence caused an asymmetry during the second and third seconds. Especially in the transition between core and wall region a step decrease in the solid fraction is observed.

The same data base as above is used in Fig. 4.11. The density profile here was reconstructed by means of a third order polynomial. The left and right sides of the profiles were calculated separately. Data for the first second again shows a symmetric profile. The effect of the local turbulence in the transition region between core and annulus during the second and third second is seen also in this representation but due to the character of the polynomial the profiles are smoothed. In addition the calculated solid fraction in the core is larger for the second and third seconds than for the first second.

In Fig. 4.12 with the same data the density profiles were also reconstructed by means of a third order polynomial. In this case axial symmetry is assumed. Each profile is calculated with one polynomial function (overlapping the readings from the left to the right half). All profiles therefore must be symmetric. The local disturbance during the second and third seconds is smoothed out. The solid fraction in the core during the first second was low, while during the remaining time the solid fraction in the core region was higher. It is also interesting that the cross sectional average solid fraction in the first second is low while it is the same for the

other two profiles and higher than during the first second.

With the x-ray system the mean solid fraction of the cross section is reproducible when the averaging time is longer than 60 seconds (Fig. 4.9). When the record length is longer than 60 seconds the assumption of axial symmetry is good. In Fig. 4.13 a density profile is shown averaged over a time period of 100 seconds. Integrating the data over a longer time period gives the same shape of the profile. The density profiles in Fig. 4.13 are calculated with a third order polynomial function. For two cases the left and right side of the riser are treated separately. The third case the data are calculated with one polynomial function. It is demonstrated clearly, that the assumption of axial symmetry is good for time averages longer than 60 seconds, and questionable for instantaneous pictures or short time averages.

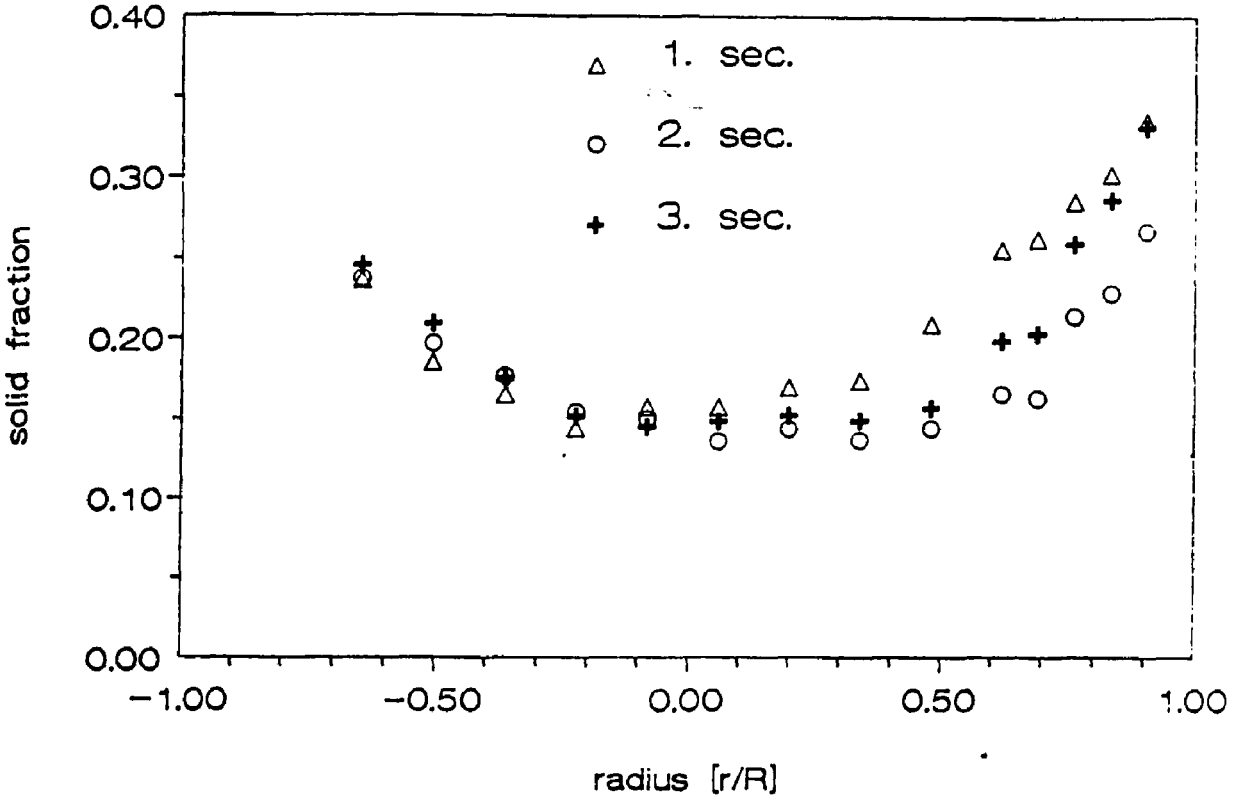

Fig. 4.10 Density Profile derived from "True" Readings of the Phototransistor, U_g = 3 m/s, Dense Phase.

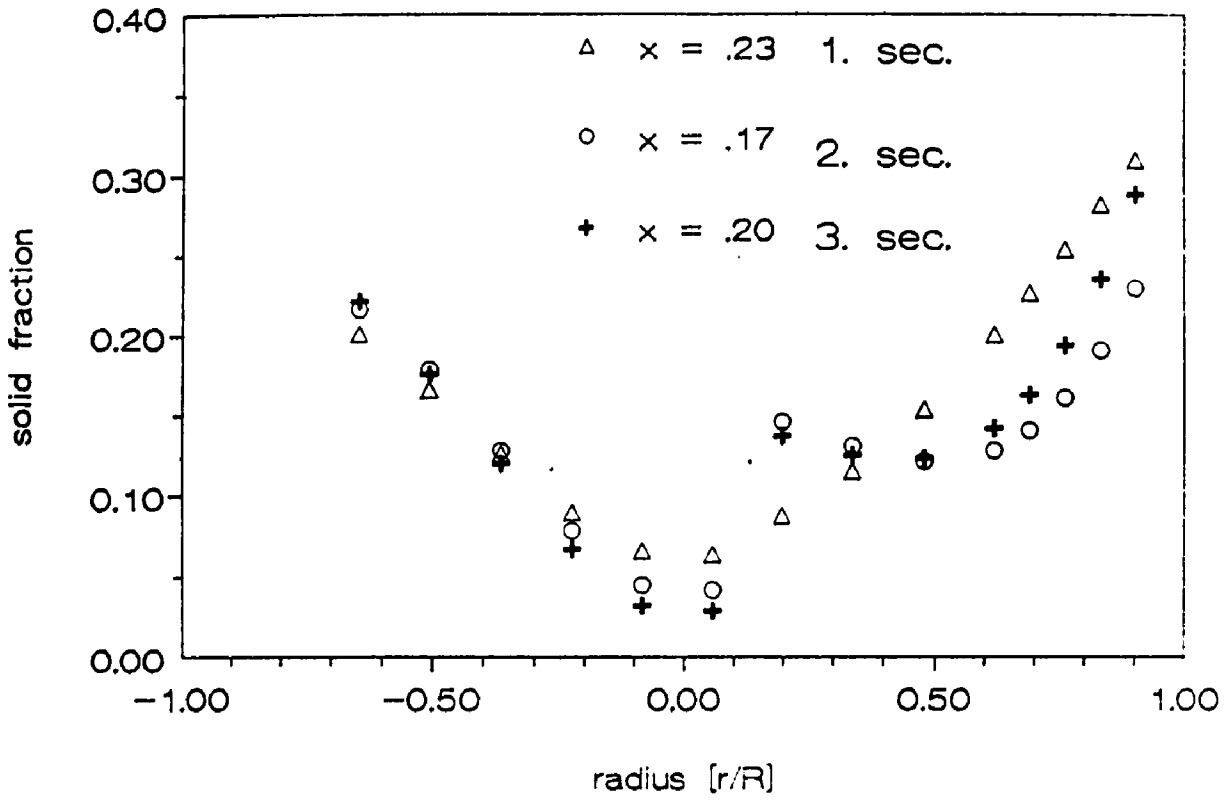

Fig. 4.11 Radial Density Profile Reconstruct by Means of a Third Order Polynomial Function, Left and Right Side are Calculated Separately.

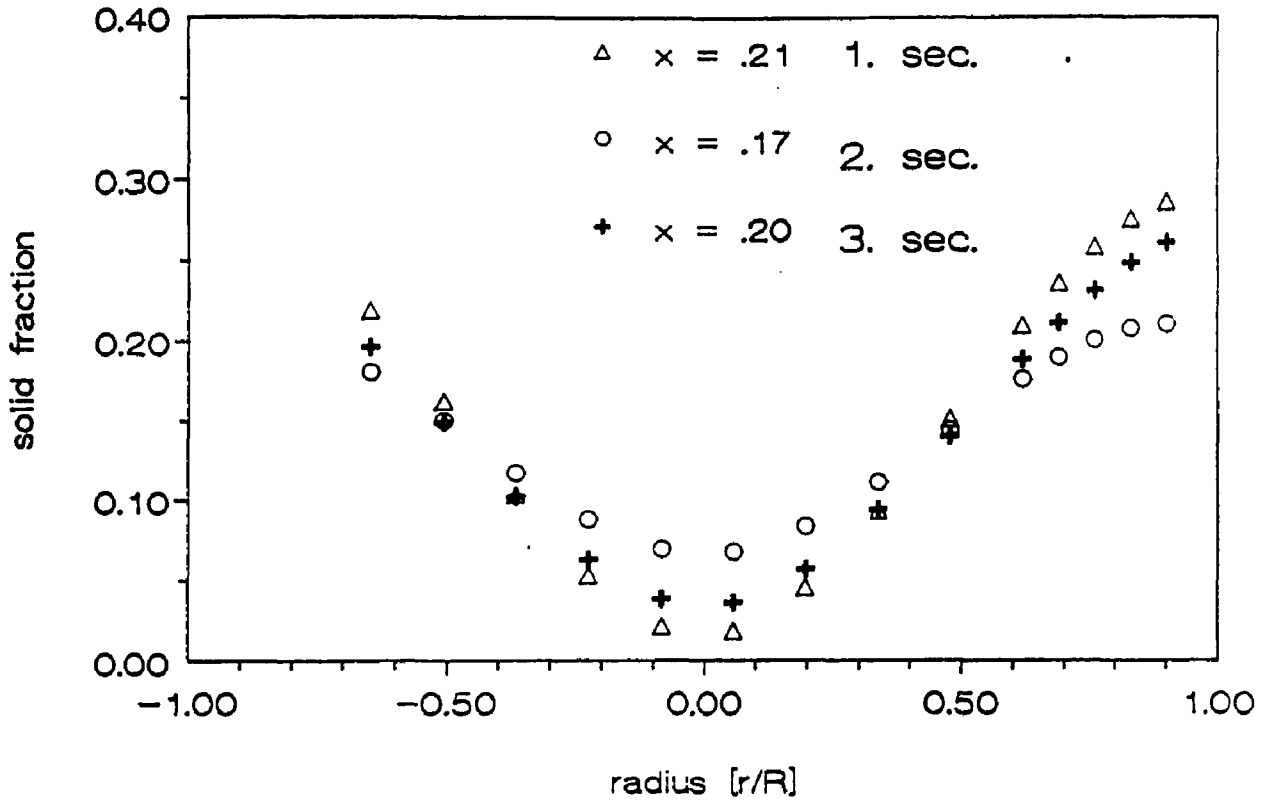

Fig. 4.12 Radial Density Profile Reconstructed by Means of a Third Order Polynomial Function, Left and Right Side are Overlapped.

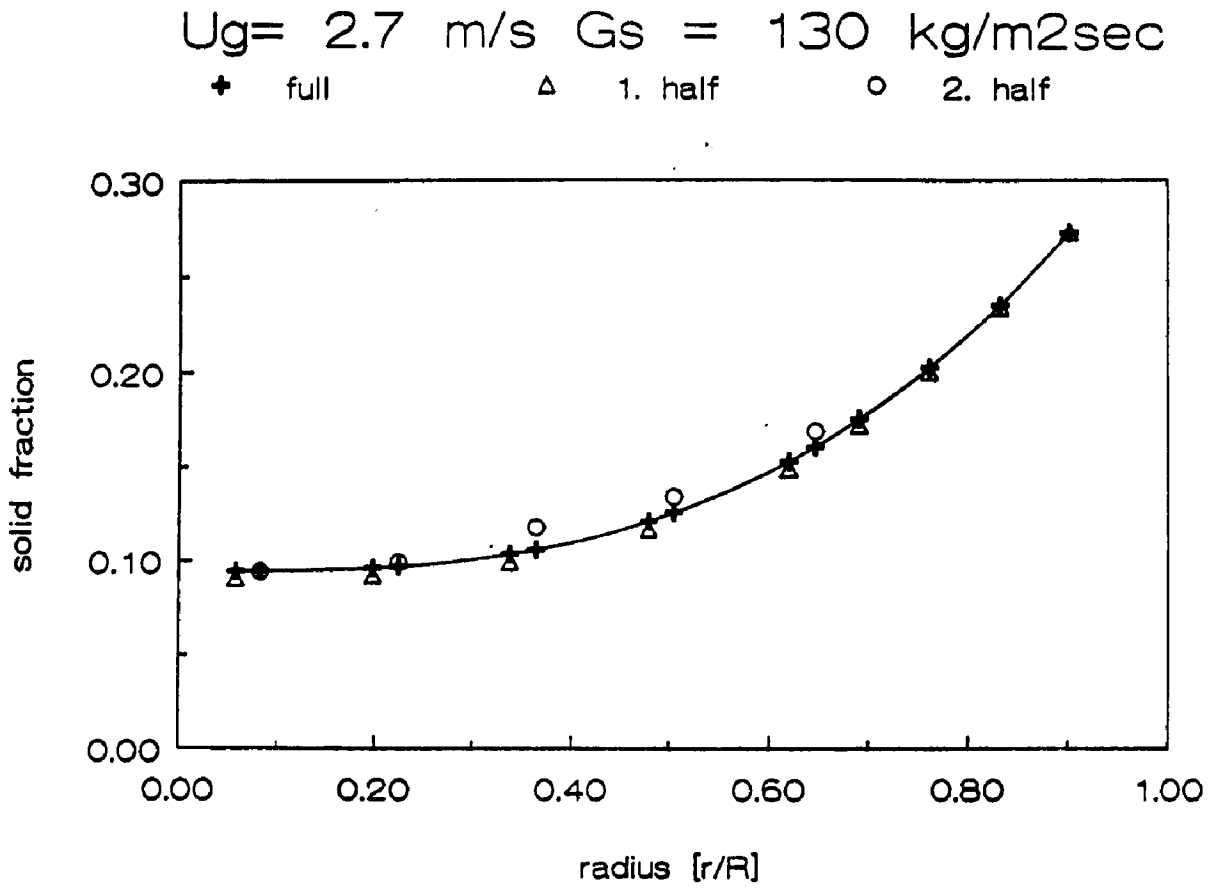

Fig. 4.13 Radial Density Profile Reconstruct by Means of a Third Order Polynomial, Averaging Time is 100 Seconds.

4.3 Radial Density Profiles

Radial density profiles indicate a segregation of the two phase flow in the fast fluidized bed in the sense that a dilute core region is surrounded by a denser annular outer or wall region. In the core region the solid is preferentially transported upwards while in the denser wall region a more up and down oscillating type of flow exists. The shape of the density profile in the dense region is parabolic and in the dilute region flatter. For smaller diameter risers used in research work the parabolic shape of the density profile is not dependent on the riser diameter (Hartge, 1985, Fig. 2.10) but is typical for the gas solid flow in the high velocity fluidization regime.

To determine if a fully developed flow pattern in either the dense or dilute phase exists, axial and radial density profiles were studied. As shown earlier, pressure fluctuation readings are dependent on the spacing of the probes. Radial density profiles presented during the last few years or so by several researchers (i. e. Gajdos and Bierl,1978; Shao, 1985; Hartge et al, 1985; Herb et al, 1989 etc.) with different measurements techniques show different shapes at different heights in the riser. Some measurements were taken in the dense phase and some in the dilute phase. However, no conclusion can be drawn at this point as to whether or not the flow in the riser is fully developed from these data. A clear indication of the existence of a fully developed flow pattern in the riser is a constant time mean average solid fraction and a constant radial density profile. In this work runs were

made at various superficial gas velocities and solid flow rates. The operating parameters were chosen so that in the riser only a dense phase or only a dilute phase of the flow existed. Two cases, one in the dense and one in the dilute phase, with a superficial gas velocity of 3 m/s are shown. These are representative of all the other runs. In the dense phase (Fig. 4.14) the mean average solid fraction of the cross section and the profile are constant. The radial density profiles in the dilute phase (Fig. 4.15) exhibit a change with position and there is in particular decrease of the solid fraction especially in the wall region. The mean average solid fraction also decreases with increasing height.

The integrated solid fraction of an x-ray beam in the wall region and through the middle of the bed as function of the height for the dilute and dense phase is plotted in Figure 4.16 and 4.17. In the dense phase both the solid fraction in the wall region and in the middle are constant which indicate the existence of a fully developed flow pattern. The solid fractions in the dilute phase (Fig. 4.17) decrease with increasing height. No fully developed flow exists in the dilute phase at least for an L/D of up to 30.

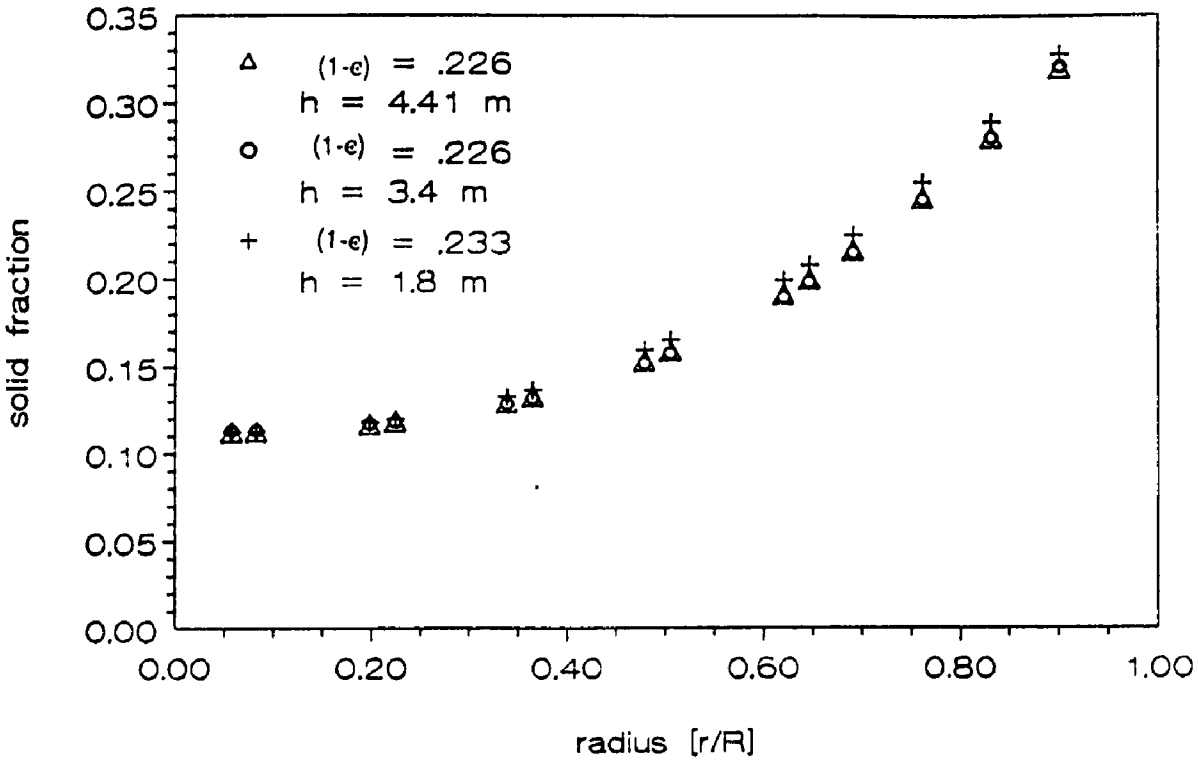

Fig. 4.14 Radial Density Profiles at Three Different Heights in the Dense Phase, U_g = 3 m/s, G_s = 140 kg/m^{2}s.

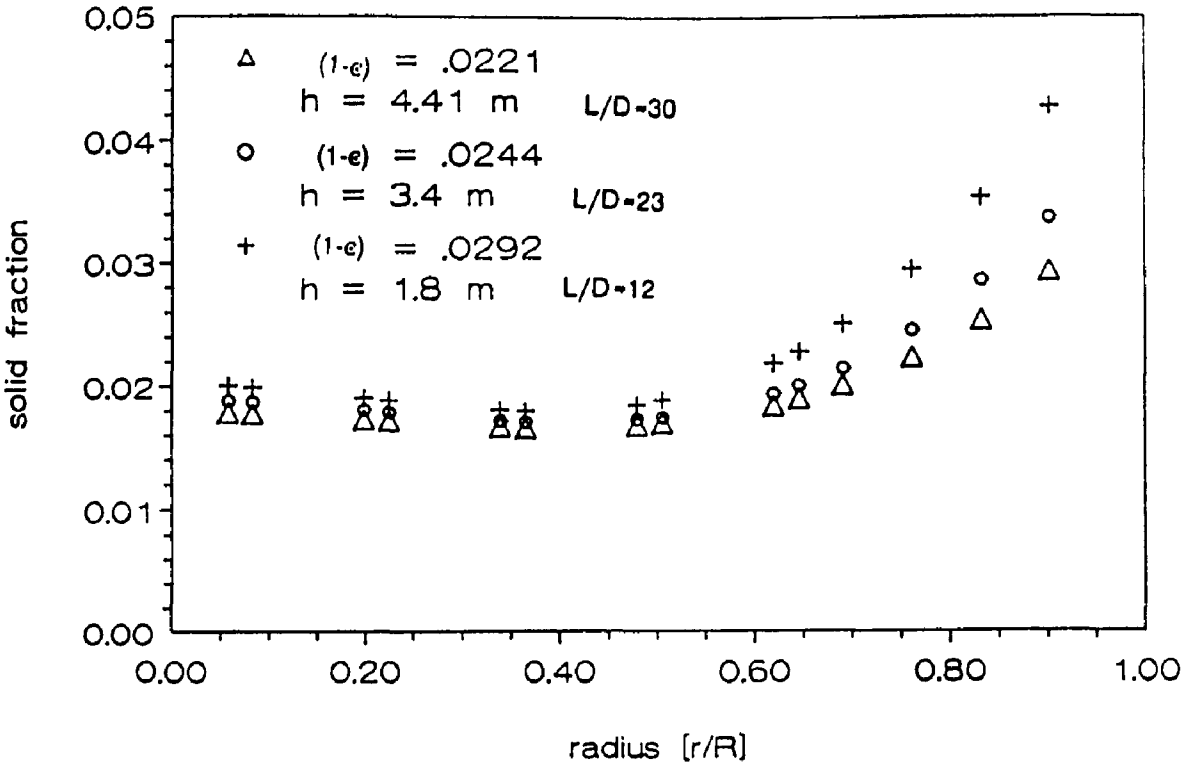

Fig. 4.15 Radial Density Profiles at Three Different Heights in the Dilute Phase. U_g = 3 m/s, G_s = 50 kg/m^{2}s.

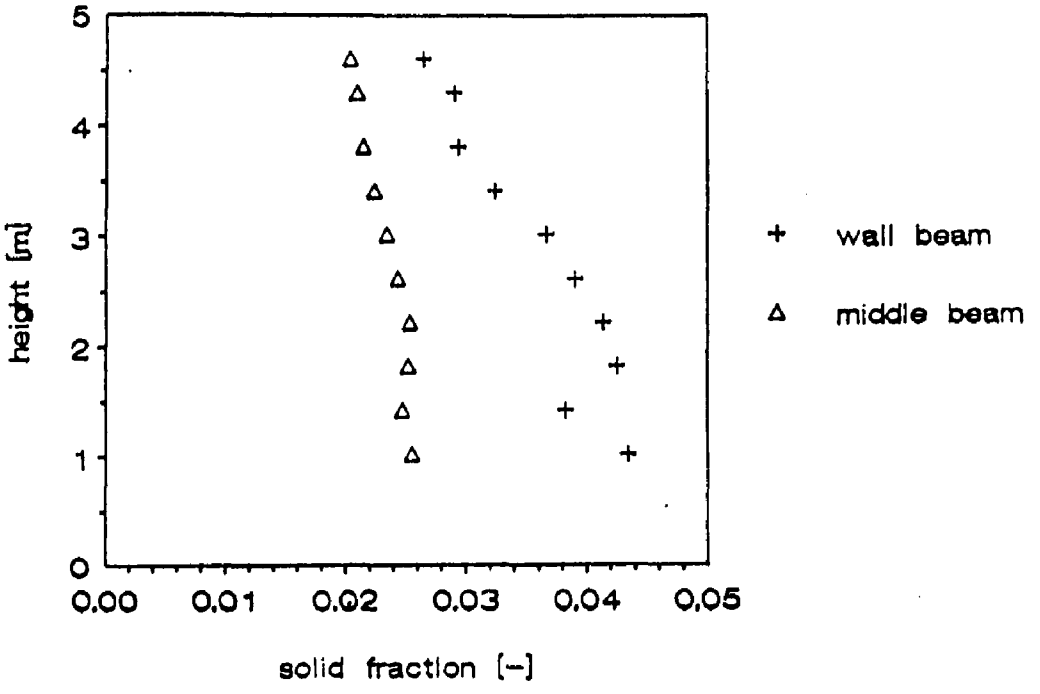

Fig. 4.16 Integrated Solid Fraction of an X-Ray Beam in the Wall Region and Trough the Middle of the Riser in Dilute Phase.

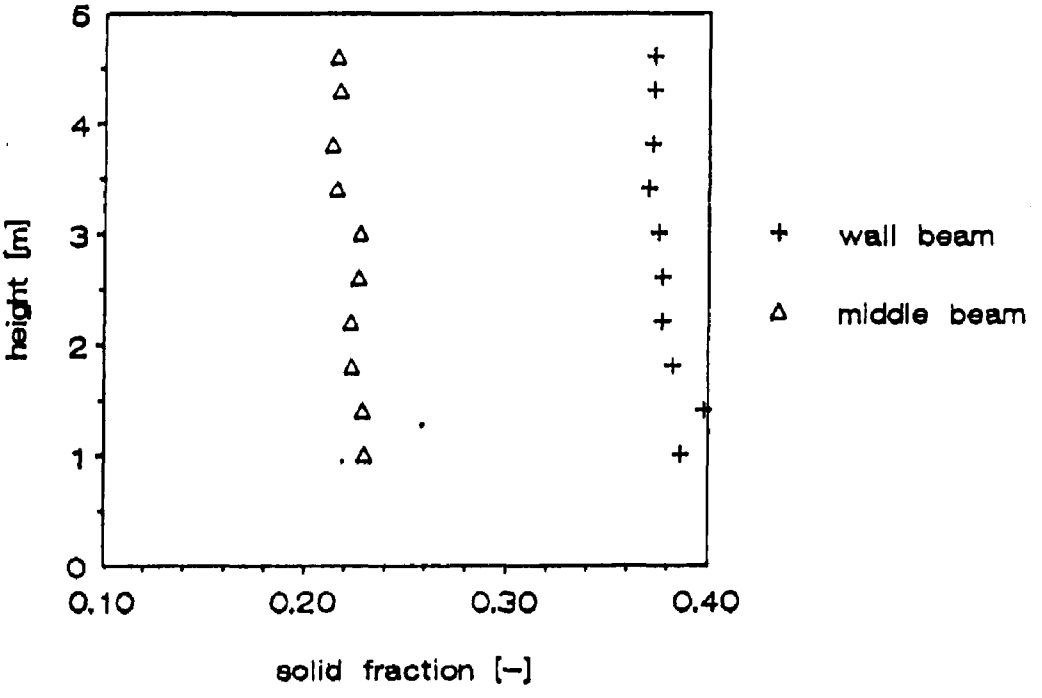

Fig. 4.17 Integrated Solid Fraction of an X-Ray Beam in the Wall Region and Trough the Middle of the Riser in Dense Phase.

4.4 Comparison of Pressure and X-Ray Fluctuation Measurements

Differential pressure readings are the pressure drop in a vertical span of the riser caused by the solid fraction and by local turbulence. The cross sectional average and radial distribution of the solid fraction alone may be detected with the x-ray method. To gain more understanding of the physical structure of the high velocity two phase flow in this chapter x-ray measurements and pressure fluctuation readings are analyzed.

Mean axial pressure profiles converted to solid fraction profiles help to determine if a dense or dilute phase or both are present in the riser. Typical axial solid fraction profiles at a superficial gas velocity of 3 m/s in the dense and dilute phases are shown in Fig. 4.18 and Fig. 4.19. The spacing of the pressure probes were 40 cm. X-ray measurements were taken between two adjacent differential pressure probes. The solid fraction for both measurements techniques are a three minute time average. In the bottom region of the riser (Fig. 4.18 and Fig. 4.19) the apparent solid fraction evaluated from the pressure gradient is higher than the solid fraction detected with the x-ray system. The difference is caused by acceleration of the solid in the entrance region.

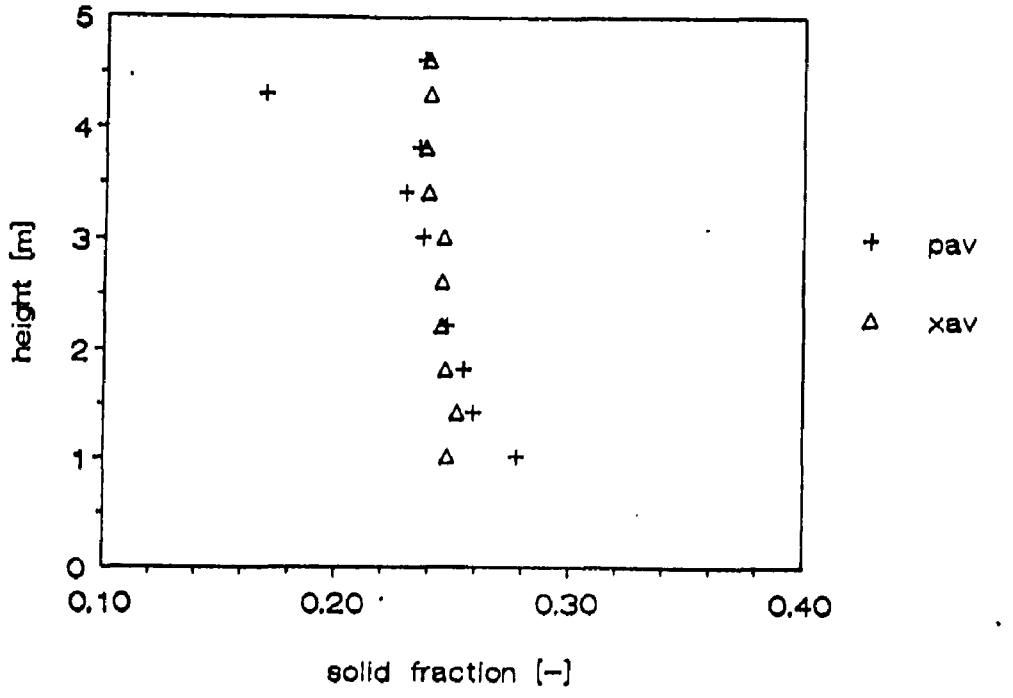

Fig. 4.18 Axial Solid Fraction Profile of Pressure Fluctuation Readings and X-Ray Measurements in the Dense Phase, U_g = 3 m/s.

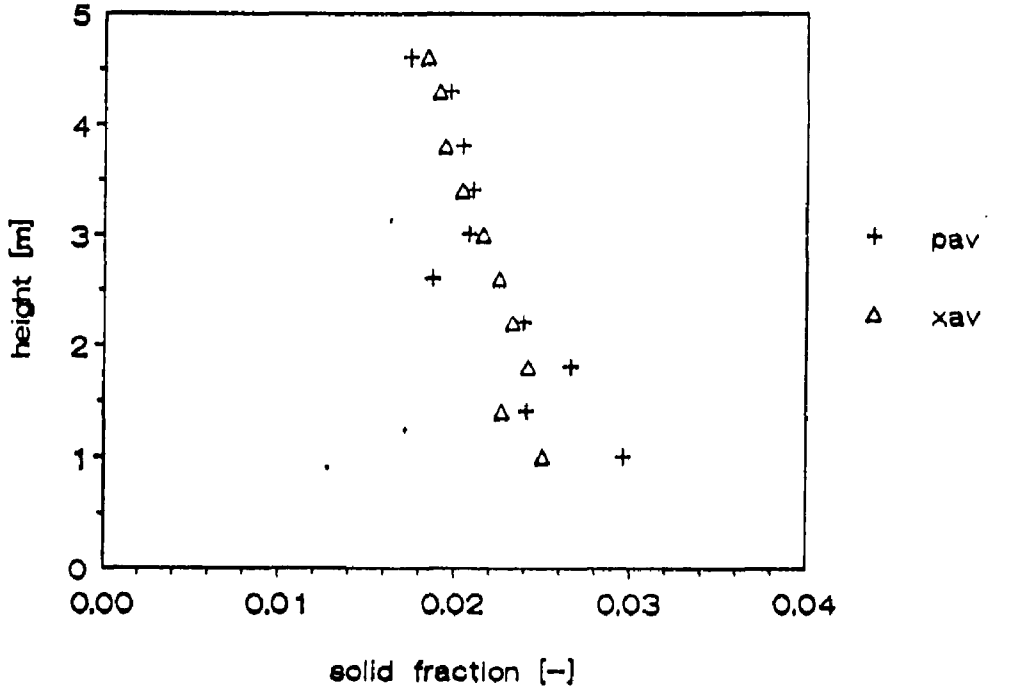

Fig. 4.19 Axial Solid Fraction Profile of Pressure Fluctuation Readings and X-Ray Measurements in the Dilute Phase, U_g = 3 m/s.

The length of the entrance region can be estimated, analyzing the axial solid profiles taken with x-ray and pressure gradient measurements at various velocities in either the dense or dilute phase. Above the entrance region the agreement between time-mean x-ray measurements and time mean pressure gradient measurements are excellent.

The time series of the solid fraction fluctuation of the x-ray measurements and pressure gradient measurements are shown in Fig. 4.20. The x-ray data are the instantaneous computed cross sectional average which have a damped response in contrast to the pressure fluctuation readings. The integrated solid fraction of an x-ray beam through the wall region and the middle of the riser is presented in Fig. 4.21. In the wall region large solid fluctuations are detected which support the idea in chapter 4.1 that with decreasing spacing of the differential pressure probes, the increasing pressure fluctuation readings are mainly caused by solid movement in the denser wall region. Solid fractions in the core have smaller fluctuations with a slightly smaller amplitude than the pressure fluctuation readings. A superimposed low frequency of approximately one Hz, discussed in section 4.1, is also dominant in the power spectra (Fig. 4.22) of the cross sectional average x-ray measurements. While the pressure fluctuation reading exhibits a sharp peak at one Hz, the x-ray readings also detect frequencies lower than one Hz. The lower than one Hz fluctuations appear to be generated mostly in the oscillating wall region as seen in the power spectrum of the integrated solid fraction of the x-ray beam

through the wall region (Fig. 4.23).

The Probability Density Functions (PDF's) (Fig. 4.24) show, for the x-ray measurements, a smaller variance than the pressure fluctuation PDF's. It is interesting that the PDF's of the x-ray beam through the wall region of the dense phase (Fig. 4.25) exhibit density fractions similar to a packed bed while the middle beam has solid fractions as low as observed in the dilute phase.

The measurements discussed above indicate clearly the existence of a dilute core surrounded by a dense annulus or wall region. The pressure fluctuation readings which represent a cross-sectional average are mainly the result of fluctuations in the wall region because almost all of the solid at any axial position is in the wall region.

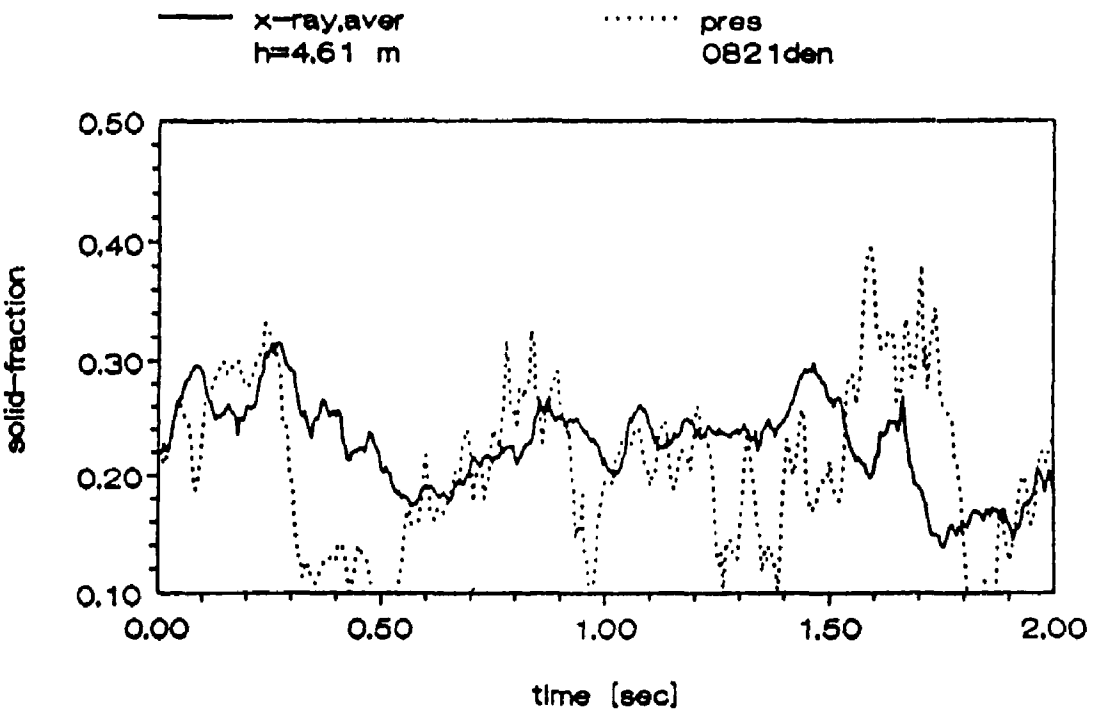

Fig. 4.20 Time Series of X-Ray Measurements and Pressure Fluctuation Readings in the Dense Phase, U_g = 3 m/s, G_s = 140 kg/m^{2}s.

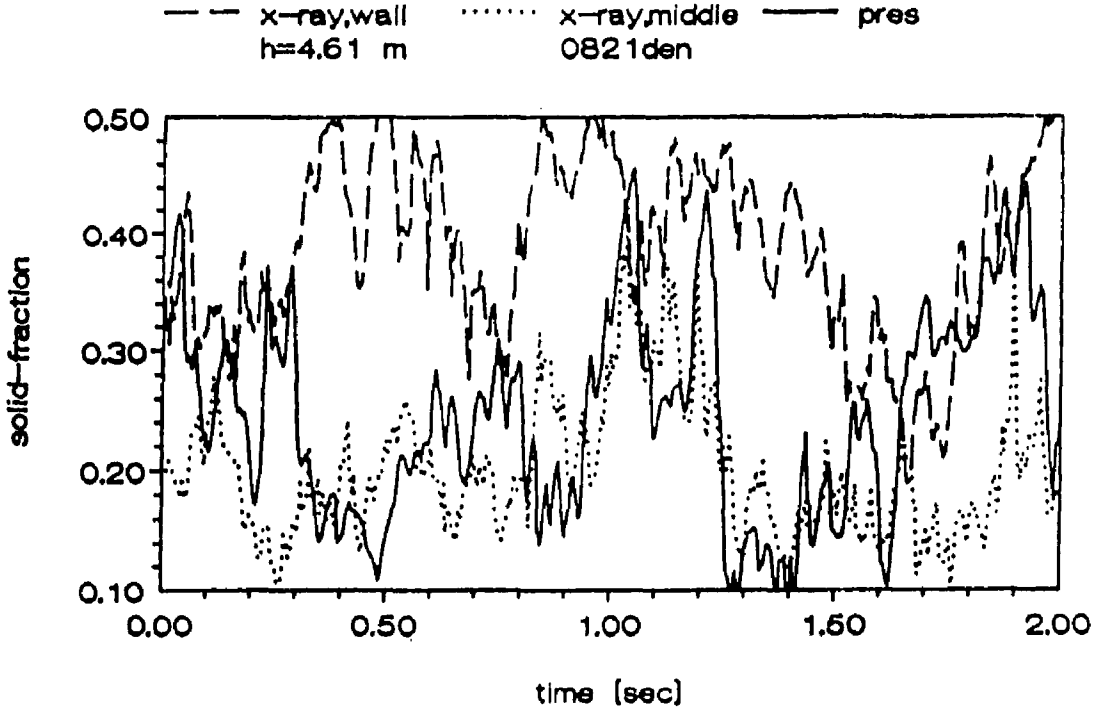

Fig. 4.21 Time Series of Pressure Fluctuation Readings and X-Ray Measurements, Wall Beam and Middle Beam, in a Dense Phase, U_g = 3 m/s.

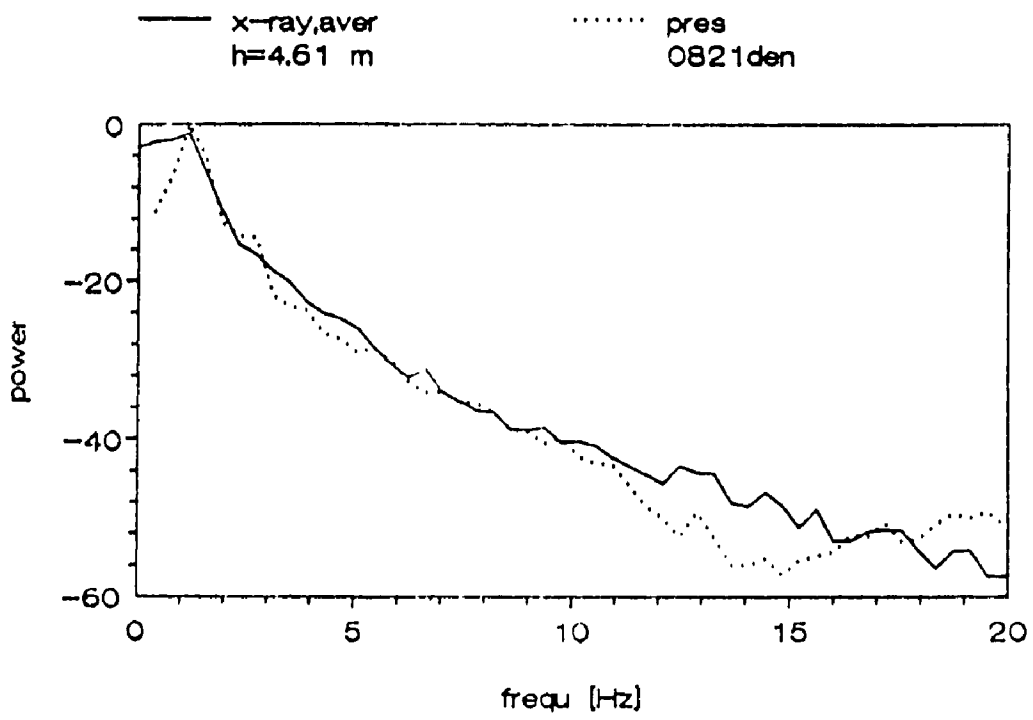

Fig. 4.22 Power Spectra of Pressure Fluctuation Readings and X-Ray Measurements in the Dense Phase, U_g = 3 m/s.

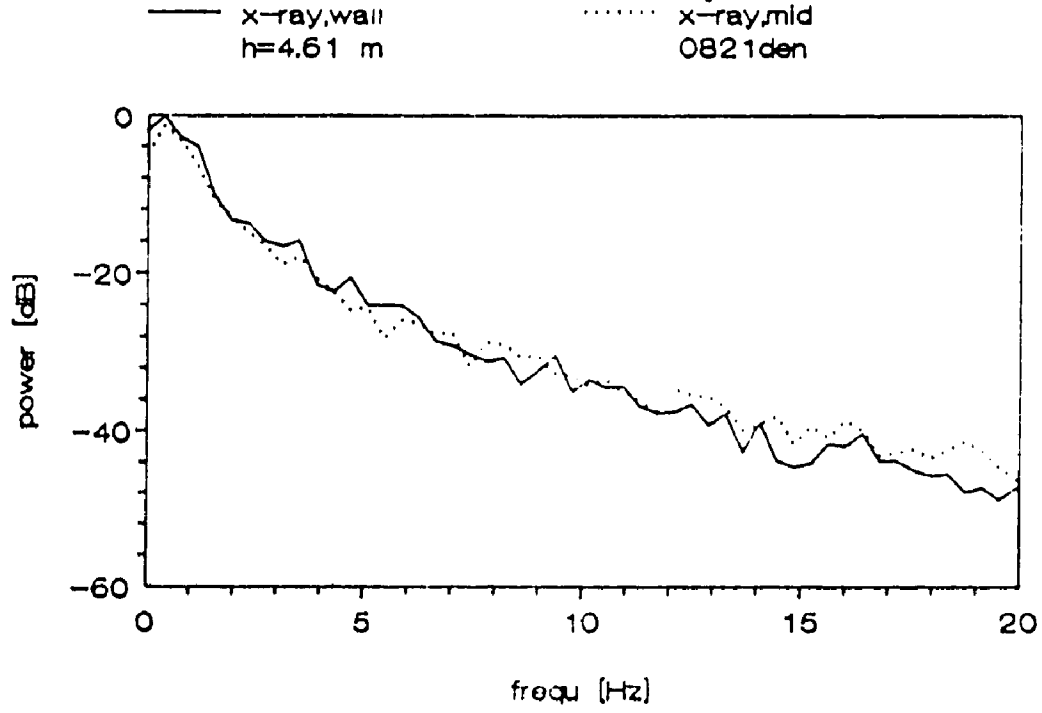

Fig. 4.23 Power Spectra of X-Ray Measurements, Wall Beam and Middle Beam in the Dense Phase, U_g = 3 m/s.

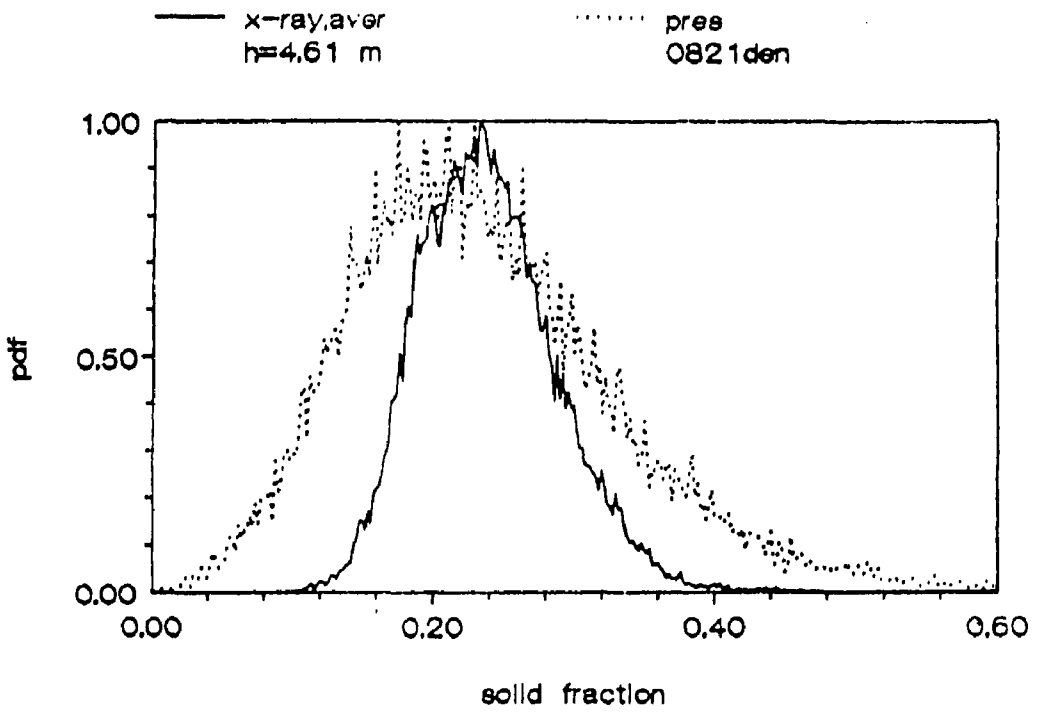

Fig. 4.24 PDF's of Pressure Fluctuation Readings and X-Ray Measurements in the Dense Phase, U_g = 3 m/s.

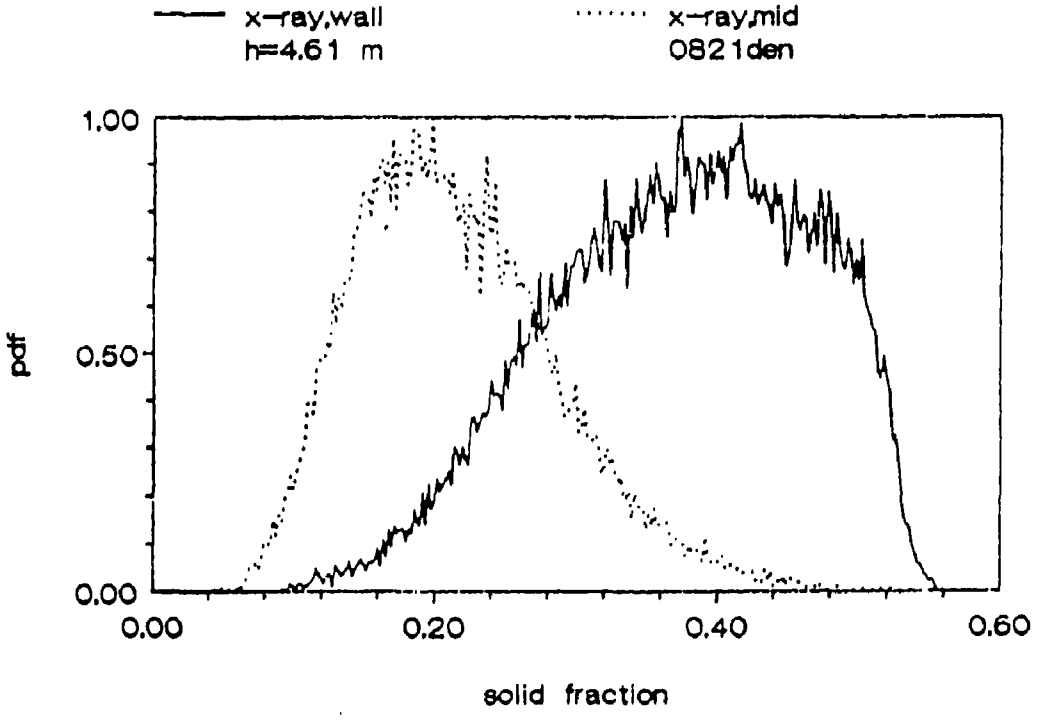

Fig. 4.25 PDF's of X-Ray Measurements in the Dense Phase, Wall Beam and Middle Beam, U_g = 3 m/s.

4.5 Variance Analysis

The variance, σ, of a probability density function computed from the x-ray measurements or pressure fluctuation readings is a measure of the quality of the fluidization. A small variance indicates a more homogenous flow than does a large one. The standard deviation of differential pressure signals was used in earlier research work (Yerushalmi et al, Schnitzlein, 1986, etc.) to classify the different regimes of the high velocity fluidized flow.

For the course of this work the variance, σ, of the x-ray measurements and pressure fluctuation readings (spacing of 40 cm) are normalized with the time mean solid fraction $(1-\epsilon)$. It has to be noted here that for these experiments the solid flow rate was adjusted so that only a dense or dilute phase was present in the riser. Fig. 4.26 shows the normalized variance in a riser operated at a superficial gas velocity of 3 m/s in the dilute phase. The variances for both pressure and x-ray readings are quite constant which allows us to calculate the height average for the x-ray measurements and pressure fluctuation readings. The averaged variance versus the superficial gas velocity is plotted in Fig.4.27. The variance of the pressure readings is always higher than the variance of the x-ray measurements. Only at a spacing of 1.60 m of the differential pressure probes does the variance from the pressure fluctuations have a value similar to that from the x-ray reading fluctuations. Because of the normalization of the variance

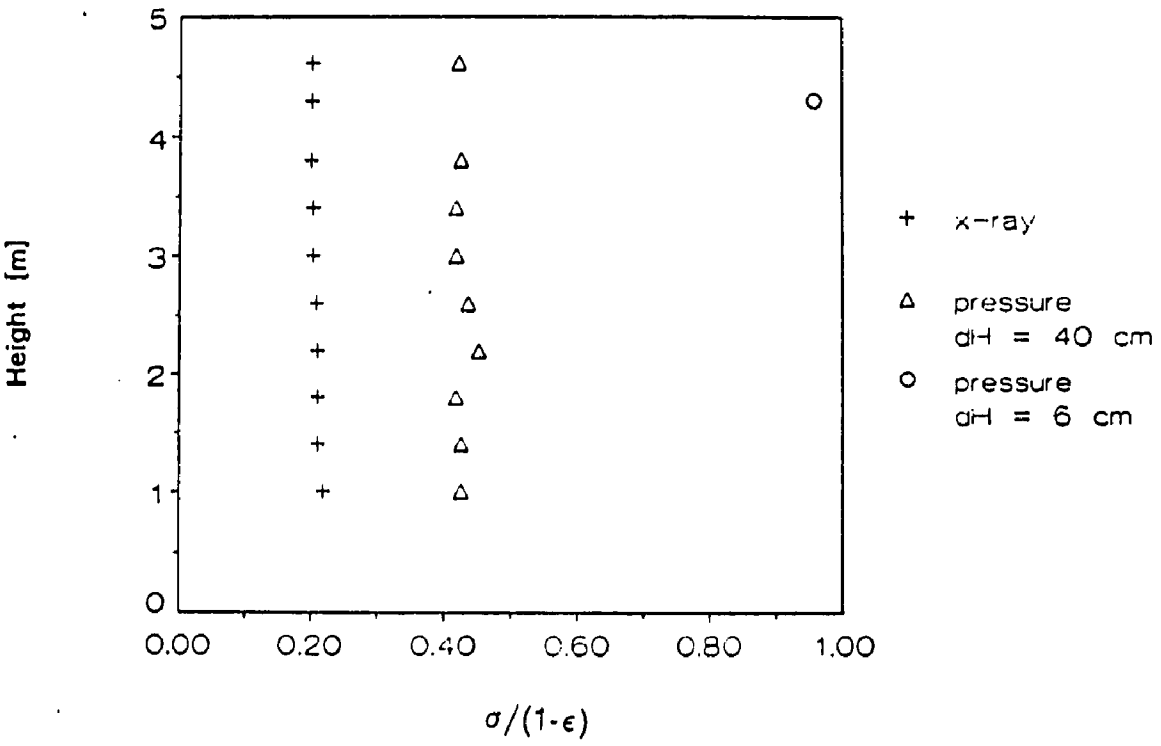

Fig. 4.26 Normalized Variance as a Function of the Height in the Dilute Phase, U_g = 3 m/s.

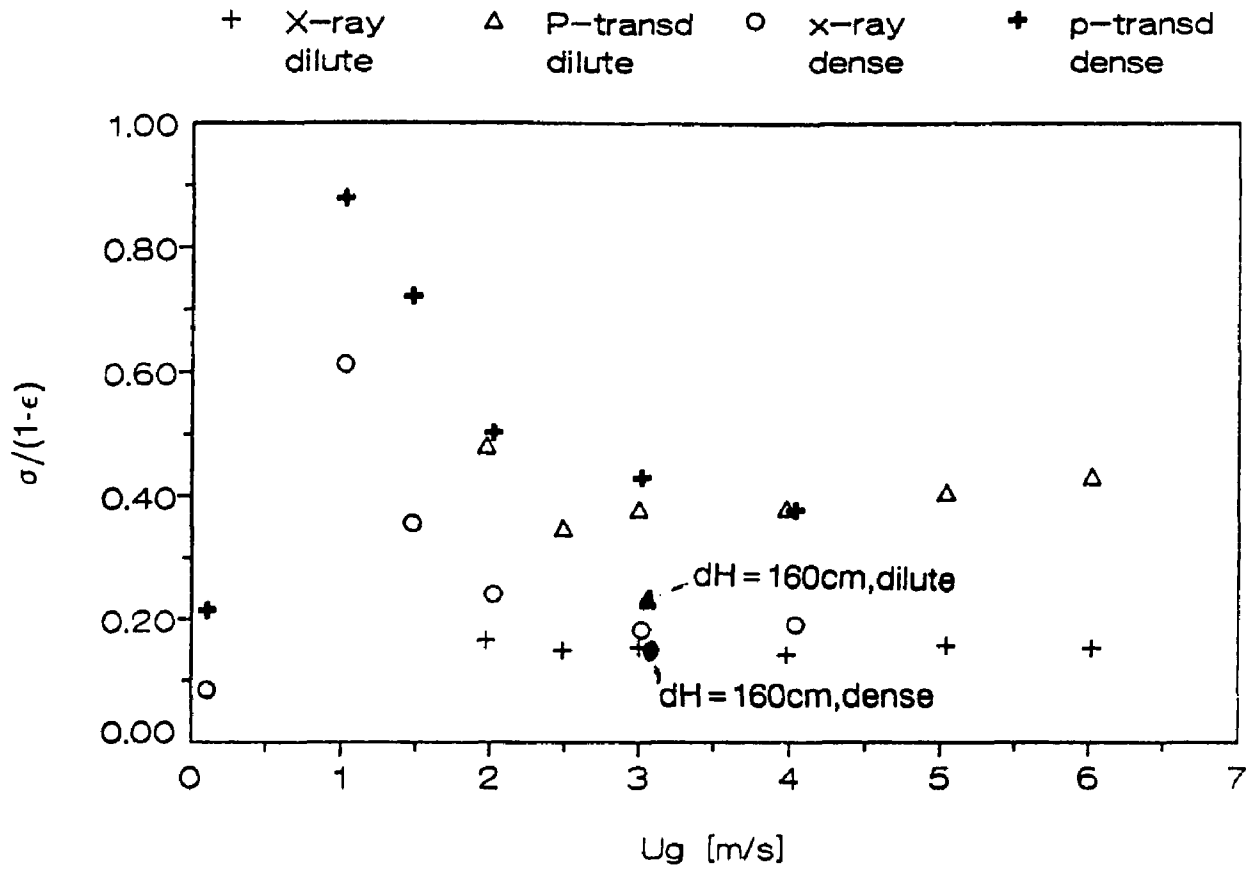

Fig. 4.27 Normalized Variance as a Function of the Superficial Gas Velocity.

with the solid fraction, both dense and dilute phases show the same normalized values.

The results of Fig. 4.27 are of considerable importance since they demonstrate that pressure fluctuation readings converted to solid fraction are larger in amplitude than the solid fluctuation detected with the x-ray system. Pressure fluctuation readings are a sum of the pressure drop caused by the solid fraction in a height segment of the riser and acceleration and deceleration of the solid. The difference between the values is relates to the magnitude of Reynolds stress-like correlation terms arising from the turbulence.

5. Conclusions

(1) A technique has been developed to directly measure instantaneous and time mean cross sectional solid fraction and its radial distribution in a high velocity fluidized bed. The method is based on an x-ray chordal absoptometry technique using phototransistor sensors hardwired to a computerized data acquisition system. The x-ray assembly is mounted on a tray, which moves along the bed length.

(2) The amplitude and the time average of differential pressure readings in the high velocity fluidized bed both increase with decreasing spacing (<40 cm) of the pressure taps. The probability density functions of the pressure fluctuations are symmetric for a spacing of more than >80 cm and become more and more asymmetric in shape with decreasing spacing. Pressure fluctuation readings with a spacing of less than 40 cm are strongly influenced by the local turbulence in the flow. For large spacings (>80 cm) an averaging effect over the turbulent fluctuations is observed.

(3) All of the power spectra show a superimposed low frequency of about one Hz, independent of the spacing.

(4) The minimum data collection time to obtain reproducible time-average data is 3 min for the pressure fluctuation measurements and one minute for the x-ray measurements.

(5) The x-ray measurements show the existence of radial profiles of solid fraction in the dense phase and dilute phase in the riser. The profiles indicate a core-annulus flow pattern with a dilute core and a dense wall region. The shape of the profiles in the dense phase above the entrance region is quite constant which indicates a fully developed flow in the dense phase. Solid fraction profiles in the dilute phase become flatter with increasing height in the riser. Thus the dilute phase flow is not fully developed for at least an L/D ratio of 30.

(6) Pressure fluctuation readings converted directly to apparent solid fraction are larger in amplitude than the solid fraction fluctuation detected with the x-ray system. Pressure fluctuation readings are a sum of the pressure drop due to the solid fraction in the segment of the riser and accelerations and decelerations of the solid. The power spectra for both the pressure readings and x-ray measurements show a superimposed low frequency which may be interpreted as the natural or resonance frequency of this apparatus. Additionally, x-ray measurements also show the existence of frequencies lower than the superimposed one Hz frequency.

REFERENCE

Abed, R., (1984), in Fluidization, Kunii and Toi, Eds., Engineering Foundation

Avidan, A.A., (1980), "Bed Expansion and Solid Mixing the High Velocity Fluidized Beds", Ph.D. Thesis, City University of New York

Baskakov, A.P. et al., (1973), "Heat Transfer to Objects Immersed in Fluidized Beds", Powder Technology 8, pp. 273 - 282

Basu P. and J.F. Large, (1988), "Circulating Fluidized Bed Technology II", Pergamon Press, Oxford, New York, Beijing

Beisswenger, H.; Daradimos,G.; Janssen, K. and V. Petersen, (1980), "Die Verbrennung ballastreicher, meist schwefelhaltiger Brennstoffe in der zirkulierenden Wirbelschicht", Aufbereitungstechnik, 12, pp. 616 - 621

Berker, A. and T. J. Tulig, (1986), "Hydrodynamics of Gas-Solid Flow in a Catalytic Cracker Riser: Implications for Reactor Selectivity Performance", Chem. Eng. Sci. 41 p. 821, 1986

Brereton, C. and J. R. Grace, (1989), "The Intermittency Index and its Significance for Fast Fluidization", Free Forum of the International Fluidization Conference, Banff, Alberta, 7-12 May 1989

Fan, L.S.; Satija, S. and K. Wisecarver, (1986), "Pressure Fluctuation Measurements and Flow Regime Transitions in Gas-Liquid-Solid Fluidized Beds", AICHE J., 32, P.328

Feindt, H.-J., (1986), "Einfluss von Wäremetauscherrohren auf die lokale Strömungsmechanik von Gas/Feststoff- wirbelschichten", Masterthesis Technische Universitat Hamburg-Harburg

Furusawa, T. and T. Shimizu, (1988), "Analysis of Circulating Fluidized Bed Combustion Technology and Scope for Future Development", Proceedings of the Second International Conference on Circulating Fluidized Beds, Compiegne, France, March 14-18, pp. 51 - 62

Gajdos, L. J. and T. W. Bierl, (1978), "Studies in Support of Recirculating Bed Reactors for the Processing of Coal", Topical Report, DOE Contract No. Ex-C7601-2449

Geldart, D., (1973), "Types of Gas Fluidization", Pow. Tech., 7, pp. 285 -292

Hartge, E. U.; Li, Y. and J. Werther, (1985), "Analysis of the Local Structure of the Two Phase Flow in a Fast Fluidized Bed", 1st Int. Conf. on Circulating Fluidized Beds, Halifax

Hartge, E. U., Renser, D. and J. Werther, (1988), "Solids Concentration and Velocity Patterns in Circulating Fluidized Beds", in Circulating Fluidized Bed Technology II, Pergamon Press, Toronto

Herb, B.; Tuzla, K. and J. C. Chen, (1989), "Distribution of Solid Concentrations in Circulating Fluidized Bed", in Fluidization VI, J. R. Grace, L. W. Schmidt and M. A. Bergougnou, Eds., Engineering Foundation, New York

Heyde, M. and H.J. Klocke, (1979), "Wärmeübergang zwischen Wirbelschicht und Wärmetauschereinheiten", vt "Verfahrenstechnik", 13, November, pp. 199 - 209

Hinze, J. O., Turbulence, McFraw Hill, New York, 1959

Kwauk, M. and Y. Li, (1980), "The Dynamics of Fast Fluidization", in Fluidization, J.R. Grace and J.M. Matsen, ed., Plenum Press, New York and London

Kwauk, M.; Li, Y.; Chen, B.; Wang, F. and Y. Wang, (1981), "Hydrodynamic Correlations for Fast Fluidization", presented at China-Japan Symposium on Fluidization, China, April 4-9

Lanneau, K.P., (1960), "Gas-Solids Contacting in fluidized Beds", Trans. inst. Chem. Engrs., 38, p. 125

Lewis, W.K.; Gilliland, E.R. and W.C. Bauer, (1941), "Characteristics of Fluidized Particles", Ind. Eng. Chem., 41, pp 1104 -1117

Li, Y. and M. Kwauk, (1980), "The Dynamics of Fast Fluidization", in "Fluidization", Grace, J.R. and J.M. Matsen, Plenunm Press, New York - London, p. 537

Li, J.; Tung, Y. and M. Kwauk, (1988), "Energy Transport and Regime Transition in Particle-Fluid Two-Phase Flow", in Circulating Fluidized Bed Technology II, P. Basu and J.F. Large, ed., Oxford, New York, Beijing

Li, J.; Tung, Y. and M. Kwauk, (1988), "Method of Energy Minimazation in Multi-Scale Modeling of Particle-Fluid Two-Phase Flow", in Circulating Fluidized Bed Technology II, P. Basu and J.F. Large, ed., Oxford, New York, Beijing

Li, J. and H. Weinstein, (1989), "An Experimental Comparison of Gas Backmixing in Fluidized Beds Across the Regime Spectrum", in Chem. Eng. Sci., 44, pp 1697

Matsen, J.M., (1973), "Flow of Fluidized Solids and Bubbles in Standpipes and Risers", Pow. Tech., 7, pp. 93 - 96

Matsen, J.M., (1988), "The Rise and Fall of Recurrent Particles: Hydrodynamics of Circulation", Proceedings of the Second International Conference on Circulating Fluidized Beds, Compiegne, France, March 14-18, pp. 3 - 12

Paul, M., (1982), "Digitale Messwertverarbeitung", VDE-Verlag, Berlin-Offenbach

Pope, M., (1978), "Atmospheric Fluidized Bed Combustion Technology in the USA", VDI-Berichte no. 322

Reh, L., (1971), "Fluid Bed Processing", Chem. Eng. Progr., 67, pp. 58 - 64

Saxton, A. L. and A. C. Worley, (1970), Oil and Gas J., 68, 82

Schmidt, W.; Beisswenger, H. and F. Kaempf, (1979), "Flexibility of Fluid Bed Calciner Process in View of Changing Demands in the Alumina Market", Am. Inst. of Mining, Metallurgical and Petroleum Engineers: 106th AIME Annual Meeting, New Orleans

Schnitzlein, M. (1987), "The Hydrodynamics of a Fast Fluidized Bed Characterized by its Pressure Signals",
Ph.D. Thesis, City University of New York

Schnitzlein, M. and H. Weinstein, (1988), "Flow Characterization in High-Velocity Fluidized Beds using Pressure Fluctuations", Chem. Eng. Science, 43, pp. 2605 - 2614

Shao, M., (1986), "Radial and Axial Variation in Voidage in High Velocity Fluidized Beds", Ph.D. Thesis, City University of New York

Weinstein, H.; Li, J.; Bandlamudi, E.; Feindt, H.J. and R. A. Graff, (1989), "Gas Backmixing in Fluidized Beds in Different Regimes and Different Regions", in Fluidization VI, J. R. Grace, L. W. Schmilt and M. A. Bergougnou, Eds.

Weinstein, H.; Shao, M.J.; Schnitzlein, M., (1985), "Radial Variation in Void Fraction in Solid Density in High Velocity Fluidization", Paper presented at the First Int'l. Conference Circulating Fluidized Beds, Halifax, Canada

Weinstein, H.; Shao, M.J.; Schnitzlein, M. and R.A. Graff, (1986), "Radial Variation in Void Fraction in a Fast Fluidized Bed", Paper presented at the V Int'l. Conference on Fluidization, Elsinore, Denmark

Werther, J. and E.-U. Hartge, (1986), "Stroemungsstructuren in zirkulierenden Wirbelschichten", Chem. Ing. Tech., 58

Winkler, F., (1922), "Verfahren zum Herstellen von Wassergas", Patentschrift, DRP 437 970

Yerushalmi, J.; Molver, A.E. and A.M. Squires, (1974), "The Fast Fluidized Bed", Preprints of GVC/AICHE Joint Meeting and Jahrestreffen der Vergahrensingenieure, Munich

Yerushalmi, J.; Crankurt, N.T., Geldart, D. and B. Liss, (1978), "Flow Regimes in Vertical Gas-Solid Contact Systems", AICHE Sym. Ser., 74, pp. 1 - 13

Yerushalmi, J.; Gluckman, M.J.; Graff, R.A.; Dobner, S. and A.M. Squires, (1976), "Production of Gaseous Tuels from Coal in the Fast Fluidized Bed", in "Fluidization Technology", D.I. Kearins, Hemisphere Publ. Corp., New York

Yerushalmi, J.; Turner, D.H. and A.M. Squires, (1976), "The Fast Fluidized Bed", Ind. Eng. Chem. Process Des. and Dev., 15, p. 47

Yerushalmi, J. and N.T. Crankurt, (1978), "High - Velocity Fluidized Beds", Chem.-Tech., 9, pp. 564 - 572

Yerushalmi, J. and N.T. Crankurt, (1979), "Further Studies of the Regimes of Fluidization", Pow. Tech., 24, pp. 187 - 205